Doklady Physics, Vol. 46, No. 2, 2001, pp. 103–106. Translated from Doklady Akademii Nauk, Vol. 376, No. 6, 2001, pp. 753–756.

TECHNICAL PHYSICS

Analysis of Ice Conditions in Arctic Regions according to Data of Radiophysical Measurements by the "Okean-01" Satellite

A. M. Volkov*, V. D. Grishchenko, V. F. Kravchenko***, V. S. Loshchilov**, A. M. Pichugin*, Corresponding Member of the RAS V. I. Pustovoĭt****, and I. S. Skuratova*******

Received September 9, 2000

INTRODUCTION

Radiophysical methods play an important role in solving problems of the Earth's remote probing (see, e.g., [1–5]). Among them, microwave-range multichannel satellite data are of paramount significance, since they provide complete information on environmental conditions on the basis of observations from space independently of the weather and illuminance of the Earth's surface. The latter fact is of particular importance while monitoring the sea-ice cover in polar regions. However, in spite of the intense development of radar ([1, 2, 4, 6–9] etc.) and radiometric ([1, 4, 10, 11] etc.) systems for the space monitoring of the environment, there is no experience to date concerning the combined data analysis of radar and radiometric Earth probing. This can be explained by the fact that the most known satellites are not equipped with adequate instruments operating synchronously in time and space. Only satellites of the "Okean" series possess these features [1, 2, 4]. Therefore, the urgency of the present study is evident.

INSTRUMENTAL CHARACTERISTICS

In this study, we present results of a complex analysis and an interpretation of patterns of sea ice, which were obtained with the help of both a radar lateral-scanning system functioning with an operation frequency of 9.52 GHz, a scanning band of 450 km, and a coordinate resolution of 2×2 km^2 and a PM-08 microwave radiometer operating at a frequency of 36.6 GHz with horizontal polarization, a scanning band of 550 km, and a coordinate resolution of 20×20 km^2. Both systems are installed on board the "Okean-01" satellite [1, 2, 4, 12].

AN ALGORITHM FOR DATA INTERPRETATION

In spite of its rather low resolution, the PM-08 radiometer makes it possible to obtain important information on ice conditions, which complements the data of a radar lateral-scanning system. In particular, the backscattering of radiowaves by rarefied young smooth ice is very low and differs little from the scattering by a weakly ruffling sea surface. Therefore, in patterns obtained with the help of a radar lateral-scanning system, this ice can be erroneously interpreted as an open water surface. In this case, the PM-08 ranging data make it possible to determine the positions of these ice fields more reliably owing to the stronger contrast between the radiations of the sea surface and the ice cover.

Below, we present an algorithm for the interpretation of microwave patterns of the sea-ice cover together with an estimate of the general and partial ice close-packing for predominant ice age stages. This algorithm is based on model calculations of radio-brightness temperatures and PM-08 radiometric data. Methods of processing and analysis of radiometric and radar patterns are described in a number of papers [13–15]; therefore, these problems are not discussed here.

We emphasize that single-channel measurements by a PM-08 radiometer make it possible only to distinguish either two age types of sea ice (provided that it completely covers the region under investigation and other ice types are absent) or the combination of ice and open water. To determine an ice type according to PM-08 ranging data, the following procedures should be performed:

* *Scientific Center of Prompt Earth Monitoring, Russian Aviation-Space Agency, Moscow, Russia*

** *Research Institute of Arctic and Antarctic Regions, St. Petersburg, Russia*

*** *Institute of Radio Engineering and Electronics, Russian Academy of Sciences, Mokhovaya ul. 18, Moscow, Russia*

**** *Research-Technological Center of Unique Instrumentation, Russian Academy of Sciences, Moscow, Russia*

***** *Research-Technological Center "KomTekh," Dolgoprudnyĭ, Moscow oblast, Russia*

1028-3358/01/4602-0103$21.00

1. Reclassification of the radiothermal pattern in accordance with the chosen threshold, and creation of the binary pattern in which the brightness values equal to 100 or 0 are assigned to all pixels corresponding to many-year ice or one-year ice, respectively. A similar procedure is performed to separate the boundary between the ice and the open water surface.

2. Low-frequency filtration by a window with a given size of the binary pattern obtained forms a tone pattern whose brightness in each pixel is proportional to the value of the close-packing of the many-year ice in the filter window. The size of this window is chosen depending on the necessary specification of the ice close-packing distribution, pattern resolution, and the scale of the ice map being created.

3. Reclassification of the smoothed pattern for separating the boundaries of zones with prescribed quantitative ranges of close-packing values for many-year ice, and assigning conditional brightness values to these zones.

4. Interactive procedure of constructing a vectorial file of the ice map with separating the boundaries of zones with given ranges of ice close-packing values according to their pattern in terms of a conditional brightness. Graphical ice symbols containing qualitative and quantitative parameters for distributions of the two ice types (in accordance with their international classification) are included in the zones.

REALIZATION IN PRACTICE

The above-mentioned approach to the interpretation of radiothermal patterns of sea ice is aimed at constructing ice maps with scales on the order of $1/3 \times 10^6$ to $1/5 \times 10^6$. In Fig. 1, an ice map of the ice close-packing distribution for the many-year ice and one-year ice is presented. The map is obtained according to data of a PM-08 radiometer using a filter window of 15 × 15 pixels.

To confirm the validity of the interpretation of sea-ice radiothermal patterns, a fragment of the complex ice map developed in the Center of the Ice and Hydrometeorological Information of the Research Institute of Arctic and Antarctic Regions for the period of January 10 to 15, 1997, is presented. The map was composed according to lateral-scanning radar-system

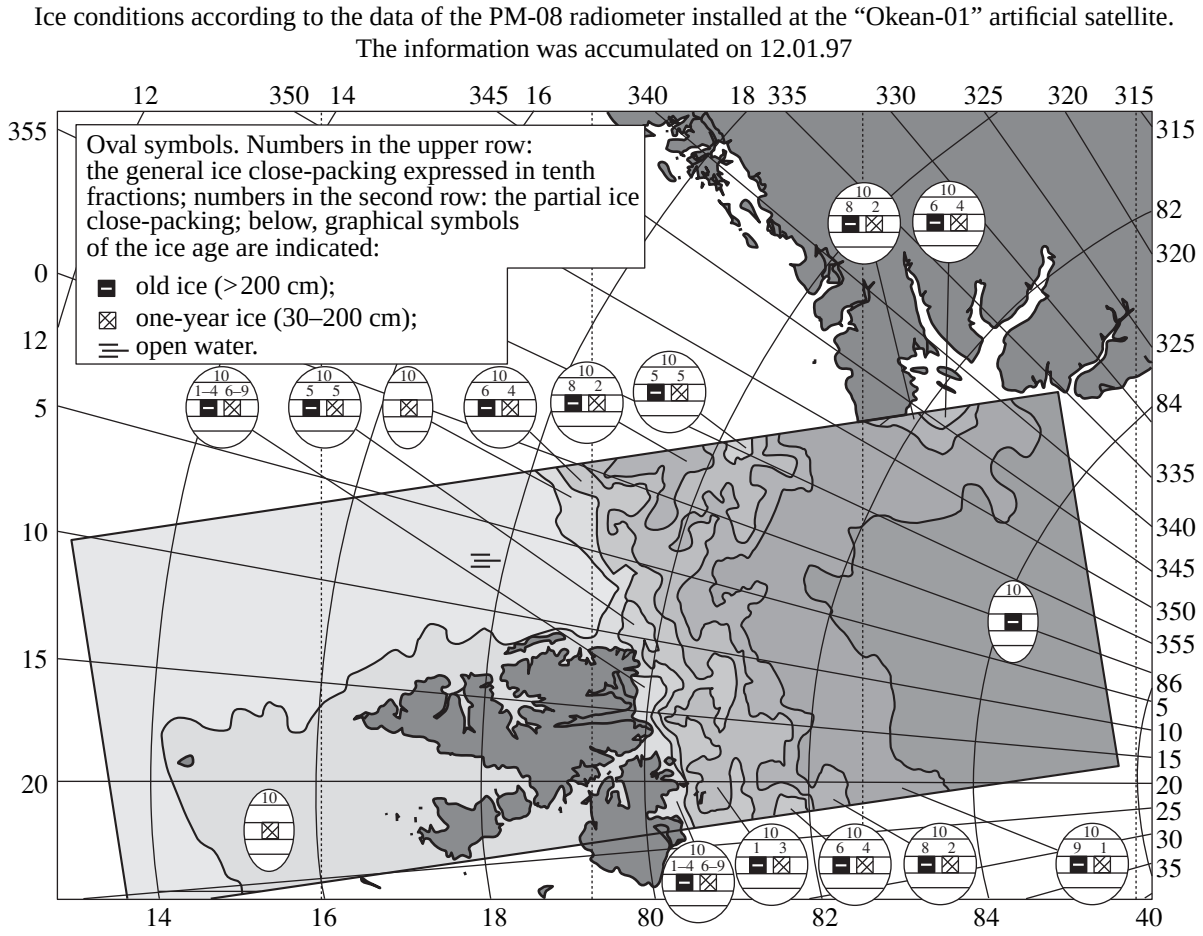

Fig. 1. Ice map composed according to the results of interpretation of the radiothermal pattern for the PM-08 microwave radiometer installed at the "Okean-01" satellite No. 7.

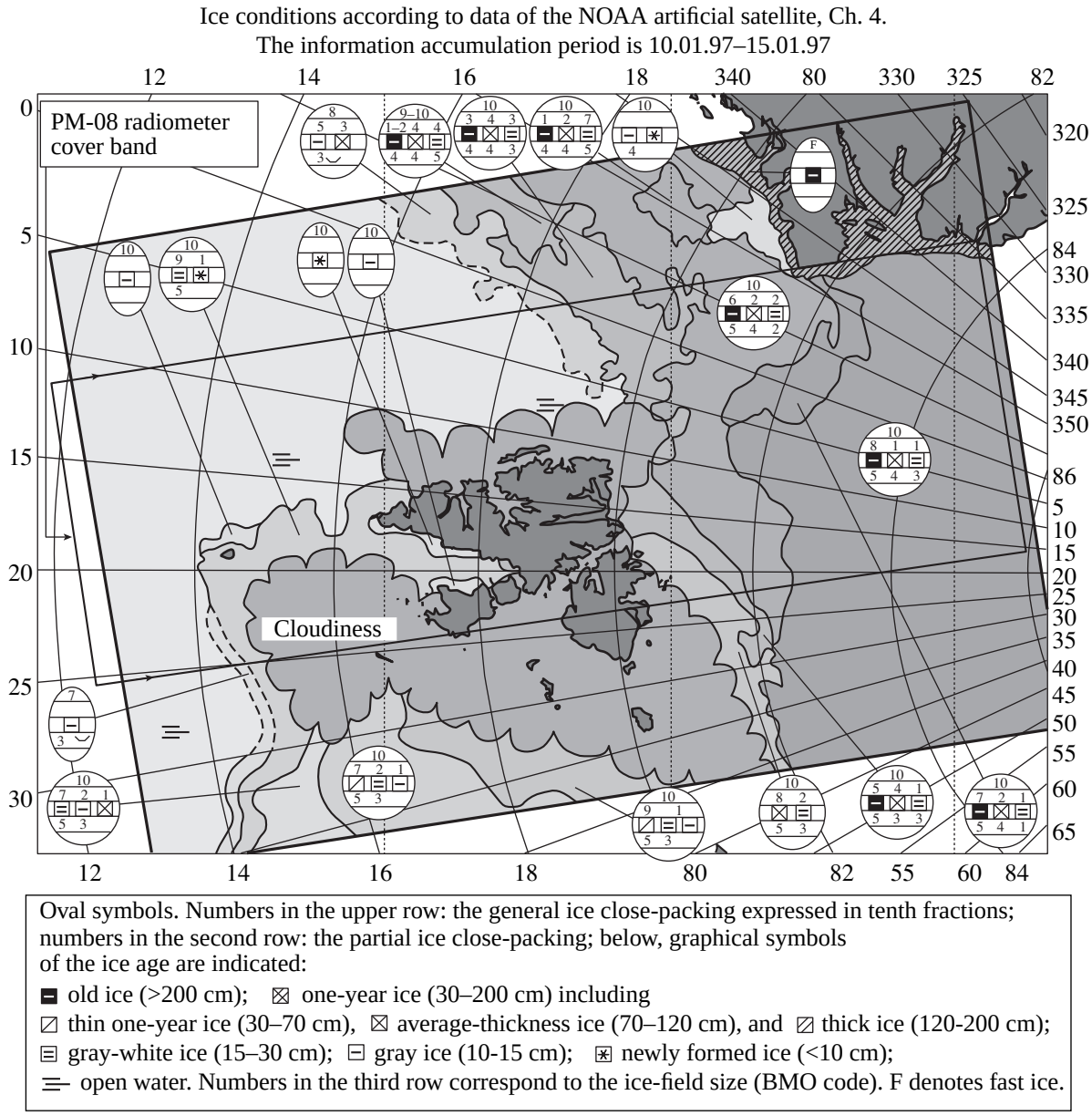

Fig. 2. Fragment of the complex review ice map composed according to the results of visual interpretation for a series of patterns obtained by the lateral-scanning radar system installed at the "Okean-01" satellite No. 7 and AVHRR patterns of the NOAA satellite in the infrared range for the period of January 10 to 15, 1997 (Archives of the Center for the Ice and Hydrometeorological Information of the Research Institute of Arctic and Antarctic Regions).

patterns obtained with the help of the "Okean-01" satellite and the AVHRR high-resolution multichannel radiometer of the NOAA satellite. Based on the comparative analysis of these maps, we are able to make the following conclusions:

1. The positions of the boundaries for a zone in which the old ice predominates (6/10 and larger), in general features, coincide for both maps.

2. The southern boundaries for a zone of maximum close-packing of the old ice approximately coincide. However, the partial close-packing for this ice is determined by the visual map as 8/10, (with the presence of 2/10 of the one-year white ice and gray-white ice). At the same time, according to the results of the interpretation of the radiothermal pattern, the close-packing of the old ice is determined to be 10/10; i.e., the presence of the one-year ice does not exceed 5%.

3. In accordance with the data of interpretation of the radiothermal pattern in the sea northern part (in the air-temperature zone of –35°C), the ice edge is shifted by 4 to 48 km towards the open water with respect to the position of this edge on the visual map. To the south

from the Medvezhiĭ island (in the air-temperature zone of –17°C), the ice edge is shifted by 24 to 37 km, but, contrarily, towards the ice pack. The cause of this disagreement could be an effect of the PM-08 antenna system and errors in both the choice of the radio-brightness temperature threshold for the open water while interpreting the radiothermal pattern and the determination of the ice edge position while visual interpreting patterns were obtained with the help of the satellites.

4. The boundaries and configurations of small zones do not coincide in detail; however, the variations in distinctions of partial ice close-packing do not exceed 2/10. These distinctions are typical for subjective estimates of the partial ice close-packing and are not considered as rough errors for ice maps.

CONCLUSIONS

Thus, comparative analysis of the ice maps has shown the general consistency between the results of automated interpretation of the radiothermal patterns and the data obtained by means of the visual interpretation of radar and infrared patterns with a higher resolution. Hence, the above-mentioned complex approach to the interpretation of radiothermal and radar patterns, which is complemented by information related to the optical range, can be used for mapping of the ice cover in the winter period of a year.

In spite of the relatively low spatial resolution, the PM-08 radiometer data are an important source of information on sea ice, especially in the case of a combined interpretation using lateral-scanning radar-system patterns. This combined analysis of radiothermal and radar patterns substantially facilitates interpretation of ice conditions and makes it possible to exclude a number of ambiguities. The method of processing and interpreting of patterns obtained by both radar lateral scanning and radiometric measurements by the PM-08 radiometer installed at the "Okean-01" satellite allows the general and partial close-packing for basic age types of sea ice in Arctic regions to be determined and their distribution to be mapped.

REFERENCES

1. V. P. Shestopalov, A. I. Kalmykov, V. A. Komyak, *et al.*, Dokl. Akad. Nauk SSSR **284**, 98 (1985).
2. *Radio Detection and Ranging of the Earth's Surface from Near Space*, Ed. by L. M. Mitnik and S. V. Viktorov (Gidrometeoizdat, Leningrad, 1990).
3. A. A. Goncharenko, V. F. Kravchenko, and V. I. Ponomarev, *Remote Probing of Nonhomogeneous Media* (Mashinostroenie, Moscow, 1991).
4. A. M. Volkov, in *Trudy Nauchn.-Issled. Tsentra po Izuch. Prirodn. Resursov*, No. 45, p. 80 (1999).
5. V. K. Volosyuk and V. F. Kravchenko, Zarubezh. Radioélektron. Usp. Sovrem. Radioélektron., No. 8, 3 (2000).
6. A. I. Kalmykov, V. B. Efimov, S. S. Kavelin, *et al.*, Issled. Zemli iz Kosmosa, No. 5, 84 (1984).
7. V. N. Chelomeĭ, G. A. Efremov, K. Ts. Litovchenko, *et al.*, Issled. Zemli iz Kosmosa, No. 2, 80 (1990).
8. E. H. Velten and G. H. Dieterle, in *Proceedings of the International Geoscience and Remote Sensing Symposium, IGARSS'86, Zürich, 1986*, p. 161.
9. A. P. Luscombe, in *Proceedings of the International Geoscience and Remote Sensing Symposium, IGARSS'88, Edinburgh, 1988*, p. 1027.
10. J. P. Holinger, J. L. Pierc, and G. A. Proc, IEEE Trans. Geoscience Remote Sensing **GE-28** (5), 781 (1990).
11. N. A. Armand, B. G. Kutuza, and V. A. Panchenko, in *Remote Sensing for Global Change, Climate Change, and Atmosphere and Ocean Forecasting: European "International Space Year" Conference, Munich, 1992*, p. 1063.
12. V. S. Blinov, A. K. Goncharov, O. L. Senkevich, *et al.*, *Tr. Nauchno-Proizvod. Ob"edin. "Planeta,"* Ser. A, No. 42, 33 (1993).
13. A. P. Pichugin and S. A. Shilo, Issled. Zemli iz Kosmosa, No. 1, 77 (1989).
14. A. P. Pichugin, L. V. Elenskiĭ, V. B. Efimov, *et al.*, Issled. Zemli iz Kosmosa, No. 6, 82 (1984).
15. V. V. Asmus, P. A. Nikitin, A. E. Popov, *et al.*, Issled. Zemli iz Kosmosa, No. 3, 107 (1985).

Translated by G. Merzon

Doklady Physics, Vol. 46, No. 2, 2001, pp. 107–109. Translated from Doklady Akademii Nauk, Vol. 376, No. 6, 2001, pp. 757–759.

TECHNICAL PHYSICS

A New Type of Structural Memory in Titanium Nickelide

V. I. Zel'dovich, N. Yu. Frolova, and I. V. Khomskaya

Presented by Academician B.V. Litvinov June 9, 2000

Received July 3, 2000

The effect of reversible shape memory (RSM) is usually associated with internal-stress fields due to dislocations [1]. If these fields are oriented in a certain way, then they induce a martensite transformation with the selection of a certain martensite orientation from all crystallographically possible orientations. The selection of the preferable orientation results in macroscopic deformation of the specimen, the so-called reversible shape memory deformation henceforth called the RSM deformation. In alloys based on titanium nickelide with nickel content exceeding the equiatomic value, aging processes [2] and precipitation of the Ti_3Ni_4 phase occur, which produce an essential effect on the subsequent martensite transformations [3]. The present study was undertaken with the aim to clarify the role of Ti_3Ni_4-particles in the formation of the reversible memory effect in titanium nickelide. We established that the austenitic-type reversible-memory effect and its preservation during thermal processing of specimens are provided by precipitation of the aging-phase particles (Ti_3Ni_4) with preservation of the texture in the particle arrangement.

The 2.2-mm-thick plates of the Ti–50.5 at. % Ni alloy were obtained by rolling the specimens in the austenitic state. The temperatures of martensite transformations and RSM deformation were studied by the dilatometric method on a Chevenard differential optical dilatometer. The specimens were cut out from the plates along the rolling direction. The measurements were made in the following sequence. Each specimen was first cooled to a temperature below the temperature M_f of the completion of the martensite transformation, then it was heated above the temperature A_f of the completion of the reverse martensite transformation, and, finally, was cooled to room temperature. The directions of dilatometric measurements are indicated by the arrows near the corresponding curves. Room temperature is shown by the vertical lines. The material structure was studied with the help of a JEM 200CX electron microscope.

Institute of Metal Physics, Ural Division, Russian Academy of Sciences, ul. S. Kovalevskoĭ 18, Yekaterinburg, 620219 Russia

Rolling with subsequent holding of the specimens for 3.6 ks at temperatures 523, 623, and 698 K only slightly affected the dilatometric curves of the martensite transformations. The curves indicate the austenite-type reversible memory effect characteristic of specimens rolled in the austenitic state [4]. Martensite transformations occurring during specimen cooling proceeded in the sequence B2 ⟶ R ⟶ B19'. During specimen heating, the sequence was B19' ⟶ B2 (curve *1* in Fig. 1). Holding of the specimens at temperatures 723, 248 K (curves *2* and *3* in Fig. 1) and, then, at 773 K (Fig. 2, curve *1*) reduced the temperatures of the martensite transformations and the RSM deformation. Comparing the dilatometric curves of martensite transformations upon specimen holding at 773 and 698 K (cf. curve *1* in Fig. 2 and curve *1* in Fig. 1), one can see that the RSM deformation is reduced by three times, whereas the temperatures of the martensite transformations decreased by 30 K. These changes indicate considerable variations in the structural state of the alloy.

However, the specimens preliminarily heated to 773 K and then held for 3.6 or 36 ks at 623 K showed

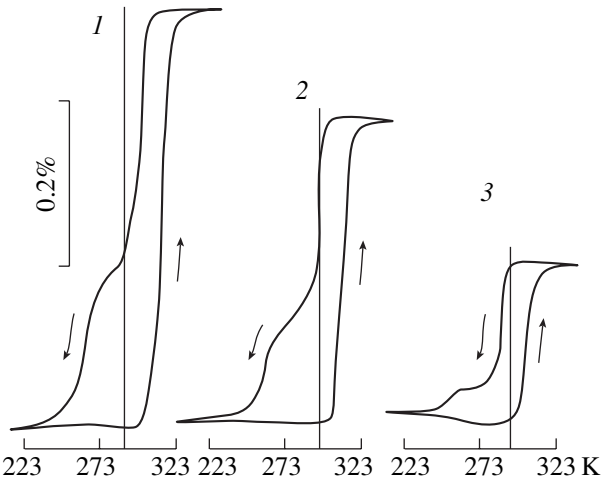

Fig. 1. Dilatometric curves of martensite transformations: (*1*) deformation with 3.6-ks-long holding of the specimen at 698 K; (*2*) the same as in (*1*) with 3.6-ks-long holding of the specimen at 723 K; (*3*) the same as in (*2*) with 3.6-ks-long holding of the specimen at 748 K.

1028-3358/01/4602-0107$21.00 © 2001 MAIK "Nauka/Interperiodica"

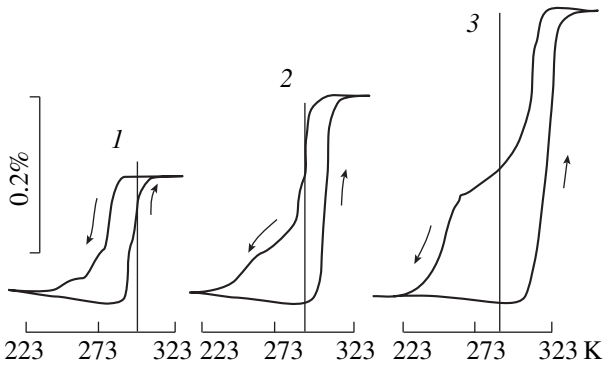

Fig. 2. Dilatometric curves of martensite transformations: (*1*) deformation with 3.6-ks-long holding of the specimen at 773 K; (*2*) the same as in (*1*) with 3.6-ks-long holding of the specimen at 623 K; (*3*) the same as in (*1*) with 36-ks-long holding of the specimen at 623 K.

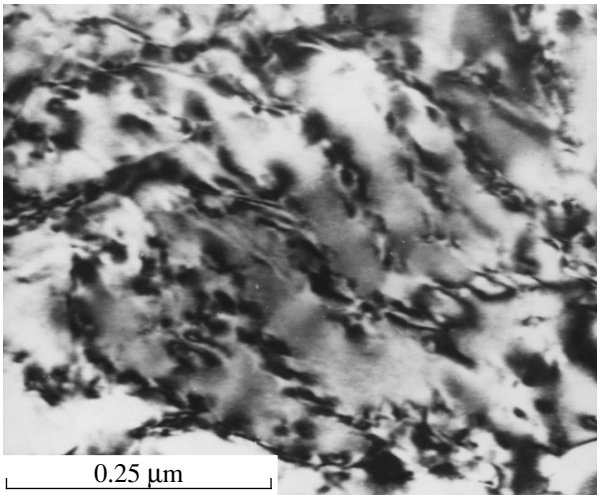

Fig. 3. Precipitation of Ti_3Ni_4 particles at subgrains. Deformation with 3.6-ks-long holding of the specimen at 773 K followed by 36-ks-long holding of the specimen at 623 K.

a more pronounced RSM deformation and higher temperatures of martensite transformations (curves *2* and *3* in Fig. 2). Upon 36-ks-long holding of the specimens at 623 K, the transformation temperatures become equal to the temperatures obtained upon heating of the deformed specimens at 623 K. The RSM deformation is restored, although only partly. These experiments indicate the existence of a specific type of the memory, the reversible shape memory, which we called the double memory. The existence of a double memory indicates that holding of the specimens preliminary heated to 773 K at the temperature 623 K provides, at least, partial restoration of the structural state of the alloy.

A decrease of RSM deformation with an increase of the specimen temperature to 723–773 K could be explained by the change in the internal-stress fields caused by rearrangement of the dislocation structure. However, the restoration of specimen deformation upon its reheating to 623 K is inconsistent with such an explanation. The decrease in the temperatures of martensite transformations upon specimen heating to 773 K and their increase during subsequent heating to 623 K indicate the occurrence of the processes of dissolution and precipitation of the Ti_3Ni_4 phase.

The aging process with precipitation of Ti_3Ni_4 particles in titanium-nickelide alloys containing 50.5 at. % Ni (and lower) has not been studied as yet. Our electron microscopy data show that at a temperature of 623 K, the precipitation of Ti_3Ni_4 particles takes place. Then, at 773 K, they are dissolved. Thus, in the alloy studied here, as well as in the alloys with higher Ni-content, the solubility of nickel in the TiNi intermetallic compound is temperature-dependent. Upon rolling in the austenitic state, the structure contained ~70-nm-long Ti_3Ni_4 particles formed during aging. The particles were oriented with their long axes along a certain preferable direction. Thus, rolling and cooling give rise to the aging process and, in addition to the deformation texture of the B2-phase, a texture in the particle arrangement arises. Thus, the reversible memory effect can be explained not only by the existence of a "crystallographic" and a "dislocation" texture in the B2-phase, but also by the texture in the arrangement of the Ti_3Ni_4 particles.

Holding of the specimens for 3.6 ks at 773 K results in dissolution of the Ti_3Ni_4 particles and polygonization of the B2-phase. Additional holding of the specimens at 623 K gives rise to a new aging process, whereas the Ti_3Ni_4 particles precipitate mainly at the subgrain boundaries, thus, forming a characteristic net (Fig. 3). Since martensite is nucleated at these particles [2, 3] orientationally related to the B2 matrix, the increase of the RSM deformation in the process of aging at 623 K (Fig. 2) can be explained by the reproduction of the texture in the particle arrangement. Thus, the reversible shape memory effect is associated with the memory of the texture in the arrangement of the Ti_3Ni_4 particles.

The cycles of particle precipitation and dissolution can be multiply repeated. Figure 4 illustrates the change in the temperatures of martensite transformations and RSM deformation upon alternating holdings of the specimen at 623 and 773 K. The alternating holding of specimens at 773 and 623 K gives rise to an alternating decrease and increase of the RSM deformation. Here, the Ti_3Ni_4 particles play a double role. Particle precipitation and the corresponding matrix depletion of nickel increase the temperatures of the martensite transformations. The texture in the particle arrangement and the martensite nucleation at these particles result in a selection of preferable martensite orientations and macroscopic RSM deformation. It should be emphasized that the processes of particle dissolution and precipitation take place in the deformed and polygonized B2-matrix at temperatures below the

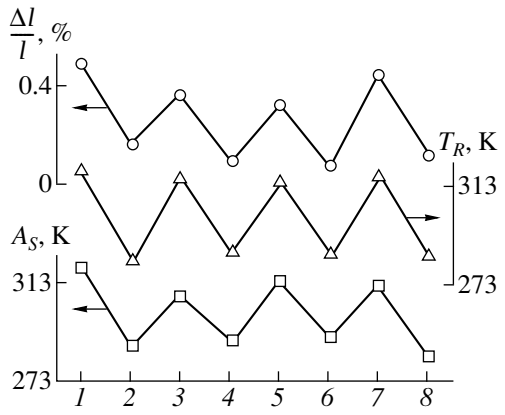

Fig. 4. The change in the RSM deformation $\frac{\Delta l}{l}$ and the temperatures T_R and A_S of initiation of the transformation B2 ⟶ R and B19' ⟶ B2, respectively, upon alternating holding of the specimen for 36 ks at 623 K and 3.6 ks at 773 K. (*1*, *3*, *5*, *7*) Holding of the specimen at 623 K; (*2*, *4*, *6*, *8*) holding of the specimen at 773 K.

recrystallization temperature, which provides the implementation of the reversible memory effect.

Heating of the specimens to 873 K results in dissolution and recrystallization of Ti_3Ni_4 particles. These processes are accompanied by complete disappearance of the reversible memory effect and reduction of the temperatures of the martensite transformations. Aging of specimens preliminarily heated up to 873 K during 36 ks and subsequent 360-ks-long holding at 623 K increases the temperatures of the martensite transformations, but the RSM deformation is not restored.

Thus, a new type of structural memory has been discovered in titanium nickelide, namely, reversible shape memory of the austenitic type. The reversible shape memory is associated with the processes of precipitation of the particles of the aging Ti_3Ni_4 phase fixing the dislocation structure. In the alloys where the dissolution temperature of the Ti_3Ni_4-particles is lower than the temperature of their recrystallization, the RSM deformation can be controlled by varying the processes of particle dissolution and precipitation.

ACKNOWLEDGMENTS

This study was supported by the Russian Foundation for Basic Research, project no. 99-02-16645.

REFERENCES

1. V. A. Likhachev, S. L. Kuz'min, and Z. P. Kamentseva, *Effect of Form Memory* (Leningr. Gos. Univ., Leningrad, 1987).
2. M. Nishida, C. M. Wayman, and T. Honma, Metal. Trans. A **17A**, 1505 (1986).
3. V. I. Zel'dovich, G. A. Sobyanina, and V. G. Pushin, Scr. Mater. **37** (1), 79 (1997).
4. V. I. Zel'dovich, V. G. Pushin, N. Yu. Frolova, *et al.*, Fiz. Met. Metalloved., No. 8, 90 (1990).

Translated by L. Man

Doklady Physics, Vol. 46, No. 2, 2001, pp. 110–112. Translated from Doklady Akademii Nauk, Vol. 376, No. 4, 2001, pp. 471–473.

MECHANICS

Hereditary-Type Model of a Nonlinear Medium with Allowance for Temperature and Humidity

S. I. Alekseeva

Presented by Academician V.P. Larionov June 16, 2000

Received June 16, 2000

Materials with pronounced viscous properties find ever increasing application in industry. These are polymer-matrix-based and pure polymer composites whose number and variety steadily increase. It is well known that various climatic factors such as temperature and humidity are very important for estimating the behavior and characteristics of these materials and, therefore, the derivation of constitutive equations with allowance for these factors is of key importance for modern machine building.

In this paper, we use as the constitutive equation the Rabotnov nonlinear equation [1]

$$\varphi(\varepsilon) = \sigma + \int_0^t K(t-\tau)\sigma(\tau)d\tau, \qquad (1)$$

where $\varphi(\varepsilon)$ is the curve of instantaneous deformation, $K(t-\tau)$ is the kernel of the integral equation in the form of the Abel kernel,

$$K(t-\tau) = \frac{k}{(t-\tau)^{\alpha}},$$

proved to be very efficient in nonlinear equations [2, 3, etc.].

The problem of allowance for temperature and humidity is considered in a large number of studies, in which the temperature and humidity are artificially introduced into the constitutive equation. In other words, all the kernel parameters and the curve of instantaneous deformation (or, in the linear case, the elastic modulus) are assumed to be dependent on both temperature and humidity. Evidently, the determination of these dependences requires vast experimental information, which is not always available.

We should invoke here the principle of analogies still widely used in engineering practices (see [4–6, etc.]). The difficulty here is the determination of the entire set of necessary parameters whose number is very large in the nonlinear case. In turn, this makes their determination ambiguous. Moreover, considerable difficulties also arise in attempts to solve particular nonlinear mechanical problems.

In [7], another method of taking into account the temperature was suggested and tested on many materials with pronounced viscous properties. The method is based on the fact that the $\varphi(\varepsilon)$ curve, being the curve of instantaneous deformation, is also the curve of the absolute-zero temperature. The corresponding equation is written as

$$\varphi(\varepsilon) = \sigma + \int_0^t K(t-\tau)f(T)\sigma(\tau)d\tau.$$

If the process proceeds at an infinitely high rate (i.e., with $t = 0$ at a certain temperature) or at an arbitrary rate, but at the absolute zero, we arrive at $\sigma = \varphi(\varepsilon)$, i.e., at the equation of a curve limiting the possible deformation process from above. It was also shown that the function of temperature effect can be an exponential function $f_1(T) = T^{\gamma}$, where T is the temperature in Kelvins. It is expedient to take

$$f_1(T) = \left(\frac{273 + T^{\circ}\mathrm{C}}{273}\right)^{\gamma}. \qquad (2)$$

In this paper, we propose the principle of allowance for humidity in the constitutive equation proceeding from the same premises as were used in allowance for temperature. We introduce the function of humidity effect $f_2(W)$, where W is a relative increment in weight (expressed in percent) due to absorption of moisture:

$$f_2(W) = \left(\frac{W_0 + W(\text{wt }\%)}{W_0}\right)^{\beta}. \qquad (3)$$

Here, W_0 is an empirical constant which can conditionally be taken as the relative decrease in the material weight (expressed in percent) under the conditions of room humidity compared to the weight of an absolutely dry material.

Blagonravov Institute of Engineering Science, Russian Academy of Sciences, ul. Griboedova 4, Moscow, 101830 Russia

1028-3358/01/4602-0110$21.00

The constitutive equation takes the form

$$\varphi(\varepsilon) = \sigma + \int_0^t \frac{k}{(t-\tau)^\alpha}\left(\frac{273 + T^\circ\mathrm{C}}{273}\right)^\gamma \times \left(\frac{W_0 + W(\text{wt }\%)}{W_0}\right)^\beta \sigma(\tau)d\tau. \quad (4)$$

The introduction of the humidity function into the constitutive equation in the above form is justified by available experimental data. It was shown that an increase of humidity lowers the position of the deformation curve and enhances the effect of creep. On the other hand, the material drying "suppresses" viscous effects and the deformation curve approaches the curve of instantaneous deformation. This fact implies the choice of the function of humidity effect in the same form as that of the temperature effect. Experiments on the humidity effect are labor-consuming and require meticulous measurements and special instruments. Thus, the number of relevant published data is scarce, which, in turn, hinders testing of the suggested equation.

An important problem is the construction of a scale of moisture saturation, which requires at least two reference points. For temperature, the reference points (in the Celsius scale) are the ice melting point (0°C) and water boiling point (100°C). In the SI system of units, temperature is measured in kelvins. The first reference point is 0 K or the absolute-zero temperature (–273°C); the other reference point is the triple-point of water, 273 K (0°C). Thus, the function of temperature effect $f_1(T)$ is taken to be relationship (2). Unfortunately, there is no reliable scale for determining the level of moisture saturation. Nevertheless, the magnitude W_0 in Eq. (3) has a quite definite physical meaning. If, on material drying, W(wt %) becomes equal to $-W_0$, then $f_2(W) = 0$ and, in accordance with Eq. (4), we arrive at the equation for the instantaneous curve $\sigma = \varphi(\varepsilon)$, irrespective of other loading conditions. The value of the quantity W_0 should be one of the reference points for constructing the scale of moisture saturation. The second reference point can be humidity under room conditions, $W = 0$.

The validity of similar representations is confirmed, e.g., in [8], where the effect of various media (including water) on the strength characteristics of polymethyl methacrylate is considered. It was also shown that at a low loading rate (1×10^{-3} s^{-1}), the medium reduces the strength and increases the viscous effects (thus, in water, the strength decreases by 18%; in acetone, by 56%). With an increase in the loading rate by an order of magnitude, the effect of the media becomes rather weak. Thus, irrespective of the material saturation with various components and the rate tending to infinity, the deformation curve approaches the instantaneous curve, which justifies the initial premises used for the construction of Eq. (4).

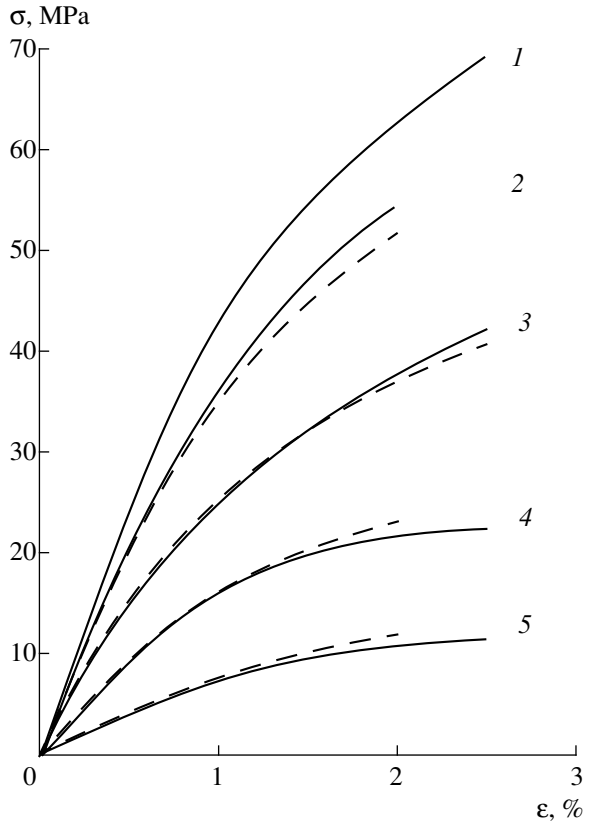

Fig. 1. Deformation curves for PN-3 polyester resin obtained under a constant loading rate $\dot{\varepsilon} = 5.5 \times 10^{-3}$ min^{-1} and at various temperatures and a moisture value $W = 0.2$ wt %. Solid lines correspond to experiment [6]. Dashed lines were calculated by Eq. (4). (*1*) φ(ε); (*2*) 0; (*3*) 20; (*4*) 40; (*5*) 60°C.

As an example, we consider the results of the experiments on the combined effect of the temperature and humidity on the deformation and creep curves of PN-3 polyester resin [5, 6]. The parameters of Eq. (4) were calculated as is described in [9]. It should be emphasized that the reason for determining the parameters of the humidity function is the same as for determining the function of temperature described in detail in [10]. Thus, we obtained the following values: $\alpha = 0.93$; $k = 0.02$ min$^{-(1-\alpha)}$; $\gamma = 13.27$; $W_0 = 3.45$ wt %; and $\beta = 2.5$. The calculated instantaneous curve of deformation, φ(ε), is shown in Fig. 1. Figure 1 also shows the experimental data and the data calculated by Eq. (4) at $W = 0.2$ wt % and different temperatures. Figure 2 shows the experimental and calculated creep curves at different levels of saturation with moisture at 40°C. It should be indicated that, as was shown in studies [5, 6], the humidity at 20°C only slightly affects the creep curves. Indeed, at the moisture change from 0.2 to 1.5 wt %, five-hour loading gives rise to 0.3% strain, whereas the same loading at 40°C yields a strain exceeding 3%.

The above results prove the necessity of the simultaneous allowance for both temperature and humidity

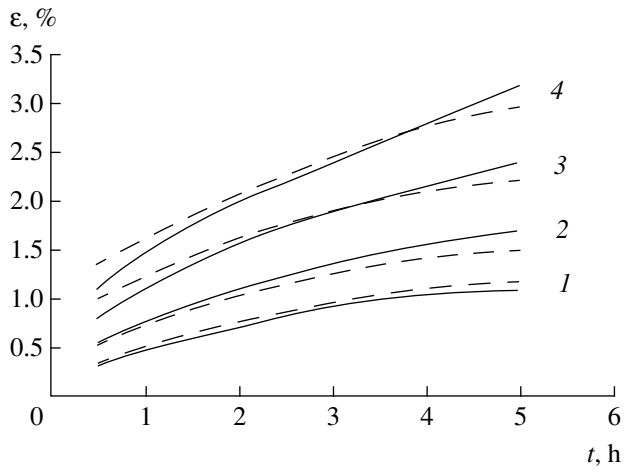

Fig. 2. Creep curves σ = 12 MPa for PN-3 polyester resin at different humidity values at T = 40°C. Solid lines indicate experiment [5]. Dashed lines are calculated by Eq. (4). (*1*) 0.2; (*2*) 0.5; (*3*) 1.0; (*4*) 1.5 wt %.

and the importance of constructing reliable constitutive equations for calculating the structure elements operating in various modes.

If the temperature and humidity in the problem under study remain constant, irrespective of their values, Eq. (4) is used in the same way as Eq. (1), with the only difference being the kernel parameter (a multiplier before the integral) recalculated according to (2) and (3). The possibility of using Eq. (4) for the processes with varying temperature and constant humidity was shown in [2]. As far as we know, no experiments with variable humidity have yet been made.

It should be emphasized that the combined effect of the temperature and humidity on material behavior can be more complicated than the behavior described by Eq. (4). Here, some secondary effects are also possible.

ACKNOWLEDGMENTS

This study was supported by the Russian Foundation for Basic Research, project no. 98-01-00969.

REFERENCES

1. Yu. N. Rabotnov, *Elements of Hereditary Mechanics of Solids* (Nauka, Moscow, 1977).
2. J. V. Suvorova, in *Failure Mechanics of Composites* (North-Holland, Amsterdam, 1985), Vol. 3, pp. 177–214.
3. Yu. V. Suvorova, A. E. Vasil'ev, G. P. Mashinskaya, and G. N. Finogenov, Mekh. Kompoz. Mater., No. 5, 847 (1980).
4. J. D. Ferry, *Viscoelastic Properties of Polymers* (Wiley, New York, 1961; Inostrannaya Literatura, Moscow, 1963).
5. Yu. S. Urzhumtsev and R. D. Maksimov, *Prognostication of the Deformability of Polymer Materials* (Zinatne, Riga, 1975).
6. V. P. Mochalov, N. I. Aniskevich, and R. D. Maksimov, Mekh. Polim., No. 4, 579 (1972).
7. Yu. V. Suvorova, Probl. Prochn., No. 2, 43 (1977).
8. A. N. Tynnyĭ, Yu. A. Kolevatov, A. I. Soshko, and N. G. Kalinin, Fiz.-Khim. Mekh. Mater. **5**, 677 (1969).
9. A. E. Osokin and Yu. V. Suvorova, Prikl. Mat. Mekh. **42**, 1107 (1978).
10. S. I. Alekseeva, Zavod. Lab., No. 7, 32 (1994).

Translated by V. Bukhanov

Doklady Physics, Vol. 46, No. 2, 2001, pp. 113–118. Translated from Doklady Akademii Nauk, Vol. 376, No. 4, 2001, pp. 474–479.

MECHANICS

Atomic Functions in the Problem of Evaluating the Rayleigh Functions and the Precession Coefficient for the Resonator of a Wave Solid-State Gyroscope

M. A. Basarab*, V. F. Kravchenko, V. A. Matveev*, and Corresponding Member of the RAS V. I. Pustovoĭt*****

Received October 16, 2000

INTRODUCTION

In modern practice, increasingly rigid requirements are being imposed on sensitive elements of navigational systems. Unconventional gyro devices designed on the basis of new physical principles are necessitated. One of such a class of devices is that generally referred to as Foucault pendulums. Among them, the micromechanical vibrational gyroscope, string gyroscope, ring gyroscope, etc. are well known. This paper is devoted to studying the properties of sensitive elements (sensors) of wave solid-state gyroscopes [1, 2] whose operation principle is based on using inertia features of standing waves excited in revolving axial-symmetric shells. This effect was discovered theoretically and confirmed experimentally by G. Bryan in 1890 [3]. The fundamentals of the analytical theory and mathematical modeling of elastic processes in resonators of solid-state wave gyroscopes were given in [1, 2, 4–9]. As a rule, the authors of these papers dealt with sensors in the form of either an elastic ring or canonical shells of revolution (cylinder, cone, quadric shells). In this paper, we first consider the use of atomic functions [10] which allow us to determine dynamic characteristics of sensitive elements for arbitrary-shape gyroscopes.

STATEMENT OF THE PROBLEM

Let a shell of revolution be either bounded by two parallel lines of this shell or dome-shaped. We assume the boundary conditions to be linear and homogeneous and introduce an orthogonal coordinate system related to the meridians and parallels of its median surface. The arc length s ($0 < s_1 < s < s_2$) of the generatrix and the azimuth angle φ ($0 < \varphi < 2\pi$) are taken as curvilinear coordinates. We denote by $B(s)$ and θ ($\theta_1 < \theta < \theta_2$) the distance to the axis of revolution and the angle between the inner normal to the shell and the axis of revolution, respectively. It is well known that the rotation of an axial-symmetric shell is accompanied by splitting (caused by the action of Coriolis forces) of the normal modes for bending vibrations and results in a precession of standing waves. Under the simplifying assumption on inextensible parallels, the standing-wave precession coefficient for a revolving shell is given by the formula [7]

$$K = -\frac{\int_{s_1}^{s_2} V(U\cos\theta + W\sin\theta)B(s)ds}{\int_{s_1}^{s_2} (U^2 + V^2 + W^2)B(s)ds}, \qquad (1)$$

where $U(\theta)$, $V(\theta)$, and $W(\theta)$ are the Rayleigh functions [11] determined by the shell geometry, boundary conditions, and the vibrational-mode number n, i.e., the number of waves in a parallel. In practice, it is inconvenient to use formula (1) directly, except for the case of a narrow class of axial-symmetric canonical shells for which an expedient system of curvilinear coordinates can be chosen. In this case, the Rayleigh function can, as a rule, be found analytically. The problem is to develop a new mathematical model allowing these functions to be evaluated for arbitrary shells of revolution.

DERIVING DIFFERENTIAL RELATIONSHIPS FOR THE RAYLEIGH FUNCTIONS

We introduce the cylindrical coordinates r, z, and φ, with the z-axis directed along the symmetry axis. In this

* *Bauman State Technical University, Vtoraya Baumanskaya ul. 5, Moscow, 107005 Russia*

** *Institute of Radio Engineering and Electronics, Russian Academy of Sciences, ul. Mokhovaya 11, Moscow, 103907 Russia*

*** *Central Design Bureau of Unique Instrumentation, Russian Academy of Sciences, ul. Butlerova 15, Moscow, 117342 Russia*

1028-3358/01/4602-0113$21.00

case, the following expressions for the displacement components u_r, u_z, and u_φ hold:

$$u_r = U\cos\theta + W\sin\theta,$$
$$u_z = -U\sin\theta + W\cos\theta, \quad u_\varphi = \frac{V}{r}. \tag{2}$$

If the inextensibility conditions for the median surface are satisfied, then $U\cos\theta + W\sin\theta = nV$. In the new notation, expression (1) takes the form

$$K = \frac{n\int_{z_0}^{Z} u_\varphi^2 r^3 \sqrt{1+(r')^2}\,dz}{\int_{z_0}^{Z} [r^2(n^2+1)u_\varphi^2 + u_z^2] r\sqrt{1+(r')^2}\,dz}, \tag{3}$$

where $z_0 = z(s_1)$ and $Z = z(s_2)$. In the case of an inextensible shell, the functions $u_r(z)$, $u_z(z)$, and $u_\varphi(z)$ are determined from the following equations [11]:

$$\frac{1}{r^2}(r^2 u_\varphi')' + n^2\frac{r''}{r}u_\varphi = 0,$$
$$u_r = nru_\varphi, \quad u_z = -r\left(nr'u_\varphi + \frac{r}{n}u_\varphi'\right). \tag{4}$$

Introducing the notation $y(z) = ru_\varphi(z)$, we assume that $y(z_0) = 0$ (rigid fixing) and the boundary $z = Z$ is free. Since the Rayleigh functions are defined with an accuracy to a constant nonvanishing factor [11], we can assume that $y(Z) = C$, where C is an arbitrary nonvanishing constant. Let $C = 1$. In this case, the function $y(z)$ is a solution to the boundary value problem for the ordinary differential equation of the second order:

$$y'' + (n^2 - 1)\frac{r''}{r}y = 0, \quad y(z_0) = 0, \quad y(Z) = 1. \tag{5}$$

Employing the change of variables $y(z) = u(z) + u_0(z)$, with $u_0(z) = \dfrac{z - z_0}{Z - z_0}$, we reduce problem (5) to that with homogeneous boundary conditions:

$$u'' + t(z)u = f(z), \quad u(z_0) = 0, \quad u(Z) = 0. \tag{6}$$

Here,

$$t(z) = (n^2 - 1)\frac{r''}{r}, \quad f(z) = -t(z)u_0.$$

In the case of an arbitrary shell with its generatrix described by the expression $r = r(z)$, problem (6) can only be solved numerically. As follows from (4), to determine the displacement components u_z at arbitrary points, the first derivative of the solution to problem (5) should also be evaluated. Hence, if the method of finite differences is employed to solve this problem, an additional approximation to the function $y(z)$ in the gaps between net nodes is required. To avoid this, it is advisable to seek a solution to problem (5) in the class of continuously differentiable functions. We employ one of the projecting-net methods, with properly chosen basis functions. The method of collocations is the simplest for numerical simulations. It yields adequate results if finite functions are chosen as basis functions. Recently, the theory of atomic functions is being widely used for solving various problems of numerical analysis [10, 12–14].

ATOMIC FUNCTIONS up(x) AND fup$_n$(x)

The simplest atomic function up(x) satisfies the following functional–differential equation:

$$\mathrm{up}'(x) = 2\mathrm{up}(2x+1) - 2\mathrm{up}(2x-1),$$
$$\mathrm{supp\ up}(x) = [-1; 1], \quad \mathrm{up}(x) \in C^\infty(-\infty; \infty).$$

The function up(x) is even, with up(0) = 1. It increases (decreases) in the interval [–1; 0] ([0; 1]), with up$(1 - x) = 1 - \mathrm{up}(x)$. The following recurrence relations hold for the moments of up(x):

$$a_0 = 1, \quad a_{2n} = \frac{(2n)!}{2^{2n} - 1}\sum_{k=1}^{n}\frac{a_{2n-2k}}{(2n-2k)!(2k+1)!},$$
$$b_{2n+1} = \frac{1}{(n+1)\times 2^{2n+3}}\sum_{k=0}^{n+1} a_{2n+2}.$$

Here,

$$a_{2n} = \int_{-1}^{1} x^{2n}\mathrm{up}(x)\,dx \text{ and } b_n = \int_{0}^{1} x^n \mathrm{up}(x)\,dx.$$

The values of the function up(x) at the points $\dfrac{k}{2^n}$ are rational numbers; in particular,

$$\mathrm{up}(-1 + 2^{-n}) = \frac{b_{n-1}}{2^{n(n-1)/2}(n-1)!}.$$

To find up(x) at an arbitrary point, the convergent series of the form

$$\mathrm{up}(x-1) = \sum_{k=1}^{\infty}(-1)^{s_k+1}p_k \times \sum_{j=0}^{k}\frac{2^{((j+1)j-(k-j)(k-j-1))/2}b_{k-j-1}}{(k-j-1)!\,j!}(x-0, p_1 \ldots p_k)^j$$
$$0 \le x < 1,$$

is used. Here,

$$b_{-1} = 1, \quad s_k = \sum_{j=1}^{k} p_j$$

and $x = 0$, $p_1 \ldots p_k$ is the binary representation of the number x. The recurrence functional–differential relations for the determination of atomic functions $\mathrm{fup}_n(x)$ are similar to the equations for the Schönberg B_n-splines:

$$y_n'(x) = K\left\{y_{n-1}\left(x-\frac{1}{2}\right) - y_{n-1}\left(x+\frac{1}{2}\right)\right\},$$

$$y_0(x) = \mathrm{up}(x),$$

where K is a normalization factor. It follows from these equations that

$$\mathrm{supp}\,\mathrm{fup}_n(x) = \left[-\frac{n+2}{2}; \frac{n+2}{2}\right].$$

In this interval, the function $\mathrm{fup}_n(x)$ can be represented as

$$\mathrm{fup}_n(x) = \sum_{i=0}^{m+1} \alpha_i^{(m)} \mathrm{up}\left[2^{-m}\left(x - 2^m + \frac{m}{2} + 1 - i\right)\right],$$

$$\alpha_0^{(m)} = 1, \quad \alpha_i^{(m)} = (-1)^i C_{m+1}^i - \sum_{j=0}^{i-1} \alpha_j^{(m)} \delta_{i-j+1},$$

$$\delta_1 = 1, \quad \delta_{2k} = -\delta_k, \quad \delta_{2k-1} = \delta_k.$$

We approximate the function $f(t) \in C^r[-\pi; \pi]$, given at the equidistant net Δ_N: $t_i = ih$, $h = \frac{\pi}{N}$ $(i = \overline{-N, N})$, with the help of elements of the space $\mathrm{UP}_{N,r}$, i.e., by linear superpositions of the functions $\mathrm{up}(x)$ with their arguments translated and scaled:

$$\sum_k d_k \mathrm{up}\left(\frac{x+\pi}{2^r h} - k \times 2^{-r}\right).$$

We assume that r is an even number and the functions $f(t)$ are given at the points

$$\tau_k = kh, \quad k = \overline{-N - \frac{r}{2}, N + \frac{r}{2}}.$$

The space $\mathrm{UP}_{N,r}$ has a basis consisting of the finite function $\mathrm{fup}_r(x)$ with translated and scaled arguments. The approximation of the rth order of the function $f(t)$ by atomic functions is performed according to the expression

$$\Phi_{N,r}(f; t) = \sum_{k=-N-r/2}^{N+r/2} c_k \varphi_{r,k}(t).$$

Here, $\varphi_{r,k}(t) \equiv \mathrm{fup}_r\left(\frac{t+\pi}{h} - k\right)$ and the support for $\varphi_{r,k}(t)$ is defined by the inequality $|t - \tau_k| \le \frac{r+2}{2} h$. It is known [10] that, for arbitrary $\forall h > 0$, there exist the numbers $\exists c_k$ such that

$$\| f(x) - \Phi_{N,r}(f; x) \|_{C^l[-\pi;\pi]} \le K_r h^{r-l} \omega_r(f; h),$$

where $\omega_r(f; h)$ is the continuity modulus of the function $f^{(r)}(x)$, with K_r independent of h (but dependent on r).

THE METHOD OF SOLVING

We introduce the equidistant net

$$z_i = z_0 + ih, \quad i = 0, 1, \ldots, N, \quad h = \frac{Z - z_0}{N} \qquad (7)$$

and the notation $t_i = t(z_i)$, $f_i = f(z_i)$, and $u_i = u(z_i)$. We seek the approximate solution $u^*(z)$ to problem (6) as a linear superposition of the atomic function $\mathrm{fup}_2(x)$ with its argument translated and scaled which satisfies the above conditions:

$$u^*(z) = \sum_{j=-1}^{N+1} d_{j+1} \psi_j(z), \qquad (8)$$

where

$$\psi_j(z) = \mathrm{fup}_2\left(\frac{z - z_0}{h} - j\right), \quad \sum_{j=-\infty}^{\infty} \psi_j(z) \equiv 1. \qquad (9)$$

The indeterminate coefficients d_i, $i = 0, 1, \ldots, N + 2$ are found from the set of linear algebraic equations:

$$Ad = b. \qquad (10)$$

The components of the matrix A and vector b are determined from the collocation conditions

$$A_{i+1,j} = \psi_{j-1}''(z_i) + t_i \psi_{j-1}(z_i), \quad b_{i+1} = f_i,$$
$$i = 1, 2, \ldots, N, \quad j = 0, 1, \ldots, N + 2$$

at the nodes z_i, the boundary conditions

$$A_{0,j} = \psi_{j-1}(z_0), \quad A_{N+2,j} = \psi_{j-1}(Z),$$
$$j = 0, 1, \ldots, N + 2; \quad b_0 = b_{N+2} = 0;$$

and an additional (fairly arbitrary) condition for interpolation by the atomic function:

$$A_{1,j} = \psi_{j-1}''(z_0), \quad j = 0, 1, \ldots, N + 2; \quad b_1 = 0.$$

The following theorem takes place.

Theorem. *If* $u(z) \in C^4[z_0; Z]$ *is an exact solution to problem* (6)*, then the following estimate for the error of approximated solution* (8) *holds*:

$$\|u(z) - u^*(z)\|_{C[z_0;Z]} \le \frac{h^2}{12} \max_{z \in [z_0;\ Z]} \left| \frac{u^{IV}(z)}{t(z)} \right|. \qquad (11)$$

NUMERICAL SIMULATION

Quadric shells of revolution. The method proposed allows us to evaluate the precession coefficient K for both canonical shells of revolution (ellipsoid and paraboloid of revolution, two-sheeted hyperboloid) and various complex-shaped shells. For dome-shaped quadric shells of revolution, the use of the net with $N = 8$ provides a good coincidence with the results obtained analytically (within an absolute error of about 10^{-4}) [8]. In both cases, the thickness of the arm fixing the segment on the base ($\theta_1 = 0$) was ignored. For the case of $\theta_1 > 0$, it was proposed in [9] to employ the method of successive integrations, which significantly complicates the problem and leads to cumbersome calculations. In the case under consideration with $\theta_1 > 0$, by virtue of the boundary conditions, the strain components u_r, u_φ, and V turn out to be vanishing. Table 1 presents the calculated values of the precession coefficient for a spherical segment at certain values of θ_1 and θ_2. For comparison, similar data taken from [9] are also presented in Table 2. The data obtained suggest that the arm is noticeably efficient only at sufficiently large θ_1 (from ~30° to 45°). This is explained by the fact that only that part of the shell which is close to its free boundary is mainly involved in the vibration. In this case, the rate of precession of the standing oscillatory wave increases slightly because the coupling between the wave and the base is enhanced. Variations of the angle θ_2 more considerably affect the precession. The results obtained are consistent both qualitatively and quantitatively with those given in [8, 9].

Table 1. Calculated values of the precession coefficient for a spherical segment at various angles θ_1 and θ_2

θ_1	$\theta_2 = 80°$	$\theta_2 = 90°$	$\theta_2 = 100°$
0°	0.7631	0.7230	0.6868
15°	0.7634	0.7231	0.6868
30°	0.7675	0.7254	0.6880
45°	0.7881	0.7371	0.6943

Table 2. Values of the precession coefficient for a spherical segment at various angles θ_1 and θ_2 (according to the data of [9])

θ_1	$\theta_2 = 80°$	$\theta_2 = 90°$	$\theta_2 = 100°$
0°	0.7632	0.7230	0.6867
15°	0.7632	0.7230	0.6867
30°	0.7635	0.7231	0.6867
45°	0.7681	0.7254	0.6878

Shells with zero curvature. We now consider cylindrical and conical shells. In this case, solving system (6) is simplified because $t(z) = f(z) = 0$; i.e., $u(z) = u_0(z)$. Transposing equality (3), we obtain for a cylindrical shell ($r = a$),

$$K = \frac{-n}{n^2 + 1 + \frac{3}{n^2}\left(\frac{a}{Z - z_0}\right)^2}. \qquad (12)$$

For the fundamental mode of vibration ($n = 2$), in the limit as $Z \longrightarrow \infty$, we have $K \longrightarrow -0.4$. The same value of the scaling coefficient is yielded by the ring model for the resonator of a wave solid-state gyroscope [2]. In the case of a conical shell ($r = \lambda z$), we have the following expression for the precession coefficient:

$$K = \frac{-n}{n^2 + 1 + n^2\lambda^2}. \qquad (13)$$

According to [8], the scaling coefficients for cylindrical and conical shells must take the forms, respectively,

$$K = \frac{-2}{n^2 + 1 + \frac{3}{n^2}\left(\frac{a}{Z - z_0}\right)^2}, \qquad (14)$$

$$K = \frac{-2}{n^2 + 1 + n^2\lambda^2}. \qquad (15)$$

In the case of $n = 2$, formulas (12) and (13) coincide with (14) and (15). It is worth noting that, for shells with zero curvature, the extension of the median surface is more significant compared to that for shells with positive curvature. Results disregarding this extension can be treated only as qualitative ones [8].

Complex-shaped shells. The case of the shell directrix described by a piecewise continuous function is of particular interest. In this case, the solution to problem (6) should be sought in the class of distributions. As an example, we consider a shell consisting of two bodies linked in the plane $z = c$, namely, a cone with its vertex at the origin and a cylinder of radius a and length $l = Z - c$ (Fig. 1):

$$r(z) = \frac{a}{c} z\eta(c - z) + a\eta(z - c).$$

Here, $\eta(z)$ is the Heaviside step function:

$$\eta(z) = \begin{cases} 0, & z < 0 \\ 1, & z \geq 0. \end{cases}$$

It is known that

$$\eta'(z) = \delta(z),$$

where $\delta(z)$ is the Dirac delta-function. Using its basic properties, it is easy to prove that

$$\frac{r''}{r} = \frac{-\delta(z-c)}{z + (c-z)\eta(z-c)}.$$

To evaluate the indeterminate coefficients in expansion (8), we employ the Galerkin method. We seek an approximate solution in the form

$$u^*(z) = \omega(z) \sum_{j=-1}^{N+1} d_{j+1}\psi_j(z),$$

where $\omega(z)$ is a function satisfying the homogeneous boundary conditions

$$\omega(z) = z(Z-z).$$

With regard to the properties of the Dirac delta-function, the elements of the matrix A and the components of the vector b in Eq. (10) are found by the Galerkin method in the form

$$A_{ij} = \int_0^Z \{[\omega(z)\psi_{i-1}(z)]'' + t(z)\omega(z)\psi_{i-1}(z)\}$$

$$\times \omega(z)\psi_{j-1}(z)dz = \int_0^Z [\omega(z)\psi_{i-1}(z)]''\omega(z)$$

$$\times \psi_{j-1}(z)dz - \frac{n^2-1}{c}\omega^2(c)\psi_{i-1}(c)\psi_{j-1}(c),$$

$$b_j = \int_0^Z f(z)\omega(z)\psi_{j-1}(z)dz = \frac{n^2-1}{cZ}\omega(c)\psi_{j-1}(c),$$

$$i, j = 0, 1, \ldots, N+2.$$

When evaluating the precession coefficient K by formula (3), it should be taken into account that

$$r' = \frac{a}{c}\eta(c-z).$$

Let $a = Z$. Varying the parameter c from zero to Z, we can prove that the coefficient K changes continuously from a minimum of 0.6522 to a maximum of 0.7778, which correspond to a cylinder and cone, respectively. These limiting values coincide with those obtained by formulas (12) and (13).

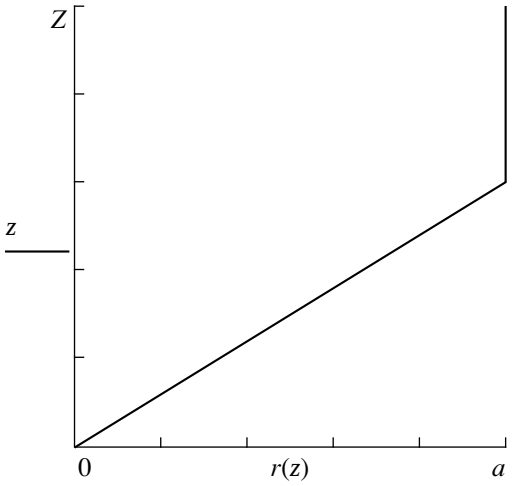

Profile of the complex-shaped shell.

CONCLUSIONS

The proposed and substantiated method of finding the Rayleigh functions and precession coefficient for shells of revolution has a number of advantages when compared to analytical methods. It allows us to perform calculations for shells of arbitrary shapes. The new method is suitable for numerical simulations. The use of atomic functions as basis functions enables us to solve boundary value problem (6) and makes finding coefficient (3) more simple. The precession coefficients evaluated for a wide class of shells are in good agreement with the theoretical results obtained by different methods [2, 6, 8, 9]. Numerical analysis indicates that the method proposed can be used for designing wave solid-state gyroscopes and allows us to optimize their basic dynamic characteristics.

ACKNOWLEDGMENTS

The authors are grateful to Academician of the National Academy of Sciences of Ukraine V.L. Rvachev for valuable discussions of the results obtained.

REFERENCES

1. V. F. Zhuravlev and D. M. Klimov, *A Wave Solid-State Gyroscope* (Nauka, Moscow, 1985).
2. V. A. Matveev, V. I. Lipatnikov, and A. V. Alekhin, *Designing of a Gyroscope Based on Elastic Waves in Solids* (Moscow, 1997).
3. G. H. Bryan, Proc. Cambridge Philos. Soc. **7**, 101 (1890).

4. V. F. Zhuravlev and D. M. Klimov, Izv. Akad. Nauk SSSR, Mekh. Tverd. Tela, No. 5, 17 (1983).
5. V. F. Zhuravlev and A. L. Popov, Izv. Akad. Nauk SSSR, Mekh. Tverd. Tela, No. 1, 147 (1985).
6. V. A. Matveev, O. S. Naraĭkin, and I. P. Ivanov, Izv. Akad. Nauk SSSR, Mashinostr., No. 7, 6 (1987).
7. N. E. Egarmin, Izv. Ross. Akad. Nauk, Mekh. Tverd. Tela, No. 4, 49 (1993).
8. M. A. Dzama and N. E. Egarmin, Izv. Akad. Nauk SSSR, Mekh. Tverd. Tela, No. 1, 170 (1991).
9. N. E. Egarmin, Izv. Akad. Nauk SSSR, Mekh. Tverd. Tela, No. 1, 142 (1986).
10. V. L. Rvachev and V. A. Rvachev, *Nonclassical Methods of Approximation Theory in Boundary Value Problems* (Naukova Dumka, Kiev, 1979).
11. J. W. Strutt (Lord Rayleigh), in *The Theory of Sound* (Macmillan, London, 1894; Gostekhizdat, Moscow, 1955), Vol. 1.
12. V. F. Kravchenko and V. A. Rvachev, Zarubezhn. Radioélektron., Usp. Sovrem. Radioélektron., No. 8, 6 (1996).
13. M. A. Basarab and V. F. Kravchenko, Élektromagn. Volny Élektron. Sist. **5** (4), 4 (2000).
14. M. A. Basarab, V. F. Kravchenko, and V. I. Pustovoĭt, Dokl. Akad. Nauk **374**, 324 (2000) [Dokl. Phys. **45**, 457 (2000)].

Translated by V. Chechin

Doklady Physics, Vol. 46, No. 2, 2001, pp. 119–123. Translated from Doklady Akademii Nauk, Vol. 376, No. 4, 2001, pp. 480–484.

MECHANICS

A Mechanism of Temporal Variation of Seismicity and Acoustic Emission prior to Macrofailure

L. R. Botvina*, P. N. Shebalin, and I. B. Oparina***

Presented by Academician V. I. Keĭlis-Borok March 13, 2000

Received June 7, 2000

Irregularity is a characteristic feature for time variation of the number of seismic events prior to an earthquake: lull periods in a preparation zone of a future earthquake are changed by the periods of relative activation. Increase in seismic activity in a wide zone around a future-earthquake focus was first noted by Keĭlis-Borok [1]. The phenomenon of seismic lull in a preparation zone of a strong earthquake was first described by Mogi [2]. Both precursor phenomena observed in the month–year time scale, being in apparent conflict, are quite consistent. The seismic lulls mentioned by Mogi occur against the background of activation in a wider zone ("doughnut pattern"). Both activation (in the foreshock form) and lull periods are observed prior to earthquakes in a shorter time scale [3]. Kosobokov and co-authors [4] have demonstrated the precursor character of local changing in activation and lull periods. Various scenarios for space–time variation of seismic activity prior to earthquakes were studied by a large number of authors.

In this paper, for constructing a model of irregular temporal change in seismic activity, we use data on acoustic emission in the process of metallic-specimen destruction. These data are compared with the results of analysis of time dependence for seismic events accumulated during a preparation period for earthquakes.

The well-known models for lull periods are based on either a temporal drop in tectonic stress or dilatancy hardening in a seismic-active zone, or on a bimodal distribution of rock strength in this zone. Variations of tectonic stress are related [3] to loss of strength as a result of rock sliding under creep conditions. Dilatancy hardening is associated with either a decrease of pore pressure in the Earth's crust when evolving fracturing or with the Kaiser effect [2, 5] observed in analysis of the acoustic emission for both metallic materials and rocks. The essence of this effect is the fact that a material, being repeatedly loaded, exhibits no acoustic-emission signals until the preceding loading level is attained. In other words, this effect of material "memory" assumes a change in the tectonic stress, i.e., its decrease and subsequent restoration in a lull period. The bimodal material's strength distribution for a medium may be a consequence of its random heterogeneity, i.e., the existence of the heterogeneities or roughnesses in the rupture plane [6].

The multiplicity of models proposed for the explanation of the same phenomenon testifies to the fact that its physical meaning, as well as constitutive factors, need to be elucidated. It is well known [2, 7, 8] that acoustic emission can be employed for analyzing seismicity. The characteristics of acoustic-emission development when destroying specimens of rock or model materials, in many instances, are similar to those of seismicity prior to an earthquake. Therefore, for understanding the nature of lull periods and the factors governing them, data records for the acoustic emission when destroying metal specimens were used. These data were compared with the results of the analysis for temporal dependence of seismic events accumulated in North California and certain other regions of the world during earthquake-preparation periods.

For constructing the temporal behavior of the events accumulated in North California, all principal events with a magnitude $M \geq 6$ found in the catalogue which occurred from 1976 to 1995 were selected. The aftershocks following these events were excluded. Thus, 16 such earthquakes were found. Then, the accumulated number of events with a magnitude $M \geq 3.5$ which occurred five years prior to the principal event was calculated for the spatial region of strong-earthquake preparation. This region was determined from the aftershock cloud for this earthquake. The results of these estimates are shown in Table 1.

In addition, similar temporal dependences were constructed for 32 earthquakes with $M \geq 7.5$ which occurred in various regions of the world. In Fig. 1a are shown typical temporal dependences for the accumulated number of events ΣN, the ratios S/N for the weight sum S [1] of the events to their number N, and

* *Baĭkov Institute of Metallurgy, Russian Academy of Sciences, Leninskiĭ pr. 49, Moscow, 117334 Russia*

** *International Institute of the Earthquake-Forecast Theory, Varshavskoe sh. 79, Moscow, 113556 Russia*

1028-3358/01/4602-0119$21.00

Table 1. Duration T_S of lull periods prior to principal events with a magnitude $M \geq 6$ in the North California region from 1976 to 1995

No.	Year	Month	Day	Hour	Min	Latitude	Longitude	Depth, km	M	T_S, days
1	1976	11	26	11	19	41.29°	125.71°	15	6.80	280
2	1980	5	25	19	44	37.57	118.82	15	6.70	53
3	1980	11	8	10	27	41.12	124.25	19	7.20	1190
4	1983	5	2	23	42	36.22	120.32	10	6.70	170
5	1984	4	24	21	15	37.32	121.70	8	6.20	540
6	1984	9	10	3	14	40.50	126.83	10	6.70	1200
7	1984	11	23	18	8	37.48	118.65	15	6.20	1160
8	1986	7	21	14	42	37.54	118.45	9	6.50	300
9	1987	7	31	23	56	40.42	124.41	16	6.00	250
10	1989	10	18	0	4	37.04	121.88	18	7.10	950
11	1991	8	17	19	29	40.24	124.35	12	6.30	175
12	1992	4	25	18	6	40.37	124.32	15	7.20	250
13	1993	5	17	23	20	37.17	117.78	6	6.20	270
14	1994	9	1	15	15	40.40	125.68	10	7.10	160
15	1994	9	12	12	23	38.82	119.65	14	6.10	780
17	1995	9	20	23	27	35.76	117.64	5	6.10	840

the exponent b in the well-known Gutenberg–Richter equation

$$\log N = \log C - bM,$$

relating the accumulated number of seismic events to their magnitudes. The weight sum for the events was calculated from the equation

$$S(t: M, \overline{M}, S, \alpha, \beta) = \sum 10^{\beta(M_i - \alpha)}.$$

The ratio S/N [1] yields the mean event magnitude determining the mean fracture length. Therefore, a sharp increase in the ratio S/N is indicative of a similarly sharp increase in the fracture length prior to an earthquake. As is evident from Fig. 1a, the dependence ΣN as a function of T has two plateaus separated by a region of sharp rise of the number of events accumulated prior to the earthquake. The length of the second plateau, which is 2.5 years in this case, determines the lull period. Its beginning in 1990 coincides with a sharp increase in the ratio S/N characterizing the fracture length and with a decrease in the exponent b. The latter fact was employed by a number of researchers [9] as one of the earthquake precursors. For the construction of temporal dependences for the accumulated number of acoustic-emission signals (ΣN), the results of tests of specimens made of steels of various qualities under conditions of stretching and bending [10, 11] were used. This information is of interest since it is obtained for materials of various strength and viscosity and for specimens of various geometric shapes (see Table 2). Moreover, it contains data on the experimental deformation curve (Fig. 1b), which makes it possible to evaluate the specimen destruction energy, as well as data of optical and electron microscopy accounting for the actual material vulnerability to damage at various stages of destruction development.

It is evident that curves ΣN as a function of T in Fig. 1b, obtained for metallic specimens from acoustic-emission data, are similar to the analogous curves in Fig. 1a, based on the results of seismic-activity analysis. Indeed, as in the first case, in the temporal dependence of the accumulated number of acoustic-emission signals, there exist two plateaus connected with one another by a segment having a sharp increase in ΣN. The onset of the second plateau corresponds to the minimum value of the signal amplitude A and to the break in the deformation curve $P(T)$ owing to a decrease in the strain-hardening coefficient. This decrease can be caused by a reduction in the plastically deformed volume and localization of the destruction (see Fig. 1b). Indeed, observation of the notch mouth with the help of an optical microscope revealed a microcrack with a size of ~0.5 mm (Fig. 1c) which appeared at the beginning of the acoustic-lull period and was absent prior to this moment. Further deformation of the specimen caused stable development of the crack (according to the pit-creation mechanism) until maximum loading was attained. Thereafter, this development was changed by the unstable increase of the crack according to the cleavage mechanism, which proceeded up to final fail-

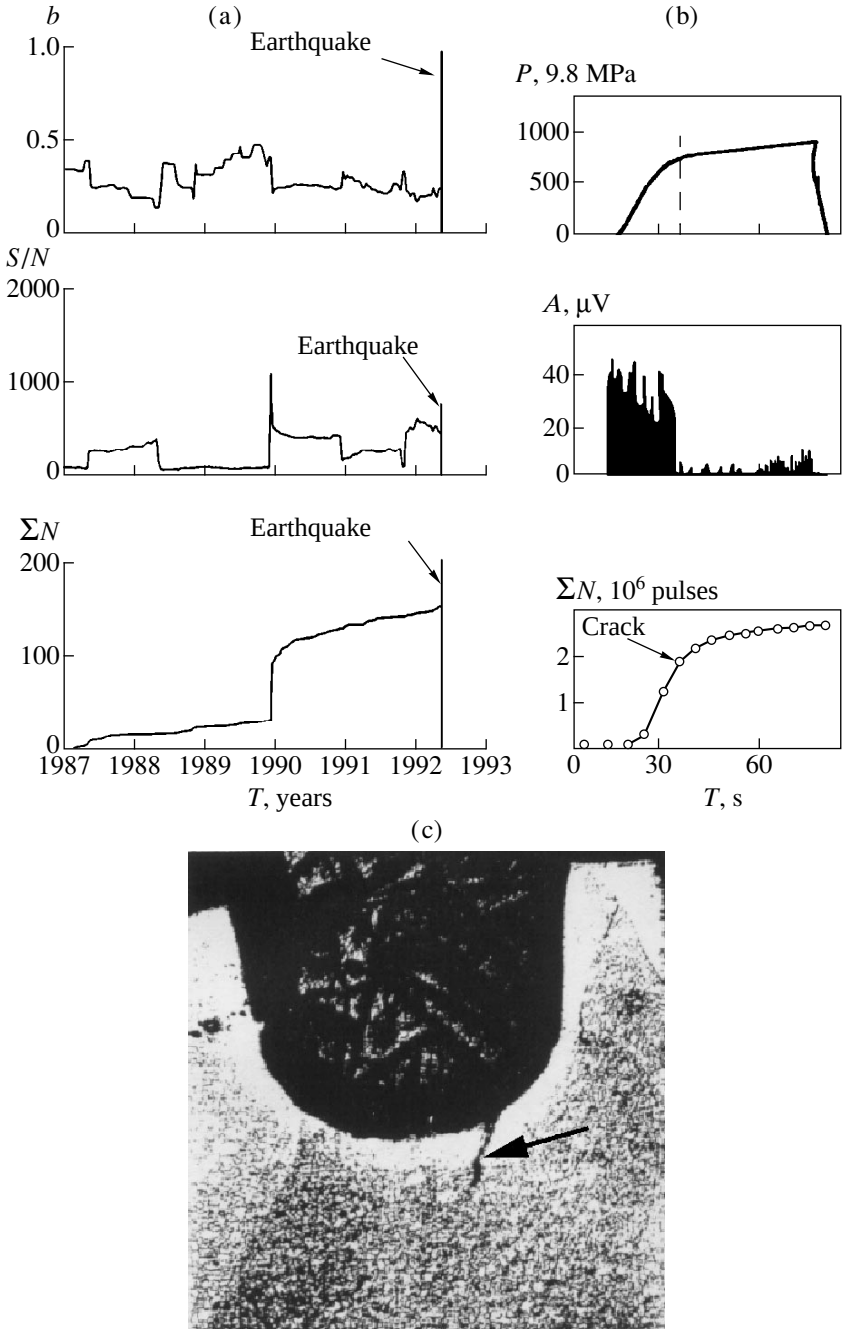

Fig. 1. Temporal dependences of the accumulated number of (a) seismic events prior to the Philippines earthquake on May 17, 1992, with $M = 7.5$ (latitude is 17.19°, longitude is 126.76°, depth is 33 km) and (b) acoustic events while destroying specimens made of 17KhG2SAFR steel with a notch radius $r = 1.5$ mm. (c) The initial crack in the notch mouth for a 17KhG2SAFR girder-steel specimen tested for three-point bending.

ure. In a number of cases, this resulted in one more plateau in the curve $\Sigma N(T)$. This fact made it possible to relate the development of the unstable brittle crack to a short-term lull. This is in contrast to the concept of a stable crack development initiating an intermediate-type lull.

As the estimates [11] have shown for specimen fractures (see Table 2), it is the stable-crack length l_c that determines the lull-period T_{AE}, since in the case of a larger stable-crack length, a longer lull duration is observed. It follows from Table 2 that the duration of the lull period for a specimen depends on the steel strength and viscosity and on the notch radius r. The lower the strength of a material and the weaker the tendency to brittle fracture, the longer the period in the acoustic-activity decrease and, correspondingly, the

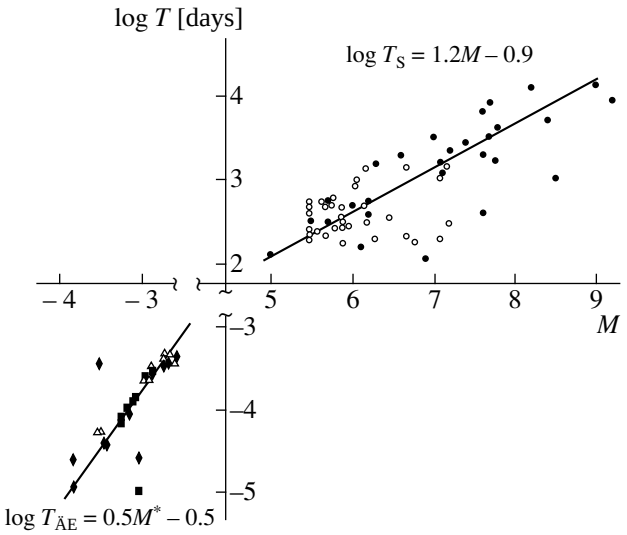

Fig. 2. The duration of the period of seismic T_S and acoustic T_{AE} lull (the first and third quadrants, respectively) as functions of the magnitudes of earthquakes (M) and metallic-specimen failures (M*). ● Data of T. Rikitake [5]; ○ data obtained in the present study for the earthquakes in North California; ■ steel 45; △ steel U8; ◆ steel 17KhG2SAFR.

period of stable crack growth (occurring, in this case, with a low speed). The same effect is caused by an increase in the specimen notch radius and a decrease in the loading rate.

The effect of the factors indicated is also found in evaluating the maximum number N_{max} of accumulated events. While testing viscous steels, N_{max} increases with the notch radius. However, while testing higher-strength steels, N_{max} is scarcely affected by variation of the notch radius.

Thus, the phenomenon of acoustic lull is associated with a stable development of a crack formed at the beginning of the lull period. The duration of this period is determined by a strained state near the crack vertex. This state depends on the notch-vertex radius and the strength and viscosity of the specimen material. According to fracture-mechanics approaches, this state can be characterized by the stress-intensity coefficient. When, for a given material, the critical value for this coefficient is attained, the lull period is over and unstable brittle fracture begins.

In a similar manner, a lull period can be characterized by the work spent for the crack-development or by the total work E spent for the specimen fracture. This work is numerically equal to the area under the deformation curve. Then, from the relation used in seismology between the earthquake energy and magnitude, we can estimate a new parameter characterizing the metallic-specimen fracture, i.e., the fracture magnitude M*. This allows us to compare the magnitude dependences for the duration of the seismic lull period T_S prior to an earthquake and the acoustic period T_{AE} prior to the specimen fracture.

The values of the fracture magnitudes M* calculated from the well-known Gutenberg–Richter relation

$$1.5M = 11.8 - \log E \text{ [erg]}$$

are listed in Table 2. In the third quadrant of Fig. 2 are shown the magnitude dependences obtained for the duration of the acoustic-lull periods T_{AE} prior to fractures of specimens with various strength, viscosity, and

Table 2. Failure characteristics for metal specimens [11] and corresponding estimated failure magnitudes

Steel quality and mechanical properties	r, mm	T_{AE}, s	E, J	M*	l_c, mm	ΣN, 10^5 pulses
Steel 45, σ_b > 610 MPa, $\sigma_{0.2}$ = 360 MPa	1.5	46	37.8	–3.3	1.1	2.3
	1.0	45	37.2	–3.3	1.61	3
	0.5	27	21.7	–3.5	1.13	3
	0.1	25	17.1	–3.5	0.5	3
	<0.1	11	7.0	–3.9	0.18	2
Steel 17KhG2SAFR, σ_b = 860 MPa, $\sigma_{0.2}$ = 630 MPa	1.5	59	66.5	–3.2	0.94	17
	1.0	63	76.0	–3.1	0.80	–
	0.5	41	37.3	–3.3	0.70	5.3
	0.1	22	22.9	–3.6	0.22	7
	<0.1	14	9.3	–3.8	0.07	4
Steel U8, σ_b = 1000 MPa	1.5	66	55.5	–3.1	0.70	0.7
	1.0	65	56.1	–3.1	0.72	–
	0.5	43	34.2	–3.3	0.39	0.9
	0.1	17	7.8	–3.7	0.12	2.1

notch shapes. It is seen that, for three types of steels, the experimental points satisfy the universal straight line described by the relation

$$\log T_{AE} = 0.5M^* - 0.5.$$

The points not satisfying this dependence and positioned below and above it correspond to specimens with sharp notches (with radii near the vertex $r \le 0.1$) that initiate brittle fracture of the specimens, which is followed by an elevated spread of mechanical properties.

In the first quadrant of Fig. 2 is shown the magnitude dependence of the seismic-lull-period duration T_S described by the relation $\log T_S = 1.2M - 0.9$ and constructed according to data obtained both in the present study and published in [6]. According to the data of other authors, who analyzed the lull phenomenon in various regions of the world, the coefficient standing at the magnitude M ranges from 0.3 to 0.8.

Both magnitude relationships shown in Fig. 2 are linear in the coordinates used but differ in the level of estimated parameters (T and M) and in their slope.

The results of this study allow us to suggest that seismic lull periods of the intermediate type, by analogy with acoustic periods, are associated with localization of the fracture in the Earth's crust, reduction of the prefracture zone, and formation of the principal fracture and its subsequent stable development. The duration for both lull-period types is controlled by the stressed state in the mouth of the principal fracture. This state depends on the rock strength, viscosity, degree of comminution, and the strain rate, as well as on the geometry of the fracture vertex.

ACKNOWLEDGMENTS

This work was supported in part by the Russian Foundation for Basic Research, projects no. 0001-00160 and 0015-99073.

REFERENCES

1. V. I. Keĭlis-Borok and L. N. Malinovskaya, J. Geophys. Res. **69**, 3019 (1964).
2. K. Mogi, *Earthquake Prediction* (Academic, Orlando, 1985; Nauka, Moscow, 1988).
3. M. Wyss and R. E. Habermann, PAGEOPH **126** (2/4), 319 (1998).
4. V. G. Kosobokov, V. I. Keĭlis-Borok, and S. W. Smith, J. Geophys. Res. B **95**, 19763 (1990).
5. T. Rikitake, Bull. Seismol. Soc. Am. **65**, 1133 (1975).
6. H. Kanamori, in *Earthquake Prediction: An International Review*, Ed. by D. W. Simpson and P. G. Richards (American Geophysical Union, Washington, DC, 1981), Maurice Ewing Series, Vol. 4, p. 1.
7. J. Weeks, D. Lockner, and J. Byerlee, Bull. Seismol. Soc. Am. **68**, 333 (1978).
8. A. V. Ponomarev, A. D. Zavyalov, and D. A. Lockner, Tectonophysics **277**, 57 (1997).
9. W. D. Smith, Nature **289**, 333 (1981).
10. L. R. Botvina, I. S. Guz', V. S. Ivanova, *et al.*, in *Proceedings of the IX All-Union Acoustical Conference, Moscow, 1977*, p. 183.
11. V. A. Kobzev, Candidate's Dissertation in Technical Science (IMET Akad. Nauk SSSR, Moscow, 1978).

Translated by V. Tsarev

Doklady Physics, Vol. 46, No. 2, 2001, pp. 124–127. Translated from Doklady Akademii Nauk, Vol. 376, No. 4, 2001, pp. 485–487.

MECHANICS

A Direct Impedance Method for Calculation of Wave Fields in Stratified-Homogeneous Media

V. N. Krutin

Presented by Academician V.P. Myasnikov July 10, 2000

Received July 13, 2000

When calculating elastic wave fields in stratified-homogeneous media, two approaches are usually used. These are the matrix Thomson–Hackell method [1, 2] developed in [3] and the impedance method proposed in [4, 5] and developed in [6].

According to the first method, each layer is represented by a characteristic matrix linking the spectra of stress vectors and displacement vectors at the boundaries of this layer (see below). The layered system, as a whole, is described by a matrix obtained by multiplying (in a certain order) the characteristic matrices of the layers. At given boundary value conditions, this matrix and the inverse one define the wave field.

The impedance method employs the linear dependence of the stress spectra and displacement spectra with the impedance tensor at an arbitrary coordinate along the gradient of the medium properties or at the layer boundaries. The determination of this tensor is reduced to solving the Cauchy problem for the matrix ordinary differential Riccati equation followed by subsequent determination of the field.

Both methods are valid for stratified and gradient media and possess mutual advantages and disadvantages.

In this study, we propose a new method, which is, in a certain sense, a hybrid one. In addition, it is rather simple and calls for a smaller amount of computation. To illustrate the essence of the method, we consider, as an example, a radially inhomogeneous medium in cylindrical coordinates r, θ, $z(x_1, x_2, x_3)$.

The method is based on solving the following problem. Let an mth cylindrical coaxial layer (r_{m-1}, r_m) be given. The layer is occupied by a homogeneous isotropic viscoelastic medium with complex elastic frequency-dependent Lamé moduli $\tilde{\lambda}_m$ and $\tilde{\mu}_m$ [7] and density ρ_m. One of the layer boundaries is loaded by a known impedance (for definition, see below). It is necessary to find the impedance at the other boundary.

The equation of small-amplitude harmonic vibrations varying by the law $\exp(-i\omega t)$ in a viscoelastic medium has the form [8]

$$(k_p^{-2}\text{grad}\cdot\text{div} - k_s^{-2}\text{rot}\cdot\text{rot} + I)\cdot\mathbf{u} = 0, \qquad (1)$$

where I is the identity matrix; $\mathbf{u}$ is the displacement vector; $k_p = \dfrac{\omega}{c_p}$ and $k_s = \dfrac{\omega}{c_s}$ are the complex wave numbers for longitudinal and transverse waves, respectively; and $c_p = \sqrt{\dfrac{\tilde{\lambda} + 2\tilde{\mu}}{\rho}}$ and $c_s = \sqrt{\dfrac{\tilde{\mu}}{\rho}}$ are the complex propagation velocities of these waves, respectively.

By definition, we introduce the potentials

$$\mathbf{u} = \nabla\varphi + \nabla\times(\psi\cdot\mathbf{e}_z) + R\cdot\nabla\times\nabla\times(\chi\cdot\mathbf{e}_z), \qquad (2)$$

where $\mathbf{e}_z$ is the unit vector and R is the arbitrary reduction radius.

Equations (1) are satisfied by the solutions to the following Helmholtz equations [9]:

$$\begin{gathered}(\Delta + \Lambda^2)\varphi = 0, \quad (\Delta + \tau^2)\psi = 0,\\ (\Delta + \tau^2)\chi = 0,\end{gathered} \qquad (3)$$

where Δ is the Laplacian, $\Lambda = k_pR$, and $\tau = k_sR$. Henceforth, we use the dimensionless coordinates $\bar{r} = \dfrac{r}{R}$, $\bar{z} = \dfrac{z}{R}$.

For a layer, the solutions to Eqs. (3) have the form

$$\begin{aligned}(\bar{\varphi}, \bar{\psi}, \bar{\chi}) &= \frac{1}{R^2}(\varphi, \psi, \chi)\\ &= \frac{1}{2\pi}\sum_{n=-\infty}^{\infty} e^{in\theta}\int_{-\infty}^{\infty}(\varphi_n, \psi_n, \chi_n)e^{i\zeta\bar{z}}d\zeta,\end{aligned} \qquad (4)$$

All-Russia Scientific and Research Institute of Geological, Geophysical, and Geochemical Systems, Russian Academy of Sciences, Moscow

1028-3358/01/4602-0124$21.00

where

$$\varphi_n = A_{1n}H_n^{(1)}(p\bar{r}) + A_{2n}H_n^{(2)}(p\bar{r}),$$
$$\psi_n = A_{3n}H_n^{(1)}(s\bar{r}) + A_{4n}H_n^{(2)}(s\bar{r}), \quad (5)$$
$$\chi_n = A_{5n}H_n^{(1)}(s\bar{r}) + A_{6n}H_n^{(2)}(s\bar{r}).$$

Here, $H_n^{(1,2)}(x)$ are the nth-order Hankel functions of the first and second kind of the argument x, respectively; $p = \sqrt{\Lambda^2 - \zeta^2}$ and $s = \sqrt{\tau^2 - \zeta^2}$.

With respect to angular harmonics, the solutions are completely split. Therefore, we consider furthermore only the spatial spectrum with respect to z of the nth harmonic. Below, we do not indicate this fact and use, for example, A_k instead of A_{kn}.

At an arbitrary cylindrical boundary, the spectra of stresses $\boldsymbol{\sigma}$ and displacements $\mathbf{u}$ are linked by the linear dependence

$$\sigma_i = \sigma_{ij}n_j = -G_{ij}u_j = -Z_{ij}v_j, \quad i, j = 1, 2, 3, \quad (6)$$

where G_{ij} and Z_{ij} are the complex tensors of spatial spectral elasticity and spatial spectral impedance, respectively; $v_j = -i\omega u_j$ are vibration-velocity components; and $\mathbf{n}$ is the unit vector of the outer normal to the surface. In addition, $Z_{ij} = -Z_{ji}$, $i \neq j$ [6].

It is evident that $G_{ij} = -i\omega Z_{ij}$. Therefore, at small vibrations, the use of G_{ij} and Z_{ij} is equivalent. By convention, we term the method the "impedance elasticity" and the tensor G_{ij} the "loading elasticity," which emphasizes the extraneous interaction of the media separated by the boundary.

On the surface r = const, the stresses are determined by the formula [8]

$$\boldsymbol{\sigma}(r) = \tilde{\lambda}\mathbf{n}\cdot\mathrm{div}\mathbf{u} + 2\tilde{\mu}\left(\frac{\partial\mathbf{u}}{\partial n}\right) + \tilde{\mu}[\mathbf{n}\times\nabla\times\mathbf{u}], \quad (7)$$
$$\mathbf{n} = \mathbf{e}_r.$$

Introducing an arbitrary constant normalizing elasticity μ_0 and taking into account (2) and (6), we obtain for the spectra

$$\bar{\sigma}_i = \frac{\sigma_i}{\mu_0} = -g_{ij}^m\bar{u}_j + b_{ik}^m A_k,$$
$$(\bar{G}_{ij} - g_{ij}^m)\bar{u}_j + b_{ik}^m A_k = 0, \quad (8)$$

where

$$\bar{u}_j = \frac{u_j}{R}, \quad \bar{G}_{ij} = \frac{G_{ij}}{\mu_0}, \quad \bar{\mu}_m = \frac{\tilde{\mu}_m}{\mu_0},$$

$$g_{ij}^m = 2\bar{\mu}_m g_{ij}, \quad g_{11} = g_{22} = \frac{1}{\bar{r}}, \quad g_{12} = \frac{in}{\bar{r}}, \quad g_{13} = i\zeta,$$
$$g_{ij} = -g_{ji} \ (i \neq j), \quad g_{23} = g_{33} = 0,$$
$$b_{ik}^m = \bar{\mu}_m b_{ik}, \quad b_{11} = -\tau^2 H_n^{(1)}(p\bar{r}),$$
$$b_{23} = s^2 H_n^{(1)}(s\bar{r}), \quad (9)$$
$$b_{33} = \frac{n\zeta}{\bar{r}}H_n^{(1)}(s\bar{r}), \quad b_{35} = \tau^2 s\hat{H}_n^{(1)}(s\bar{r}),$$
$$b_{13} = b_{15} = b_{21} = b_{25} = b_{31} = 0,$$
$$b_{i,2k} = b_{i,(2k-1)}^{(2)}.$$

Here, the formulas of the type $b_{12} = b_{11}^{(2)}$ imply that b_{12} is obtained from b_{11} as a result of changing the Hankel function of the first kind to that of the second kind; the sign $\wedge$ denotes the differentiation with respect to the argument; in (8), the summation over j and k is taken from 1 to 3 and from 1 to 6, respectively.

From (2), we have

$$\bar{u}_j = a_{jk}A_k, \quad (10)$$

$$a_{11} = p\hat{H}_n^{(1)}(p\bar{r}), \quad a_{13} = \frac{in}{\bar{r}}H_n^{(1)}(s\bar{r}),$$
$$a_{15} = i\zeta s\hat{H}_n^{(1)}(s\bar{r}),$$
$$a_{21} = \frac{in}{\bar{r}}H_n^{(1)}(p\bar{r}), \quad a_{23} = -s\hat{H}_n^{(1)}(s\bar{r}), \quad (11)$$
$$a_{25} = -\frac{n\zeta}{\bar{r}}H_n^{(1)}(s\bar{r}),$$
$$a_{31} = i\zeta H_n^{(1)}(p\bar{r}), \quad a_{33} = 0,$$
$$a_{35} = s^2 H_n^{(1)}(s\bar{r}), \quad a_{j,2k} = a_{j,(2k-1)}^{(2)}.$$

Then, (8) takes the form

$$[(\bar{G}_{ij} - g_{ij}^m)a_{jk} + b_{ik}^m]A_k = d_{ik}A_k = 0. \quad (12)$$

Let the loading elasticity of the mth layer at the boundary $\bar{r} = \bar{r}_m$ be known and equal to $\bar{G}_{ij}(\bar{r}_m)$. Then, from (12), we obtain three equations:

$$d_{ik}(\bar{r}_m)A_k = 0. \quad (13)$$

At the second boundary, $\bar{r} = \bar{r}_{m-1}$, of the layer, we use in addition three equations (10):

$$a_{jk}(\bar{r}_{m-1})A_k = \bar{u}_j(\bar{r}_{m-1}). \quad (14)$$

From the system of equations (13) and (14), we can determine the six-dimensional vector $\mathbf{A}^m$, expressing its components A_k in terms of $u_j(\bar{r}_{m-1})$ and $\overline{G}_{ij}(\bar{r}_m)$. The determinant of this system is nonzero. Inverting the system, we have

$$A_k = q_{kj}\bar{u}_j(\bar{r}_{m-1}). \quad (15)$$

From (8), at $\bar{r} = \bar{r}_{m-1}$, we obtain expressions for the desired components of the loading-elasticity tensor:

$$\overline{G}_{ij}(\bar{r}_{m-1}) = g^m_{ij}(\bar{r}_{m-1}) - b^m_{ik}(\bar{r}_{m-1})q_{kj}. \quad (16)$$

These expressions are the solutions to the problem under consideration for the cylindrical coaxial layer. It is evident that result (16) retains its validity if we mutually interchange everywhere $\bar{r}_m$ and $\bar{r}_{m-1}$.

Let the outer boundary $\bar{r} = \bar{r}_N$ of the layer be in contact with an infinite viscoelastic medium. We now determine its impedance for arbitrary vibrations at the boundary $\bar{r} = \bar{r}_N$.

From the radiation conditions, it follows that in (5), $A_2 = A_4 = A_6 = 0$. Thus, in (9), only the Hankel functions of the first kind remain. Further, we introduce the 3×3 matrices β_{ik} and α_{jk} with their components $\beta_{ik} = b_{i,(2k-1)}$ and $\alpha_{jk} = a_{j,(2k-1)}$, where b_{ik} and a_{jk} are determined by formulas (9) and (11). System (10) takes the form

$$\alpha_{jk}(\bar{r}_N)A_k = \bar{u}_j(\bar{r}_N) \quad (17)$$

and is closed. Whence it follows that

$$A_k = q_{kj}(\bar{r}_N)\bar{u}_j(\bar{r}_N) \quad (\|q_{kj}\| = \|\alpha_{jk}\|^{-1}). \quad (18)$$

Substituting A_k into (8), we obtain the expression for the loading elasticity:

$$\overline{G}_{ij}(\bar{r}_N) = g^{N+1}_{ij}(\bar{r}_N) - \beta^{N+1}_{ik}(\bar{r}_N)q_{kj}(\bar{r}_N). \quad (19)$$

We do not write out the explicit formulas for a viscoelastic medium and an ideal liquid here.

If there is a stratified system with piecewise-constant functions $\tilde{\lambda}(\bar{r})$, $\tilde{\mu}(\bar{r})$, and $\rho(\bar{r})$, then calculations are performed sequentially for each layer by the same algorithm considered above. In this case, only the values of the material parameters and the numbers of the boundaries are changed, with allowance for the continuity condition with respect to all impedance components. This condition follows from the continuity of stresses and displacements at all boundaries. The gradient medium is approximated, as in the matrix method, by a number of thin homogenous layers with a corresponding partition step. As a result, we find the impedance at one system boundary provided that it is known at the other boundary.

The initial boundary $(\bar{r}_0, \bar{r}_N)$ of the stratified-homogeneous system may be loaded by the known impedance, for example, by the infinite-medium impedance (19). This boundary may be free of stresses (zeroth impedance) or fixed (zeroth admittance). As $\bar{r}_0 \longrightarrow 0$, singularities are eliminated by the method described in [10]. Let the stresses (displacements) determined by a source at $\bar{r} = \bar{r}_0 \neq 0$ be known. Using (6), we derive the displacements (stresses) as

$$\bar{u}_j(\bar{r}_0) = -\|\overline{G}_{ij}\|^{-1}\bar{\sigma}_i(\bar{r}_0), \quad \bar{\sigma}_i(\bar{r}_0) = -\overline{G}_{ij}(\bar{r}_0)\bar{u}_j(\bar{r}_0), \quad (20)$$

provided that the impedance is known as a result of calculations.

Knowledge of the three-dimensional displacement vectors and stress vectors for $\bar{r} = \bar{r}_0$ makes it possible to determine the six-dimensional vector $\mathbf{A}$ in the adjoining layer and, then, in the entire system, which determines the wave field.

If the source is placed inside the domain, then, recalculating the impedance at both edges, we arrive at the problem of a uniform (maybe, thin) layer loaded at its boundaries by known impedances, with the source being placed inside the layer or at its boundary. This problem has a unique solution. Knowledge of the impedance at the boundary and the vibrations at this boundary is sufficient for determining $\mathbf{A}$ in the adjoining layers and, consequently, the field in the entire system.

The characteristics of the normal waves and other wave modes in the system are determined in the same way as in calculating the impedance.

The method described can be applied, at least, in five coordinate systems in which the longitudinal and transverse waves are separated [9]. It may be used for solving the problems of borehole acoustics, seismic surveying, and in the analysis of natural vibrations of planets. The method may be extended to the problems of electrodynamics and optics (fiber optics, spherically nonuniform lenses, etc.). Since recalculation of the impedance is similarly performed while decreasing and increasing $\bar{r}$, it is possible to test the calculations for finding calculation errors and to construct refining interpolation formulas.

REFERENCES

1. W. T. Thomson, J. Appl. Phys. **21**, 89 (1950).
2. N. A. Hackell, Bull. Seismol. Soc. Am. **43**, 17 (1953).
3. L. A. Molotkov, in *Mathematical Problems in the Theory of Wave Propagation* (Leningrad, 1972), Vol. 4, p. 116.

4. M. M. Machevariani, V. V. Tyutekin, and A. P. Shkvarnikov, Akust. Zh. **17**, 97 (1971) [Sov. Phys. Acoust. **17**, 77 (1971)].
5. P. E. Krasnushkin, Dokl. Akad. Nauk SSSR **252**, 332 (1980) [Sov. Phys. Dokl. **25**, 358 (1980)].
6. A. V. Bezrukov, V. Yu. Prikhod'ko, and V. E. Tyutekin, Akust. Zh. **32**, 372 (1986) [Sov. Phys. Acoust. **32**, 227 (1986)].
7. V. N. Krutin, *Vibrational Rheometers* (Mashinostroenie, Moscow, 1985).
8. L. D. Landau and E. M. Lifshitz, *Course of Theoretical Physics*, Vol. 7: *Theory of Elasticity* (Nauka, Moscow, 1987; Pergamon, New York, 1986).
9. P. M. Morse and H. Feshbach, *Methods of Theoretical Physics* (McGraw-Hill, New York, 1953; Inostrannaya Literatura, Moscow, 1960), Vol. 2.
10. V. V. Muzychenko, *Sound Diffraction on Elastic Shells* (Nauka, Moscow, 1993).
11. G. I. Petrashen', L. A. Molotkov, and P. V. Krauklis, *Waves in Layered-Homogeneous Isotropic Elastic Media* (Nauka, Leningrad, 1985), Vol. 2.

Translated by Yu. Vishnyakov

Doklady Physics, Vol. 46, No. 2, 2001, pp. 128–131. Translated from Doklady Akademii Nauk, Vol. 376, No. 4, 2001, pp. 488–491.

MECHANICS

The Dissipative Function in Models of Perfect Elastoplastic Bodies

Academician E. I. Shemyakin

Received October 24, 2000

1. In recent papers [1–5], mathematical models for perfect plastic bodies were widely discussed. The new results presented in them are associated with the development of the ideas of T. Kármán, which concern complete- and incomplete-plasticity states and plasticity singular conditions of the Tresca–Saint-Venant type [1, 3, 4, 6]. In this case, representation of the dissipative function determining the energy loss caused by irreversible (plastic) shear deformation is of primary importance. Indeed, the energy loss due to volume deformations is not considered at this level (the effects of packing change and dilatancy are ignored) and, consequently, the concept of the dissipative function reflects fundamental mechanical hypotheses lying in the basis of the mathematical model.

Usually, when constructing an expression for the dissipative function, we automatically (or by analogy with a perfectly elastic body) assume that the principal directions for the stress tensor and strain (strain rate) tensor also coincide with each other in the plastic state. As a result, the expression for the dissipative function D takes the form

$$\Delta D = \sigma_i \Delta \varepsilon_i^p, \tag{1}$$

where σ_i are the principal stresses and $\Delta\varepsilon_i^p$ are the increments of the plastic strain at each step of loading. In correspondence with the invariants introduced previously for stressed and strained states [3, 4], we consider sets of the invariants

$$T, \mu_\sigma, \sigma_n; \Gamma, \mu_\varepsilon, \varepsilon_n. \tag{2}$$

Here, T and Γ are the maximum tangential stress and the principal shear in the principal cross section; σ_n is the normal stress in the same cross section; ε_n is the strain normal to the cross section of the principal shear; and μ_σ and μ_ε are the Nádai–Lode factors for the corresponding states. For these sets of the invariants, a specific connection with the trihedron (trihedrons) of the principal directions is characteristic, although the quantities σ_n and ε_n represent spherical tensors. The parameters μ_σ and μ_ε are rather important in this discussion. Their equality implies the similarity of the corresponding tensors:

$$\mu_\sigma = \mu_\varepsilon, \quad \mu_\sigma = \mu_{\Delta\varepsilon} \tag{3}$$

(in connection with the proposed set of the invariants, see the data of Taylor and Quinney presented in [3, 4]).

In our opinion, the role of the parameters μ_σ and μ_ε is beyond the scope of mathematical formulation of the similarity problem, because they contain substantial information on the role played by other areas with extreme values of tangential stresses and strains in the Mohr stress circles:

$$\mu_\sigma = \frac{T_{23} - T_{12}}{T}, \tag{4}$$

$$T_{12} = \frac{\sigma_1 - \sigma_2}{2}, \quad T_{23} = \frac{\sigma_2 - \sigma_3}{2}. \tag{5}$$

It is worth noting that the hypothesis of the similarity of tensors, which is used while constructing mathematical models in continuum mechanics (including the model of a viscous non-Newtonian fluid), represents a very strong requirement. It implies not only proportionality of tensor components (deviators) but also coincidence of the principal directions. From this standpoint, it is important when following Kármán [6, 7], to separate two requirements, namely, those of the proportionality of the tensor components and the coincidence of the principal axes, especially in connection with the states of complete and incomplete plasticity.

We consider the incomplete-plasticity state in the case of immobile (with respect to the initial elastic state) principal directions. Then, according to Kármán, this implies that the maximum tangential stress T attains the Tresca–Saint-Venant limiting value $T = \tau_S$ corresponding to the given material, whereas two other extreme tangential stresses remain below this limit. For this state, there exist two deformation features associated with the transition to complete plasticity, in which two of the three extreme tangential stresses attain limiting values and remain constant during the deformation process. The first feature is associated with the fact

Moscow State University,
Vorob'evy gory, Moscow, 119899 Russia

1028-3358/01/4602-0128$21.00

that elastic bonds are conserved in the second principal direction; i.e., the body becomes anisotropic with respect to shears (at least, orthotropic). The second feature is associated with investigation of area fans in the vicinity of principal-shear areas. The constant value of T is attained in the basic area and the principal shear Γ grows (i.e., plastic deformation occurs). At the same time, in the vicinity of the area bisecting the angles between the first and the third principal axes and passing through the second principal axis, i.e., in other areas passing through the second axis, the tangential stresses are lower than their ultimate value. Shears occurring in these areas are in no way related to their own tangential stresses, so that the anisotropy of resistance to shear (orthotropy with allowance for orthogonality of the trihedron of the principal directions) again manifests itself. These features of the plastic state are of great importance, especially in the case of rotation of the principal directions of the stressed and strained states [8].

Thus, in the transition to the plastic state, a material can acquire anisotropic features with respect to the resistance to shears even if, initially, it was homogeneous and isotropic. As the residual strain, the anisotropy induced by plastic deformations likely represents a basic property of solids. A similar remark is possibly also valid in the case of constructing mathematical models for viscous non-Newtonian media.

2. We now consider the transition from incomplete plasticity to complete plasticity, which occurs with the conservation of the principal directions of the stressed and strained states. Then, in the general relation between the invariants

$$G(T, \mu_\sigma, \sigma_n) = 0, \tag{6}$$

where G is the function determined experimentally (see, e.g., [4]), the onset of the complete plasticity state depends on the form of the stressed state μ_σ only in other extreme areas in addition to the principal one. At the same time, the spherical tensor σ_n only causes volume strain, without affecting the process of plastic deformation. We can consider a surface mapping the process of loading and deformation in the space of the invariants T, μ_σ, and σ_n (see figure). The point A and those inside the rectangular parallelepiped represent the initial incomplete-plasticity state and elastic states, respectively. In the case of stress variation, the motion of the point A in the plane $T = \tau_S = \text{const}$ corresponds to the elastic deformations in the second principal direction. When the point A approaches the face $\mu_\sigma = -1$, the limiting value is attained in the area with the stress T_{12}; i.e., the complete-plasticity state arises:

$$\sigma_1 - \sigma_3 = 2\tau_S, \quad \sigma_1 - \sigma_2 = 2\tau_S. \tag{7}$$

Consequently, as A tends to the face $\mu_\sigma = -1$, the stress T_{12} grows and T_{23} drops. At the same time, as A approaches the face $\mu_\sigma = 1$, the tangential stress T_{23} increases and T_{12} decreases. It should be emphasized that in the incomplete-plasticity state, by virtue of the conservation of elastic bonding in the second principal direction, a decrease in T_{12} or T_{23} does not imply unloading in the areas where it occurs. The scheme of loading and deformation of the perfect elastoplastic bodies under consideration may form a basis for the classification of loading types. For example, in a broad sense [6], the simple loading corresponds to the motion of the point A along the face $T = \text{const}$ within the range $1 \geq \mu_\sigma \geq -1$, but without attaining extreme values. As has been noted before, the motion of this point towards the interior of the volume corresponds to unloading.

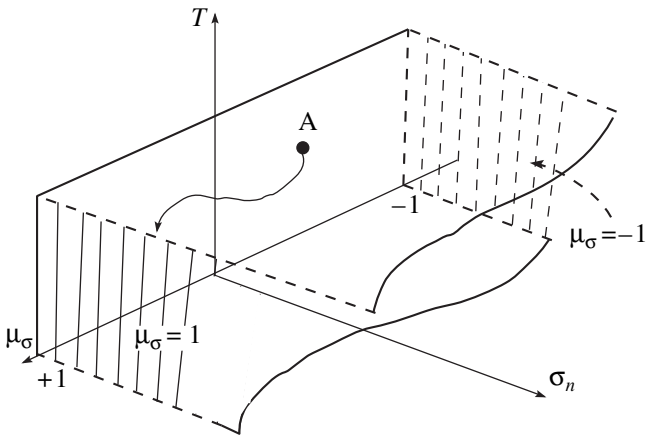

Figure.

The simple loading is also the load applied to the edges $\mu_\sigma = \pm 1$, provided that the transition to the complete-plasticity state occurs immediately from the elastic state. However, in this case, in addition to the elastic unloading, there is also a partial unloading. This occurs when the point A is displaced onto one of the faces situated to the left or to the right of the edge. For example, the transition onto the face $\mu_\sigma = 1$ implies unloading in the area with stress T. In this case, the increments of T and Γ are related by the law of elasticity:

$$\Delta T = \mu \Delta \Gamma. \tag{8}$$

Completing a rough classification of loading types, we call the loading that accompanied the rotation of the principal directions complex. In these cases, as has been noted above, a dissimilarity of the tensor principal axes arises, so that the maximum tangential stresses and the principal shears act in different, not coinciding, areas. Examples of complex loading corresponding to this classification are presented in [8].

3. Returning to the structure of the dissipative function, we note certain features of the plasticity condition (6) which are characteristic for a transition from the incomplete-plasticity state to the complete-plasticity state. Since $T = \text{const}$ and σ_n does not affect plastic deformation, we have from (6)

$$G(\bar{\mu}_\sigma) = 0, \quad \bar{\mu}_\sigma = \frac{2\sigma_2 - \sigma_1 - \sigma_3}{2\tau_S}. \tag{9}$$

As was said above, the edges $\mu_\sigma = 1$ or $\mu_\sigma = -1$ represent the lines of the transition to the complete-plasticity state. Consequently, the condition for the transition to the complete-plasticity state has the form

$$\mu_\sigma \mp 1 = 0. \quad (10)$$

Concerning calculations of shears, we note that their values in the extreme areas are governed by the parameter μ_ε, while the quantity Γ in itself is not related to the stressed state; it depends on the problem geometry, i.e., on the slip-line network and the problem boundary conditions, including elastic zones, the network being determined by the conditions at the boundary with the elastic zone.

Finally, we express the dissipative function in new invariants, bearing in mind that

$$\sigma_1 = T + \sigma_n, \quad \sigma_2 = \sigma_n + \mu_\sigma T, \quad \sigma_3 = -T + \sigma_n. \quad (11)$$

Thus, we obtain

$$\sigma_i \Delta\varepsilon_i^p = T\Delta\Gamma^p + \mu_\sigma T\Delta\varepsilon_2^p = T\Delta\Gamma^p\left(1 + \mu_\sigma\frac{\mu_{\Delta\varepsilon}}{3}\right). \quad (12)$$

The expression for D does not contain μ_ε, but involves $\mu_{\Delta\varepsilon}$. We note the following:

(i) The quantity $\Delta\varepsilon_2^p$ does not enter into D only at $\mu_\sigma = 0$ (pure shear). For other values of $\mu_\sigma \neq 0$, the quantity $\Delta\varepsilon_2^p$ can affect the dissipation. This is explained by the fact that, due to the incompressibility of the medium, $\Delta\varepsilon_2^p$ can be directly expressed in terms of $\mu_{\Delta\varepsilon}$ and $\Delta\Gamma^p$; i.e.,

$$\mu_{\Delta\varepsilon} = \frac{3\Delta\varepsilon_2^p}{\Delta\Gamma^p}. \quad (13)$$

(ii) In the complete-plasticity state, ($\mu_\sigma = \pm 1$),

$$\Delta D = T(\Delta\varepsilon_1^p - \Delta\varepsilon_3^p + \mu_\sigma\Delta\varepsilon_2^p),$$

so that, in these cases, the quantity $\Delta\varepsilon_2^p$ affects the total dissipation and, after the second direction has become valid, controls the quantity μ_σ.

By virtue of the linear dependence of $D(\mu_\sigma)$, there is no necessity for D to be optimized. Independently of the sign of μ_σ, the optimum value of D can be calculated as

$$\Delta D = \frac{4}{3}T\Delta\Gamma^p.$$

The above-mentioned experiments of Taylor and Quinney [3, 4] show that, in the complete-plasticity state, the similarity of tensors, which is violated in the case of the incomplete-plasticity state, can be restored. This implies that the energy dissipation in the case of plastic deformation is controlled by the parameter $\mu_{\Delta\varepsilon}$.

In turn, this implies that at $\mu_\sigma = 1$, the increments (but not the shears in themselves) are equal to one another:

$$\Delta\Gamma_{23}^p = \Delta\Gamma^p.$$

If $\mu_\sigma = -1$, then, respectively, $\Delta\Gamma_{12}^p = \Delta\Gamma^p$.

The positiveness of D allows both the theorem of uniqueness of the solutions to the boundary value problems for elastoplastic bodies and variational principles to be considered. In this connection, a theorem for the body's energy can be written out as

$$\int_S \boldsymbol{\sigma}_\nu \cdot \mathbf{u}\,d\mathbf{S} + \int_V \mathbf{F}\cdot\mathbf{u}\,dV = 2\int_V W\,dV + \int_V D\,dV, \quad (14)$$

where W is the positive-definite quadratic form with respect to stresses or strains for elastic states, while D is positive for all $\mu_{\Delta\varepsilon}$ and $\Delta\Gamma^p$. In calculating D, the condition of the complete-plasticity state is taken into account.

Systems of partial differential equations for the states of complete and incomplete plasticity can be indicated; these are similar to the Lamé system in the elasticity theory. This is rather convenient in discussing transitions from one state into another. The equations are derived in the local coordinate system x, y, z under the assumption that the principal directions of stressed and strained states coincide with each other and the volume variation is elastic (see [1]).

In the case of incomplete plasticity, the system has the form

$$\begin{aligned}
&(\lambda+\mu)\frac{\partial^2 u}{\partial x^2} + C_2\frac{\partial^2 u}{\partial y^2} + C_1\frac{\partial^2 u}{\partial z^2} \\
&+ (\lambda + C_2)\frac{\partial^2 v}{\partial x\partial y} + (\lambda+\mu+C_1)\frac{\partial^2 w}{\partial x\partial z} = 0, \\
&(\lambda + C_2)\frac{\partial^2 u}{\partial x\partial y} + C_2\frac{\partial^2 v}{\partial x^2} + (\lambda+2\mu)\frac{\partial^2 v}{\partial y^2} \\
&+ C_3\frac{\partial^2 v}{\partial z^2} + (\lambda + C_3)\frac{\partial^2 w}{\partial y\partial z} = 0, \\
&(\lambda+\mu+C_1)\frac{\partial^2 u}{\partial x\partial z} + (\lambda + C_3)\frac{\partial^2 v}{\partial y\partial z} + C_1\frac{\partial^2 w}{\partial x^2} \\
&+ C_3\frac{\partial^2 w}{\partial y^2} + (\lambda+\mu)\frac{\partial^2 w}{\partial z^2} = 0,
\end{aligned} \quad (15)$$

where λ and μ are the Lamé constants and

$$C_1 = \frac{\tau_S}{\gamma_1}, \quad \gamma_1 = \varepsilon_1 - \varepsilon_3; \quad C_2 = \mu - \frac{\mu\gamma_1 - \tau_S}{2\gamma_2},$$

$$\gamma_2 = \varepsilon_1 - \varepsilon_2, \quad C_3 = \mu - \frac{\mu\gamma_1 - \tau_S}{2\gamma_3}, \quad \gamma_3 = \varepsilon_2 - \varepsilon_3.$$

In addition, in the onset of the incomplete plasticity,

$$\tau_S = \mu\gamma_1 = \mu\gamma_2; \quad (16)$$

i.e.,

$$C_1 = C_2 = C_3 = \mu.$$

The comparison with the Lamé equations shows that a change of the type of equations for the displacements or displacement velocities occurs. Namely, the elliptic type of equations in the elasticity theory is changed to the degenerate hyperbolic type. Thus, although the system has two real-valued characteristic surfaces, higher derivatives calculated along the second principal direction cannot be determined. This fact is evident and justified from the physical point of view, because these surfaces correspond to the slip surfaces in the case of the preservation of the elastic bonding along the second principal direction.

In the state of complete plasticity ($\sigma_2 = \sigma_3$), the system is statically determinate and, according to [1], has the form

$$\begin{aligned} &K\frac{\partial^2 u}{\partial x^2} + C_4\frac{\partial^2 u}{\partial y^2} + C_1\frac{\partial^2 u}{\partial z^2} \\ &+ (K + C_4)\frac{\partial^2 v}{\partial x\partial y} + (K + C_1)\frac{\partial^2 w}{\partial x\partial z} = 0, \\ &(K + C_4)\frac{\partial^2 u}{\partial x\partial y} + C_4\frac{\partial^2 v}{\partial x^2} + K\frac{\partial^2 v}{\partial y^2} + K\frac{\partial^2 w}{\partial y\partial z} = 0, \\ &(K + C_1)\frac{\partial^2 u}{\partial x\partial z} + K\frac{\partial^2 v}{\partial y\partial z} + C_1\frac{\partial^2 w}{\partial x^2} + K\frac{\partial^2 w}{\partial z^2} = 0. \end{aligned} \quad (17)$$

Here, K is the compression modulus:

$$K = \lambda + \frac{2}{3}\mu, \quad C_1 = \frac{\tau_S}{\gamma_1}, \quad C_4 = \frac{\tau_S}{\gamma_2}.$$

The analysis of the system shows its hyperbolic nature. Its characteristic surface forms a circular cone with the axis directed along the first principal direction, which is also characteristic.

REFERENCES

1. L. D. Ivlev and A. Yu. Ishlinskiĭ, Dokl. Akad. Nauk **368**, 333 (1999) [Dokl. Phys. **44**, 642 (1999)].
2. B. D. Annin, Prikl. Mekh. Tekh. Fiz. **40**, 181 (1999).
3. E. I. Shemyakin, Dokl. Akad. Nauk **373**, 632 (2000) [Dokl. Phys. **45**, 419 (2000)].
4. E. I. Shemyakin, Fiz. Mezomekh. **2** (6) (1999).
5. S. B. Batdorf and B. Budiansky, *Mathematical Theory of Plasticity Based on the Concept of Slip* (US Government Printing Office, Washington, 1949), NACA Tech. Note No. 1871.
6. S. A. Khristianovich and E. I. Shemyakin, Izv. Akad. Nauk SSSR, Mekh. Tverd. Tela, No. 4, 87 (1967).
7. A. Haar and Th. Kármán, Nachr. Ges. Wiss. Göttingen, Math. Phys. Kl. **2**, 204 (1909).
8. S. A. Khristianovich and E. I. Shemyakin, Izv. Akad. Nauk SSSR, Mekh. Tverd. Tela, No. 5, 138 (1969).

Translated by Yu. Verevochkin

Doklady Physics, Vol. 46, No. 2, 2001, pp. 132–134. Translated from Doklady Akademii Nauk, Vol. 376, No. 6, 2001, pp. 760–762.

MECHANICS

Fracture Toughness of Materials and Continuum Damage Mechanics

Academician V. V. Bolotin

Received November 1, 2000

The continuum-mechanics approach to studies of damages was initiated by L.M. Kachanov and Yu.N. Rabotnov [1], who introduced the concept of damage measure. This measure characterizes the density of microcracks, micropores, plastic microstrains, and other newborn defects. These defects have a small scale compared to the body's dimensions but large compared, e.g., to the crystal-lattice parameters and other microscopic-level characteristics inherent in solid-state physics. The Kachanov–Rabotnov phenomenological damage measure is a scalar ω acquiring its values within the range $0 \le \omega \le 1$. Here, the lower and upper values correspond to the virgin nondamaged and completely damaged materials, respectively. Being applied to the states close to unidirectional tension, this measure is often interpreted as the relative decrease in the effective cross-sectional area. In this form, this measure is used in machine-design calculations against creep fracture [1–3].

It is evident that the damage orientational distribution plays an essential role, so that the damage level should be characterized by tensor quantities. In the first attempt at damage tensorial treatment [4], a second-rank symmetric tensor similar to that describing the density of dislocations was introduced to characterize the spatial distribution of microcracks. To date, a number of various measures have been proposed to describe the dispersed damage of materials, including tensors of second, fourth, etc. ranks [5, 6]. A new branch of solid-state mechanics, namely, continuum damage mechanics, is being intensely developed. The lack of experimental data and a certain freedom in choosing damage measures seems to generate a wealth of literature represented, e.g., by [6]. The conventional approach is the following: assumed damage measures are treated as complementary internal parameters which are introduced into equations for the free energy, dissipation rate, etc. The constitutive equations are developed in a standard way and, in contrast to classical equations of mechanics, are supplemented by kinetic equations describing the process of damage accumulation. The resulting system of equations is usually illustrated by simple, most often one-dimensional, examples.

The basic disadvantage of the current state of continuum damage mechanics is the fact that it is weakly confirmed by experimental data. Although the fractographic patterns of micro-damages are studied in detail, the passage to phenomenological models of continuum mechanics remains ambiguous. Usually, the level of damage attained is associated with the growth of the material's compliance, in particular, with the decrease in elastic moduli. However, the effect of small and moderate damages on the material's compliance is low, whereas a high damage level is accompanied, as a rule, by significant macroscopic plastic deformations and/or formation of macroscopic cracks.

The goal of this study is to substantiate a direct and clear relationship between damage measures and a material's macroscopic parameters which can be easily measured in laboratory conditions. To do this, we need to study macroscopic parameters more sensitive to damage level than the elastic moduli and other characteristics of the material's stiffness. This condition is satisfied by using the magnitude of the specific fracture work as a macroscopic parameter, i.e., the amount of energy spent for the formation of a unit of the new crack surface. The process of fatigue-crack growth, as well as the development of other cracklike defects is, basically, controlled by the interaction of two mechanisms. The first is the accumulation of damages near the crack tips; the second is the general balance of energy and forces in the system composed of the cracked body and a load. A crack grows when the magnitude of the specific fracture work reduces, due to damage accumulation, to a level where the state of the system becomes unstable or, at least, neutral [7–9]. The amount of energy spent on the crack-tip propagation can be easily calculated on the basis of force-displacement relationships obtained experimentally. Thus, following the evolution of the specific fracture work in the process of damage accumulation, we can yield a qualitative evaluation of the phenomenological damage measure.

The other problem is the study of the geometric properties of the damage measure. In particular, the

Blagonravov Institute of Engineering Science, Russian Academy of Sciences, ul. Griboedova 4, Moscow, 102830 Russia

1028-3358/01/4602-0132$21.00

rank of tensors characterizing the angular distribution of damages is of interest. Up to now, attention was attracted to materials whose properties were close to isotropic. However, to analyze tensor properties, we have to turn to strongly anisotropic materials, such as composites of laminate and fiber structure. The compliance and strength parameters of these composites may differ by several orders of magnitude. Even within a stacking plane, i.e. in the case of interlayer deformation and fracture, the magnitude of the specific fracture work is significantly direction-dependent. For example, the mean value of the specific fracture work along and across a unidirectional fiber-reinforced glass-epoxy composite differs approximately by a factor of two. A similar picture is observed while testing textile glass-epoxy composites, for which the difference attains approximately a factor of three.

Treating a composite as a quasi-homogeneous orthotropic solid, we attribute the axes of symmetry to the principal axes of a certain second-rank tensor and consider the material parameters related to these axes as the principal values of this tensor. Testing specimens with an oblique orientation of principal axes, we can also assess nondiagonal components of the tensor [9].

When a specimen cut out in the oblique direction from an orthotropic composite plate is subjected to tearing, the normal to the crack front deviates from the direction of the tearing force. To describe this phenomenon, we should use, at least, a second-order matrix, such as

$$\gamma = \begin{pmatrix} \gamma_{11} & \gamma_{12} \\ \gamma_{21} & \gamma_{22} \end{pmatrix}. \quad (1)$$

In this case, only a part of the newly formed crack area may be related to the contribution of the diagonal elements of this matrix. Namely, nondiagonal matrix elements $\gamma_{12} = \gamma_{21}$ which are naturally assumed to be symmetric correspond to the formation of "skew" areas. These areas are limited by the crack front and the line normal to the direction of the tearing force. Varying the angle between the direction of this force and the direction of one of the composite principal axes, we are afforded the possibility of comparing the values of the specific fracture work with the results given by the elementary transformations for the elements of the second-rank tensor:

$$\begin{aligned} \gamma_{11} &= \gamma_1 \cos^2\theta + \gamma_2 \sin^2\theta, \\ \gamma_{12} &= \gamma_{21} = \frac{\gamma_1 - \gamma_2}{2} \sin 2\theta. \end{aligned} \quad (2)$$

Here, γ_1 and γ_2 are the values of specific fracture work while tearing along the principal axes and θ is the angle between the principal axis 1 and the tearing-force direction. A satisfactory agreement between the experimental results and the calculations based on expressions (2) is observed, although a spread of the experimental results is noticeable.

Measuring the specific fracture work for initially damaged specimens opens a path to numerical evaluation of damage measures. Based on the model given by expressions (1) and (2), we introduce the phenomenological damage measures ω_1 and ω_2 in the case of tearing along the principal axes:

$$\omega_1 = 1 - \frac{\gamma_1}{\gamma_1^0}, \quad \omega_2 = 1 - \frac{\gamma_2}{\gamma_2^0}. \quad (3)$$

Here, γ_1^0 and γ_2^0 are the magnitudes of specific fracture work along the principal axes for a virgin material. Thus, the phenomenological damage measures can be interpreted as a relative decrease in the specific fracture work along the principal axes. Then, we assume that the interlayer damage may be described by a symmetric matrix,

$$\omega = \begin{pmatrix} \omega_{11} & \omega_{12} \\ \omega_{21} & \omega_{22} \end{pmatrix}, \quad (4)$$

whose components are connected with the principal damage measures ω_1 and ω_2 (3) by relationships similar to (2). We may interpret the matrix (4) as a matrix corresponding to a second-rank damage tensor.

In modeling the fatigue-crack growth, it is necessary to distinguish at least two types of damages, namely, damage produced by the cyclic normal stress acting in the plane of the expected crack propagation and that produced by the cyclic tangential stress. Let normal $\Delta\sigma_n$ and tangential $\Delta\tau_n$ stresses act in the plane with the normal n. Equations for the damage accumulation may be written out in the form

$$\begin{aligned} \frac{\partial \omega_n}{\partial N} &= \left(\frac{\Delta\sigma_n - \Delta\sigma_{th}}{\sigma_d}\right)^{m_\sigma}, \\ \frac{\partial \omega_\tau}{\partial N} &= \left(\frac{\Delta\tau_n - \Delta\tau_{th}}{\tau_d}\right)^{m_\tau}, \end{aligned} \quad (5)$$

where $\Delta\sigma_n \geq \Delta\sigma_{th}$ and $\Delta\tau_n \geq \Delta\tau_{th}$.

The damage measures $\omega_\tau(N)$ and $\omega_n(N)$ are considered slowly varying functions of the cycle number N. Material parameters (σ_d, τ_d, $\Delta\sigma_{th}$, $\Delta\tau_{th}$, m_σ, and m_τ) are easy to attribute to macroscopic characteristics measured in laboratory tests. In particular, the semiempirical Paris–Erdogan equation and its generalizations contain a number of characteristics that correlate with the parameters entering into Eqs. (5). It was shown [7, 9] that, using Eqs. (5) with properly chosen material parameters, a satisfactory agreement can be attained with numerous experimental data on fatigue crack growth. Note that the damage measures and patterns corresponding to normal and skew cracking are connected with the components ω_{jk} of the matrix (4) by Cauchy relationships.

The proposed simple interpretation of damage measures relates to the two-dimensional case and cracks of the mode I, which propagate in a fixed plane. Mixed-mode fracture cracks accompanied by kinking and branching are often observed in actual conditions. We can easily generalize the model proposed. First, we consider the three-dimensional case when the matrices (1) and (4) are replaced by similar 3×3 matrices. Second, we can introduce three matrices corresponding to modes I, II and III. In the general case, all the modes interact with each other, which results in additional matrices taking this interaction into account. Thus, we arrive at a matrix of dimension 9×9. Under the assumption of symmetry and in the general case of anisotropy, we have to deal with 21 matrix elements. This conclusion corresponds to earlier proposals of describing continuum damage with fourth-rank tensors. Further generalizations yield higher-rank tensors. However, it is difficult to presently propose a set of laboratory experiments realizing a well-conditioned procedure of evaluating components of a fourth rank tensor even in the simplest case of orthotropic media. The actual situation is much more complicated. In solving engineering problems, pure mechanical damage is often accompanied by damages of a nonmechanical nature such as corrosion, hydrogen embrittlement, etc. Allowance for nonmechanical damages requires the introduction of additional damage measures and formulation of relationships taking into account the interaction between measures of different nature [9].

ACKNOWLEDGMENTS

This work was supported in part by the Russian Foundation for Basic Research, project no. 99-01-00282. The author is grateful to V.N. Shchugorev for performing the experimental part of the research.

REFERENCES

1. Yu. N. Rabotnov, *Mechanics of Deformable Solids* (Nauka, Moscow, 1979).
2. *Creep in Structures*, Ed. by A. R. S. Ponter and D. R. Hayhurst (Springer-Verlag, Berlin, 1981).
3. H. Riedel, *Fracture at High Temperature* (Springer-Verlag, Berlin, 1987).
4. A. A. Vakulenko and M. L. Kachanov, Izv. Akad. Nauk SSSR, Mekh. Tverd. Tela, No. 4, 159 (1971).
5. D. Krajcinovic, Int. J. Damage Mech. **4**, 217 (1995).
6. I. Jasuk and M. Ostoja-Starzewski, Int. J. Solids Struct. **35**, 2383 (1998).
7. V. V. Bolotin, Izv. Akad. Nauk SSSR, Mekh. Tverd. Tela, No. 4, 133 (1988).
8. V. V. Bolotin, *Stability Problems in Fracture Mechanics* (Wiley, New York, 1996).
9. V. V. Bolotin, *Mechanics of Fatigue* (CRC Press, Boca Raton, 1999).

Translated by V. Bolotin

Doklady Physics, Vol. 46, No. 2, 2001, pp. 135–139. Translated from Doklady Akademii Nauk, Vol. 376, No. 6, 2001, pp. 763–767.

MECHANICS

Designing Laminated Plates with an Assigned Stiffness

A. G. Kolpakov

Presented by Academician E.I. Shemyakin July 9, 2000

Received July 13, 2000

We consider constructing a general solution to the problem of designing laminated plates, i.e., the set of all designs providing a desired stiffness for a plate.

The solution is obtained by methods of the "convex-combination problem" [1], to which the initial problem can be reduced provided that the Young's moduli of materials are taken as variables (instead of routinely used volume contents). We propose an algorithm of solving the discrete convex-combination problem which can be employed by numerically solving the design problem (excluding the allowance for stiffness).

1. FORMULATION OF THE PROBLEM

We consider a laminated plate with layers disposed in parallel to the coordinate plane and formed from homogeneous isotropic materials. It is necessary to find the distribution of these materials in the layers which provides the given stiffness (stiffness in the plane, asymmetric stiffness, and flexural stiffness) for the plate.

Let the coordinate y-axis be directed across the plate. In the laminated plate, the Young's modulus $E(y)$ and the Poisson ratio $\nu(y)$ are functions of the variable y.

The design problem is the following. It is required to find the distribution of the material's characteristics providing a given stiffness S^0 for a plate in the plane, an asymmetric stiffness S^1, and a flexural stiffness S^2.

To do this, it is necessary to solve the problem (without a loss of generality, the plate thickness is taken to be 1)

$$\int_{-1/2}^{1/2} \frac{E(y)}{1-\nu^2(y)}dy = S^0,$$
$$\int_{-1/2}^{1/2} \frac{E(y)y}{1-\nu^2(y)}dy = S^1, \quad \int_{-1/2}^{1/2} \frac{E(y)y^2}{1-\nu^2(y)}dy = S^2. \tag{1.1}$$

The integrals in (1.1) yield the expression for the corresponding stiffness of the plate in terms of the elastic constants of its constituent layers [2–5].

For simplicity, we assume that $\nu(y) = \text{const}$. In this case, Eqs. (1.1) are a problem with respect to $E(y)$. In practice, in plate designing, a finite (often small) number of materials is used.

For discretization of the problem, we divide the plate into m layers of equal thickness $\frac{1}{m}$; the function $E(y)$ is constant in the intervals $\left[-\frac{1}{2} + \frac{i-1}{m}, -\frac{1}{2} + \frac{i}{m}\right)$. Henceforth, $i = 1, 2, \ldots, m$.

The desired values are E_i. In the physical sense, $E_i \geq 0$. Problem (1.1) can be reduced to the following form:

$$\sum_i x_i = 1, \quad x_i = \frac{E_i}{mS^0} > 0, \quad \sum_i \mathbf{v}_i x_i = \mathbf{v} \in R^2, \tag{1.2}$$
$$v_{li} = \frac{1}{m}\int_{-\frac{1}{2}+\frac{i-1}{m}}^{-\frac{1}{2}+\frac{i}{m}} y^l dy, \quad v_l = \frac{S^l}{S^0},$$
$$l = 1, 2 \quad (\mathbf{v}_i = (v_{i1}, v_{i2}), \mathbf{v} = (v_1, v_2)).$$

The solution (the plate design) is described by the set $(E_1, \ldots, E_b)$ [or the corresponding vector $(x_1, \ldots, x_b)$].

2. THE DISCRETE PROBLEM OF CONVEX COMBINATIONS

We consider the following problem. Let $Z_n \subset [0, 1]$ be a finite set (consisting of n numbers) and $\mathbf{v}_i$, $\mathbf{v} \in R^k$ be the given vectors. It is required to indicate the numbers x_i which are solutions to the following problem:

$$\sum_i \mathbf{v}_i x_i = \mathbf{v}, \quad \sum_i x_i = 1, \tag{2.1}$$

$$x_i \in Z_n, \quad i = 1, 2, \ldots, m. \tag{2.2}$$

Institute of Mathematics, Siberian Division,
Russian Academy of Sciences,
Universitetskiĭ pr. 4, Novosibirsk, 630090 Russia

1028-3358/01/4602-0135$21.00

Problem (2.1) with the condition

$$0 \le x_i \le 1 \tag{2.3}$$

is the convex-combination problem (CCP) considered previously in [1, 2].

We remove discreteness condition (2.3) and replace it by condition (2.4). The general solution to CCP (2.1), (2.3) is known and has the form [1, 2]

$$x_i = \sum_{\gamma=1}^{M} P_{i\gamma}\lambda_\gamma, \quad i = 1, 2, \ldots, m, \tag{2.4}$$

where $\mathbf{P}_\gamma = (P_{1\gamma}, \ldots, P_{m\gamma})$ is a certain finite set of solutions to CCP (2.1), (2.4) and λ_γ ($\gamma = 1, 2, \ldots, M$) are arbitrary numbers satisfying the conditions

$$\sum_{\gamma=1}^{M} \lambda_\gamma = 1, \quad 0 \le \lambda_\gamma \le 1. \tag{2.5}$$

In other words, the set $\Lambda(\mathbf{v})$ of solutions to CCP (2.1), (2.2), (2.4) has the form $\Lambda(\mathbf{v}) = \mathrm{conv}\{\mathbf{P}_\gamma, \gamma = 1, 2, \ldots, M\}$. The method of constructing the set of vectors $\{\mathbf{P}_\gamma, \gamma = 1, 2, \ldots, M\}$ is described in [1, 2].

The set $Z_n^m = \{\mathbf{x}: x_i \in Z_n\}$ represents the discrete net in R^m. The set of solutions to CCP (2.1)–(2.3) is $\Lambda(\mathbf{v}) \cap Z_n^m$.

Problem (2.1), (2.2) is solved if we indicate the vectors given by formulas (2.4), (2.5) and satisfying the condition $x_i \in Z_n$.

Relationships (2.4), (2.5) can be considered as the CCP with respect to λ_γ. From the convexity of the set $\Lambda(\mathbf{v})$, it follows that, if the first $i - 1$ equations in (2.4) are satisfied, the subsequent ith equation is solvable if and only if

$$x_i \in I_i = [\min_i, \max_i]. \tag{2.6}$$

The interval I_i is, generally speaking, dependent on $x_1, \ldots, x_{i-1}$.

From (2.6), we obtain the necessary and sufficient condition for the existence of the solution to the discrete CCP:

$$Z(i) = Z_n \cap I_i \neq \varnothing \text{ for all } i. \tag{2.7}$$

Since the intervals I_i depend on $x_1, \ldots, x_{i-1}$, a T tree appears. Its top $T(0)$ corresponds to $i = 1$, i.e., to the absence of the solution. The branching at the level $T(i - 1)$ corresponds to the points $Z(i)$. An arbitrary branch coming from the root $T(0)$ to the level $T(m)$ yields the solution (2.1), (2.2) to the discrete CCP. On the contrary, the branch coming from the root $T(0)$ to the level $T(m)$ corresponds to an arbitrary solution of the discrete CCP. Thus, the indicated tree yields the set of all the solutions to the discrete CCP.

3. NUMERICAL ALGORITHMS

The numerical algorithm involves the following stages.

The passage from CCP (2.1), (2.3) to CCP (2.4), (2.5), i.e., the construction of the set of vectors $\{\mathbf{P}_\gamma, \gamma = 1, 2, \ldots, M\}$. The set of vectors can be constructed on the basis of the convolution algorithm described previously in [1, 2].

The test of the solvability of CCP (2.4), (2.5) for the right-hand sides from the set Z_n (constructing the intervals I_i). Since only the interval $[\min_i, \max_i]$ but not the solutions to (2.4), (2.5) are of interest to us, we can use the simplex method, which requires lesser computer memory than the convolution method. To do this, the first $i - 1$ equations from (2.4) and Eq. (2.5) are considered at the $(i - 1)$th step as constraints and the goal function $L(\lambda)$ is constructed on the basis of the ith equation from (2.4):

$$L(\lambda) = \sum_{\gamma=1}^{M} P_{i\gamma}\lambda_\gamma. \tag{3.1}$$

We also consider the problem

$$L(\lambda) \to \min(\max). \tag{3.2}$$

Constructing the tree. The tree can be constructed in an arbitrary manner, because its dimensions turn out to be not very large.

Thus, the numerical algorithm of the solution to the discrete CCP is reduced to solving well-known problems, namely, the CCP and the linear-programming problem.

4. SOLVABILITY OF A CCP AND THE STRUCTURE OF ITS SOLUTION

We consider a relatively internal point $\mathbf{x}$ of the set $\Lambda(\mathbf{v})$, i.e., the point for which we can find the vector $\mathbf{y}$ and the number δ, such that $\mathbf{x} + \mathbf{y}\tau$ lies in $\Lambda(\mathbf{v})$ for $0 < \tau < \delta$. Substituting $\mathbf{x} + \mathbf{y}\tau$ into relationships (2.1), (2.2) and differentiating them with respect to τ, we obtain that the vector $\mathbf{y}$ satisfies the equalities

$$\sum_i \mathbf{v}_i y_i = 0 \in R^2, \quad \sum_i y_i = 0. \tag{4.1}$$

Introducing the vectors $\mathbf{w}_j = (v_{1j}, \ldots, v_{mj})$, $\mathbf{w}_0 = (1, \ldots, 1)$, we can rewrite (4.1) in the form $\mathbf{w}_i\mathbf{y} = 0$, $j = 0, 1, 2$ for each vector connecting the relatively internal points. This implies that the set $\Lambda(\mathbf{v})$ lies in the hyperplane given by Eqs. (4.1) and has the dimension $m - 3$ [we recall that the solutions to CCP (2.1), (2.3) are the elements of the set R^m].

By virtue of this property, problem (2.4), (2.5) for an arbitrarily given $\mathbf{x}$, as a rule, has no solutions, because a random presence of a point in the hyperplane has a zero probability (this is only observed in the numerical calculation for an arbitrary set of desired stiffness).

In this connection, it is possible to propose perturbing the set $\{\mathbf{P}_\gamma, \gamma = 1, 2, \ldots M\}$ with the goal of yielding a solidity (i.e. the dimension m) for a convex shell of the perturbed set. From (4.1), it follows that it should perturb the set $\{\mathbf{P}_\gamma, \gamma = 1, 2, \ldots, M\}$ by the vectors $\mathbf{w}_i$, $j = 0, 1, 2$ [which are the solutions to (4.1) and are "perpendicular" to $\Lambda(\mathbf{v})$].

We now consider the perturbation of the set $\{\mathbf{P}_\gamma, \gamma = 1, 2, \ldots, M\}$ in the form $\{\mathbf{P}_\gamma + r\xi\mathbf{w}_{\gamma \bmod 3}, \gamma = 1, 2, \ldots, M\}$, where ξ is the random value uniformly distributed over the interval [0, 1], r is the characteristic value of the perturbance, and the subscript mod implies the division with respect to modulus. With the probability equal to unity, $\mathrm{conv}\{\mathbf{P}_\gamma + r\xi\mathbf{w}_{\gamma \bmod 3}\}$ has the dimension m.

Let problem (2.5) with the vectors $\{\mathbf{P}_\gamma + r\xi\mathbf{w}_{\gamma \bmod 3}, \gamma = 1, 2, \ldots, M\}$ instead of vectors $\{\mathbf{P}_\gamma, \gamma = 1, 2, \ldots, M\}$ have the solution $\mathbf{x}$. This solution is representable in the form of a convex combination:

$$\mathbf{x} = \sum_{\gamma = 1}^{M} (\mathbf{P}_\gamma + r\xi\mathbf{w}_{\gamma \bmod 3})\lambda_\gamma. \tag{4.2}$$

Substituting this expression into the former equation of (2.1) and taking into account that $\{\mathbf{P}_\gamma, \gamma = 1, 2, \ldots, M\}$ satisfies equalities (2.1), we obtain

$$\left| \sum_{\gamma = 1}^{M} \sum_i \mathbf{v}_i (P_{i\gamma} + r\xi\mathbf{w}_{i\gamma \bmod 3}) - \mathbf{v} \right| \le \sum_i |\mathbf{v}_i r\xi w_i|.$$

The last expression corresponds to the error with which the solution $\mathbf{x}$ satisfies the first equation of (2.1). This quantity is seen to have an order r.

5. NUMERICAL TESTS

We composed codes to obtain the simplicial solutions to the CCP, to construct the tree, and to solve the linear-programming problem.

Test problem. The following test problem was used. A certain structure E_i^* of the laminated plate was given, and the values of the stiffness S^ν ($\nu = 0, 1, 2$) were calculated for it according to formulas (1.1). Then, the design problem was solved for these stiffness. Within the set of its solutions, the solution E_i^* must be present. This property was verified and confirmed by numerical calculations.

Problem with a perturbed set $\{\mathbf{P}_\gamma, \gamma = 1, \ldots, M\}$. As a typical example, we present the following problem. The number of layers is $m = 7$. The design $\{E_i^*, i = 1, \ldots, 7\} = \{3, 5, 3, 5, 3, 5, 3\}$ is taken as known. The corresponding stiffness are $S^0 = 3.8571$, $S^1 = 0$, and $S^2 = 1.1348$. The number of solutions to CCP (2.1), (2.4) is $M = 12$.

For the design, the set of materials $Z_6 = \{1, 2, 3, 5, 7, 10\}$ is used.

The perturbation parameter was taken to be $r = 0.05$. Here, we present the number of nodes of the T tree at various levels:

Level i	0	1	2	3	4	5	6	7
Number of nodes	1	5	19	49	157	80	12	4

The following designs were obtained: $E_1 = \{5, 3, 5, 5, 1, 7, 1\}$, $E_2 = \{3, 5, 5, 5, 1, 5, 3\}$, $E_3 = \{3, 5, 3, 5, 3, 5, 3\}$, and $E_4 = \{1, 7, 3, 5, 3, 3, 5\}$. The design E_3 coincides with the initial design.

The stiffness $S^0 = 3.857$ and $S^2 = 1.135$ are the same for all designs obtained, while the values of the stiffness S^1 are equal to 0.163, 0.245, 0.000, and 0.082, respectively.

Examples of other numerical calculations are given in [6].

6. THE DESIGN PROBLEM WITH ALLOWANCE FOR THE STRENGTH AND THE AVERAGED STRENGTH CRITERION

Above, we described the method of solving the problem of designing laminated plates with desired stiffness characteristics. The complete solution to this problem must take into account the strength requirements. We show that the design algorithm proposed is also applicable to solving the design problem with allowance for strength.

Preliminary, we introduce the averaged strength criterion. As that for a composite plate, we imply such a criterion which, being written in terms of the characteristics of a plate as a two-dimensional object, enables us to estimate its strength as a three-dimensional (although thin) heterogeneous body [3–5]. It is possible to obtain such criteria in the case of the existence of formulas connecting local stresses σ_{ij}^ε in a plate (considered as a three-dimensional body) with its deformation characteristics as a two-dimensional object.

For a laminated plate, such formulas were obtained, e.g., in [4, 5], and have the form

$$\begin{aligned} &\sigma_{ij}^\varepsilon = c_{ij\alpha\beta}(y)[\varepsilon_{\alpha\beta} + y\rho_{\alpha\beta}], \\ &i, j = 1, 2, 3, \quad \alpha, \beta = 1, 2, \end{aligned} \tag{6.1}$$

where $y = y_3$ is the coordinate across the plate (as in [1], the plate layers are directed parallel to the plane Ox_1x_2), $c_{ijkl}(y)$ is the elastic-constant tensor, $\varepsilon_{\alpha\beta}$ is the strain tensor in the plate plane, and $\rho_{\alpha\beta}$ is the curvature tensor.

Using the relation between $\varepsilon_{\alpha\beta}$, $\rho_{\alpha\beta}$, and the forces $N_{\alpha\beta}$ in the plate plane and the moments $M_{\alpha\beta}$,

$$\begin{aligned} N_{\alpha\beta} &= S^0_{\alpha\beta\gamma\delta}\varepsilon_{\gamma\delta} + S^1_{\alpha\beta\gamma\delta}\rho_{\gamma\delta}, \\ M_{\alpha\beta} &= S^1_{\alpha\beta\gamma\delta}\varepsilon_{\gamma\delta} + S^2_{\alpha\beta\gamma\delta}\rho_{\gamma\delta}, \end{aligned} \tag{6.2}$$

we can express $\sigma^{\varepsilon}_{ij}$ in terms of $N_{\alpha\beta}$ and $M_{\alpha\beta}$ ($\alpha, \beta, \gamma, \delta = 1, 2$).

We consider the case where the Poisson ratios for materials coincide. In this case, the elastic-constant tensor can be represented in the form

$$c_{ijkl}(y) = E(y)c^0_{ijkl}, \tag{6.3}$$

where c^0_{ijkl} is independent of y and $E(y)$ is the Young's modulus.

In this case, if the ith layer $\left[-\frac{1}{2} + \frac{i-1}{m}, -\frac{1}{2} + \frac{i}{m}\right)$ of the plate is occupied by the Kth material [$E(y) = E_K$ in the layer under consideration], the local stresses in this layer are

$$\begin{aligned} &\sigma^{\varepsilon}_{ij} = E_K c^0_{ijkl}[\varepsilon_{\alpha\beta} + y\rho_{\alpha\beta}], \\ &y \in \left[-\frac{1}{2} + \frac{i-1}{m}, -\frac{1}{2} + \frac{i}{m}\right). \end{aligned} \tag{6.4}$$

We recall that a unit-thickness plate (or that transformed to such a plate by a proper replacement of the variable) is considered.

Let the strength criterion for the Kth material be written in the form

$$f_K(\sigma^{\varepsilon}_{ij}) < 1, \tag{6.5}$$

where f_K is the nonnegative Lipschitz function.

Substituting (6.4) into (6.5), we obtain the averaged strength criterion for the ith layer under the condition that this layer is occupied by the Kth material:

$$F_K(y, \varepsilon_{\alpha\beta}, \rho_{\alpha\beta}) \equiv f_K(E_K c^0_{ijkl}[\varepsilon_{\alpha\beta} + y\rho_{\alpha\beta}]) < 1. \tag{6.6}$$

The partition into layers was carried out with a step $\frac{1}{m}$. In this case, with an accuracy to $\frac{M}{m}$ (M is the maximum of the Lipschitz constants for the functions f_K; $k = 1, 2, \ldots, n$), we can replace (6.6) by the condition

$$\begin{aligned} &F_K(\varepsilon_{\alpha\beta}, \rho_{\alpha\beta}) \\ &\equiv f_K\left(E_K c^0_{ijkl}\left[\varepsilon_{\alpha\beta} + \left(-\frac{1}{2} + \frac{i}{m}\right)\rho_{\alpha\beta}\right]\right) < 1. \end{aligned} \tag{6.7}$$

Constructed according to the design ($E_1, \ldots, E_m$) or ($x_1, \ldots, x_m$), the plate conserves the integrity of all its layers if condition (6.7) is fulfilled for all $i = 1, 2, \ldots, m$. In the case of violation of conditions (6.6) or (6.7), the destruction of a certain layer takes place {i.e., (6.6) and (6.7) are the strength conditions "with respect to the first crack" [3–5]}. Condition (6.7) is an approximate condition with an accuracy of $\frac{M}{m}$.

7. THE DESIGN PROBLEM WITH ALLOWANCE FOR STRENGTH

The descriptive formulation of the problem is the following: It is required to indicate all the designs providing the desired stiffness for a plate and making it possible not to be destroyed while enduring the strains $\varepsilon_{\alpha\beta}$ and $\rho_{\alpha\beta}$ (or the loads $N_{\alpha\beta}$ and $M_{\alpha\beta}$).

The formalized setting of the problem with allowance for the above-said is the following: it is necessary to solve problem (2.1), (2.2) under condition (6.7).

The algorithm proposed in Section 2 is coordinated with the formulated problem. To obtain the designs desired, it suffices to use condition (6.7) as a filter at a recurrent step of this algorithm. For substantiating this statement, we turn to the description of the algorithm step which was presented in Section 2. At the ith step, we supplement the previously available fragment of the design $x_1, \ldots, x_{i-1}$ with the quantity x_i satisfying condition (6.6).

We modify this algorithm in the following manner. Let x_R satisfy (6.6) (we change the subscripts in order for i and R to number a layer and a type of a material, respectively). In this case, we verify the validity of the condition

$$\begin{aligned} &F_{R,i}(\varepsilon_{\alpha\beta}, \rho_{\alpha\beta}) \\ &\equiv f_R\left(E_R c^0_{ijkl}\left[\varepsilon_{\alpha\beta} + \left(-\frac{1}{2} + \frac{i}{m}\right)\rho_{\alpha\beta}\right]\right) < 1. \end{aligned} \tag{7.1}$$

If condition (3.1) holds, then $x_R = \frac{E_R}{mS^0}$ is taken as a possible value; otherwise, this equality is discarded. We deal with the algorithm from Section 2, in which the condition $x_i \in I_i$ is replaced by the condition $\{x_R \in I_i\} \cap \{\text{for } x_R, \text{ condition (7.1) is fulfilled}\}$ (i.e., supplementary condition (7.1) is posed, which we call the strength-condition filter).

Condition (7.1) is obvious from the mechanical standpoint. This is the test for a material with the Young's modulus E_R (x_R and E_R are unambiguously interrelated, see Section 2) as a candidate for the filling in with this material of the ith layer. The efficiency of modifying the algorithm to take into account its strength is related to its locality (layer-by-layer constructing of the plate design by this algorithm), which successfully coincides with the locality of strength criterion (6.7) (written for the given layer).

In the case of setting the load (i.e., $N_{\alpha\beta}$ and $M_{\alpha\beta}$), the values of $\varepsilon_{\alpha\beta}$ and $\rho_{\alpha\beta}$ can be calculated using $N_{\alpha\beta}$,

$M_{\alpha\beta}$ and the given stiffness. In this connection, we again arrive at the above problem.

REFERENCES

1. A. G. Kolpakov and I. G. Kolpakova, in *Proceedings of the XIII World Congress on Computational and Applied Mathematics, IMACS'91, Trinity College, Dublin, 1991*, Vol. 4, p. 1955.
2. A. G. Kolpakov, Zh. Vychisl. Mat. Mat. Fiz. **32**, 1323 (1992).
3. A. G. Kolpakov and I. G. Kolpakova, Comput. Struct. **57**, 599 (1995).
4. B. D. Annin, A. L. Kalamkarov, A. G. Kolpakov, and V. Z. Parton, *Calculation and Design of Composite Materials and Structural Elements* (Nauka, Novosibirsk, 1993).
5. A. L. Kalamkar and A. G. Kolpakov, *Analysis, Design and Optimization of Composite Structures* (Wiley, Chichester, 1997).
6. A. G. Kolpakov, Zh. Vychisl. Mat. Mat. Fiz. **40** (2) (2000).

Translated by V. Bukhanov

Doklady Physics, Vol. 46, No. 2, 2001, pp. 140–143. Translated from Doklady Akademii Nauk, Vol. 376, No. 6, 2001, pp. 768–771.

MECHANICS

On Body Shapes Providing Maximum Penetration Depth in Dense Media

G. E. Yakunina

Presented by Academician G.G. Chernyĭ July 13, 2000

Received July 14, 2000

For a given body-base area and constraints imposed on both the length and transverse dimensions of the body, the problem of its shape providing the maximum depth of penetration into dense media is solved within the framework of the model of local interaction.

STATEMENT OF THE PROBLEM

Let a body penetrate into a medium normally to its free surface in the direction opposite to the axis given by the unit vector **x**. We assume that at an initial time moment, the body is entirely immersed in the medium and has a velocity U_0. We write out the resistance experienced by the penetrating body in the form

$$D = \iint_S [\sigma_n(\mathbf{n}\cdot\mathbf{x}) + \sigma_\tau(\boldsymbol{\tau}\cdot\mathbf{x})]dS. \quad (1)$$

Here, σ_n and σ_τ are the normal and tangential stresses on the body surface, respectively; **n** and $\boldsymbol{\tau}$ are the unit vectors of the inner normal and the tangent to a surface element, respectively; and integration is performed over the body surface S.

We now study the interaction between the medium and the surface S within the framework of a local model. To do this, we consider the stresses to be given by two-term sums containing a constant term and a dynamic one proportional to the body velocity U squared:

$$\begin{aligned}\sigma_n &= A_1U^2(\mathbf{n}\cdot\mathbf{x})^2 + C_1,\\ \sigma_\tau &= A_2U^2(\mathbf{n}\cdot\mathbf{x})^2 + C_2.\end{aligned} \quad (2)$$

Here, A_k and C_k are positive constant model parameters dependent on the characteristics of the medium ($k = 1, 2$).

We introduce the notation $\alpha = (\mathbf{n}\cdot\mathbf{x})$. Within the framework of the model, the vector $\boldsymbol{\tau}$ lies on a sliding plane for particles of the medium, with $(\boldsymbol{\tau}\cdot\mathbf{x}) = (1 - \alpha^2)^{1/2}$, and the surface S is the upstream part of the body surface on which the condition

$$0 \le \alpha \le 1 \quad (3)$$

is satisfied.

With regard to the assumptions accepted, we rewrite (1) in the form

$$D(U) = D_1U^2 + D_2, \quad (4)$$

$$D_i = \iint_S f_i(\alpha)\alpha dS, \quad i = 1, 2, \quad (5)$$

$$f_1(\alpha) = \alpha^2(A_1 + \gamma A_2), \quad f_2(\alpha) = C_1 + \gamma C_2,$$

$$\gamma = \frac{\sqrt{1-\alpha^2}}{\alpha}.$$

The values of integrals (5) are independent of the velocity U. This allows us to integrate the equations of motion for a body with mass M subjected to the action of force (4). As a result, the penetration depth for the body in the medium is given by the expression (cf. [1, 2])

$$H = \frac{M}{2D_1}\ln\left(\frac{D_0}{D_2}\right), \quad D_0 = D(U_0). \quad (6)$$

For a given velocity U_0 and mass M, the penetration depth H depends on the body shape. We will seek the body shape providing the maximum value of H in a class of bodies with piecewise smooth surface S and base area S_b, which are interrelated by the expression

$$\iint_S \alpha dS = S_b. \quad (7)$$

Let the surface S be described by the equation $x = \chi(\rho, \theta)$ in the cylindrical coordinates (x, ρ, θ), where χ is a one-valued function of points lying in the body base. Then, $\alpha dS = dS_b = \rho d\rho d\theta$. Denoting the polar

Institute of Mechanics, Moscow State University, Michurinskiĭ pr. 1, Moscow, 117192 Russia

1028-3358/01/4602-0140$21.00

radius of the points in the base contour by $R(\theta)$, we rewrite expressions (5) and (7) in the form

$$D_i = \frac{1}{2}\int_0^{2\pi} d\theta \int_0^{R^2(\theta)} f_i(\alpha)d\rho^2, \quad i = 1, 2, \tag{8}$$

$$\int_0^{2\pi} R^2(\theta)d\theta = 2S_b. \tag{9}$$

As follows from (4), (6), and (8), we obtain the functional H depending on the functions $\alpha(\rho, \theta)$ and $R(\theta)$ that specify the body shape and are independent of each other. With M, U_0, and S_b given, the problem of the body shape providing the maximum depth of penetration is formulated in the following manner: it is necessary to find the functions $\alpha(\rho, \theta)$ and $R(\theta)$ that meet conditions (3) and (9) and provide the maximum of functional (6).

Below, we derive equations for the functions $\alpha(\rho, \theta)$ and $R(\theta)$ for an extremal surface and prove that the function α is constant on this surface.

EXTREMAL SURFACES

The Lagrange function for functional (6) is given in the form

$$\Phi = H(\alpha, R) + \lambda_0 \int_0^{2\pi} R^2(\theta)d\theta,$$

where λ_0 is a constant factor. The Euler equations for the functions $\alpha(\rho, \theta)$ and $R(\theta)$ of an extremal surface are determined from the condition $\delta\Phi = 0$. We present $\delta\Phi$ in the following equivalent forms:

$$\delta\Phi = -K_1[\delta D_0 + K_2\delta D_2] + \lambda_0 \int_0^{2\pi} \delta R^2 d\theta, \tag{10}$$

$$\delta\Phi = -K_3[\delta D_1 + K_4\delta D_2] + \lambda_0 \int_0^{2\pi} \delta R^2 d\theta. \tag{11}$$

In (10) and (11), the quantities K_m (m = 1, 2, 3, 4) depend on the body shape and are determined by the expressions

$$K_1 = \frac{H(1-w)}{D_2(q-1)}, \quad K_2 = \frac{wq-1}{1-w},$$

$$K_3 = K_1U_0^2, \quad K_4 = \frac{1+K_2}{U_0^2},$$

where $q = \dfrac{D_0}{D_2} > 1$, $w = \dfrac{q-1}{q\ln q} < 1$, and K_m (m = 1–4) are always positive. With regard to (4) and (8), we write out the variations δD_i (i = 0, 1, 2) in (10) and (11) in the form

$$\delta D_0 = U_0^2\delta D_1 + \delta D_2,$$

$$\delta D_i = \frac{1}{2}\int_0^{2\pi} d\theta \int_0^{R^2(\theta)} (f_i'(\alpha)\delta\alpha)d\rho^2 + \frac{1}{2}\int_0^{2\pi} (f_i(\alpha_f)\delta R^2)d\theta, \quad i = 1, 2. \tag{12}$$

Here, $\alpha_f = \alpha_f(R(\theta), \theta)$ and $f_i'(\alpha)$ are the derivatives of the functions $f_i(\alpha)$ with respect to the parameter α, which are given by the expressions

$$f_1'(\alpha) = A_1\alpha\left(2 + \frac{A_2(\gamma^2-1)}{A_1\gamma}\right),$$

$$f_2'(\alpha) = -C_2\frac{(\gamma^2+1)}{\alpha\gamma}. \tag{13}$$

Next, we consider representation (11) for $\delta\Phi$. Since the quantities K_3, K_4, and λ_0 are common for the entire surface and $\delta\alpha$ and δR are independent variations, the equality $\delta\Phi = 0$ is satisfied only if the function α meets the conditions

$$f_1'(\alpha) + K_4 f_2'(\alpha) = 0, \tag{14}$$

$$f_1(\alpha_f) + K_4 f_2(\alpha_f) + \lambda = 0, \quad \lambda = -\frac{2\lambda_0}{K_3}. \tag{15}$$

Since Eq. (14) has to be valid at each point on an extremal surface, we determine that the equality

$$\alpha = \alpha^* = \text{const} \tag{16}$$

holds on this surface. The constant α^* in (16) is a root of Eq. (14) provided that this root meets conditions (3) and (15). It can be proven that Eq. (14) has no more than one such root. This results in the extremal surface containing no sections with different values of α. Equation (14) may have no roots. Even in this case, condition (16) remains in force on the extremal surface.

In general, function $H(\alpha)$ (6) of the real argument attains its maximum within the interval [0, 1] when $\alpha = \alpha^*$. The maximum value of $H^* = H(\alpha^*)$ is sought among local and boundary extrema. The function H attains its local extrema for α satisfying Eq. (14), while the boundary extrema are possible for $\alpha = 0$ and $\alpha = 1$. It is worth noting that roots (14) are independent of S_b and α^* is determined only by the characteristics of the medium and the initial velocity U_0 of penetration.

The values of α^* as a function of the parameter $Y = \left(\dfrac{C_2}{A_1U_0^2}\right)^{1/3}$ are presented in Fig. 1. The curves *1* and *2* correspond, respectively, to the model with constant friction, when $A_2 = 0$, $C_2 \neq 0$ and $C_1 = 5C_2$, and the model of Coulomb friction, when $A_2 = \mu_0A_1$, $C_2 = \mu_0C_1$,

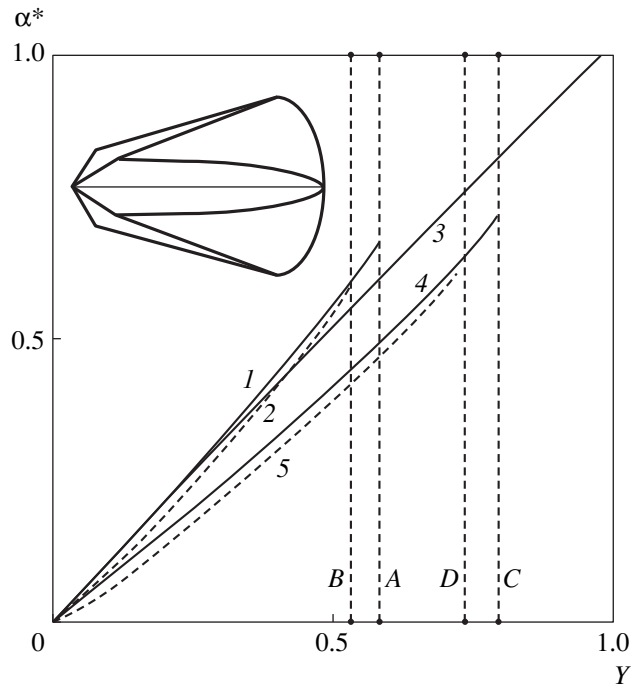

Fig. 1. Values of α^* as a function of parameter Y for the body shape providing (*1–3*) maximum depth of penetration or (*4*, *5*) minimum resistance. The model of constant friction (solid lines) and the model of Coulomb friction (dashed lines) are used. An example of the optimal body shape is shown in the insert.

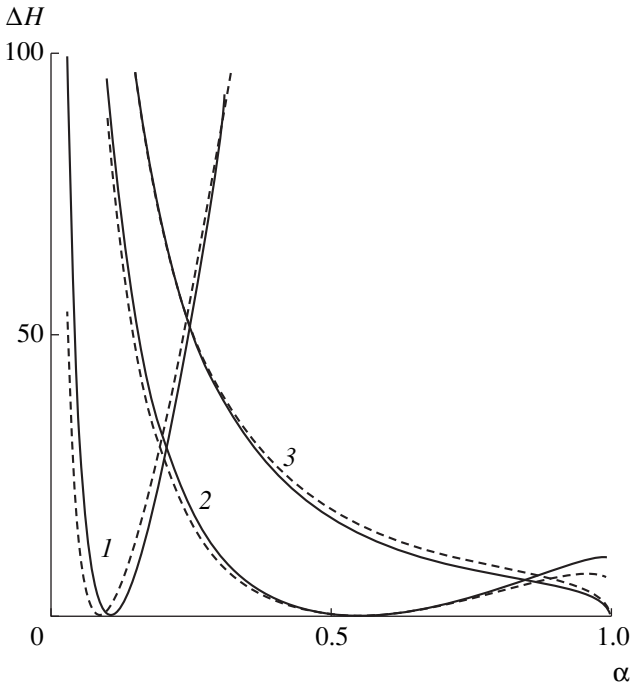

Fig. 2. Relative difference $\Delta H = \left(\frac{H^*}{H_k} - 1\right) \times 100$ as a function of α for Y = (*1*) 0.1; (*2*) 0.5; and (*3*) 0.8. The model of constant friction with $C_1 = 5C_2$ (solid lines) and the model of Coulomb friction with $\mu_0 = 0.2$ (dashed lines) are used.

and $\mu_0 = 0.2$. It is worth noting that curve *3*, which corresponds to the model with constant friction in the thin-body approximation ($\alpha^2 \ll 1$), yields a good fit to α^* for $Y < 0.5$. The local maximum of H coincides with the edge maximum for $Y = Y^*$, where the values of Y^* are shown by the points A and B on the curves *1* and *2*, respectively. For $Y > Y^*$, the body with $\alpha^* = 1$ has the maximum penetration depth.

BODY SHAPES PROVIDING MAXIMUM PENETRATION DEPTH

Condition (16) is similar to that of the minimum resistance for bodies [3, 4]. However, using representation (10) for $\delta\Phi$ with equalities (12) and (13) taken into account, we can prove that the surface of the minimum-resistance body, which is found at an initial stage of penetration with $U = U_0$ and satisfies the condition $\delta D_0 = 0$, is not optimal for functional (6) provided that positive values of $\delta\alpha$ are admissible. Hence, the body surface providing both the maximum penetration depth and the minimum resistance are formed by sections of a circular-cone surface with an opening angle $\beta^* = 2\arcsin\alpha^*$ and planes tangent to the cone. However, the values of α^* for surfaces optimal from the standpoint of resistance and penetration depth are different in these two cases.

For comparison, the values of α^* found for the minimum-resistance body shape in [3] are presented in curves *4* and *5* in Fig. 1. In this case, curves *4* and *5* correspond to curves *1* and *2* (by both the model of friction and the characteristics of the medium), respectively. The body with $\alpha^* = 1$ has minimum resistance provided that $Y > Y^*$, where the values of Y^* are shown by the points C and D on curves *4* and *5*, respectively. For such Y, the body shapes providing minimum resistance and maximum penetration depth coincide.

Condition (16) is obtained under the assumption that only the body-base area S_b is given. However, it was proved in [3, 4] that if, in addition to given S_b, constraints were imposed on the body's length and transverse dimensions, an infinite set of bodies whose surfaces met these constraints and condition (16) could be found. This implies that all such bodies, with S_b given, have the same maximum depth H^* of penetration into the medium provided that the initial conditions, velocity U_0, and mass M are identical. Such optimal bodies may be conical and have a cyclic symmetric (star-shaped) cross section [3]. At the same time, the method developed in [4] and based on condition (16) allows us to find nonconical and asymmetric optimal body shapes. In particular, this method can be used for finding the optimal shape of a body with given length provided that the body base is a circle. An example of such

a body is presented in Fig. 1. The stress action on the surface of a body moving in a dense medium often results in deformation and destruction of the body. The strength for optimal bodies with a circular base is higher than that for conical star-shaped bodies equivalent in their length and base area. Hence, in the case of a dense medium, from the standpoint of optimal shape, such circular-area bodies are preferred over star-shaped bodies.

For various Y, the maximum penetration depth H^* was compared to the penetration depth H_c for circular cones with the same mass and base area as the optimal body. The relative difference $\Delta H = \left(\frac{H^*}{H_k} - 1\right) \times 100$ as a function of α is plotted in Fig. 2 for cones with an opening angle $\beta = 2\arcsin\alpha$. Curves *1*, *2*, and *3* are plotted for $Y = 0.1$, 0.5, and 0.8, respectively. Solid lines in Fig. 2 correspond to the constant-friction model with $C_1 = 5C_2$, and dashed lines correspond to the Coulomb friction model with $\mu_0 = 0.2$. The tangency and intersection of the curves with the abscissa axis in Fig. 2 occur at $\alpha = \alpha^*$.

REMARKS AND CONCLUSIONS

The problem of body shape providing maximum depth of penetration into dense media is solved in the framework of the model of two-term local interaction (2). This model is used for describing the stress on the surface of a body penetrating into a dense medium similar to grounds and metals [1, 2]. The problem is solved without simplifying assumptions concerning the body's geometry [1, 2]. It is proved that the structure of the body shape providing maximum penetration depth coincides with that providing minimum resistance at an initial stage of penetration [3, 4]. However, in the general case, the body shapes optimal from the standpoint of penetration depth and resistance differ from one another.

REFERENCES

1. N. A. Ostapenko, V. I. Romanchenko, and G. E. Yakunina, Prikl. Mekh. Tekh. Fiz., No. 4, 32 (1994).
2. N. A. Ostapenko and G. E. Yakunina, Prikl. Mat. Mekh. **63**, 1018 (1999).
3. G. E. Yakunina, Prikl. Mat. Mekh. **64**, 299 (2000).
4. G. E. Yakunina, Prikl. Mat. Mekh. **64**, 605 (2000).

Translated by V. Chechin

Doklady Physics, Vol. 46, No. 2, 2001, pp. 69–71. Translated from Doklady Akademii Nauk, Vol. 376, No. 4, 2001, pp. 465–467.

PHYSICS

Description of a Charged-Particle Curvilinear Beam in the Small-Angle Approximation

N. D. Naumov

Presented by Academician A.F. Andreev August 15, 2000

Received June 26, 2000

The development of theoretical models describing the penetration of fast charged particles through a medium placed in a magnetic field is of undoubted interest in solving problems of high-energy physics, astrophysics, and physics of the Earth. The possibility of using analytic methods for this goal is caused by the smallness of the single-scattering angle, which results in a substantial simplification of the elastic part of the collision integral in the transport equation. Representation of this integral in differential form made it possible to obtain a number of solutions to the transport equation in small-angle approximation [1–3].

However, the results obtained relate to the case of the motion of a charged-particle flux along the magnetic-field direction, i.e., to a rectilinear beam. For a curvilinear beam, the transport equation in the small-angle approximation is not derived. For example, the problem of the injection of a charged-particle beam at a certain angle to the direction of the uniform magnetic field was studied in [4–7] on the basis of kinetic equation. In this paper, we obtained the transport equation in the small-angle approximation for the problem of penetration of a curvilinear charged-particle beam through a medium placed into a nonuniform magnetic field. For this equation, the Green's functions in the case of ring and spiral beams are also constructed.

In the presence of an external magnetic field **B**, the transport equation has the form

$$\mathbf{\Omega}\frac{\partial N}{\partial \mathbf{x}} + \frac{e}{c}[\mathbf{\Omega}\mathbf{B}]\frac{\partial N}{\partial \mathbf{p}} = S + I_{\text{el}}. \qquad (1)$$

Here, $N(\mathbf{x}, \mathbf{\Omega}, T)$ is the charged-particle flux density; e, m, and T are the particle charge, mass, and kinetic energy, respectively; S is the density of the sources; I_{el} is the elastic part of the collision integral; and

$$\mathbf{p} = \mathbf{\Omega}\frac{\sqrt{T(T+2mc^2)}}{c}.$$

The propagation of the particle beam can be conveniently considered in the curvilinear s, η, ζ-coordinate system:

$$\mathbf{x} = \mathbf{Y}(s) + \eta\mathbf{n} + \zeta\mathbf{b},$$

where $\mathbf{Y}(s)$ is the particle trajectory in the beam axis; s is the trajectory length measured from the beam injection point; and $\mathbf{t}$, $\mathbf{n}$, and $\mathbf{b}$ are the vectors of the Frenet trihedron related to the $\mathbf{Y}(s)$ curve. Substituting the expression for the velocity $\mathbf{v} = u\mathbf{t}$ into the equation for the particle motion occurring in an external magnetic field, we find for the trajectory curvature $\mathbf{Y}(s)$,

$$k = -\frac{e\mathbf{b}\mathbf{B}_0}{cp_0},$$

$$\mathbf{B}_0 = \mathbf{B}(\mathbf{Y}(s)), \quad p_0 = \frac{mu}{\sqrt{1-\frac{u^2}{c^2}}},$$

where p_0 is the particle momentum.

In the new coordinate system, Eq. (1) takes the form

$$\frac{1}{\sigma}\mathbf{t}\mathbf{\Omega}\frac{\partial N}{\partial s} + \left(\mathbf{n}\mathbf{\Omega} + \frac{\kappa}{\sigma}\zeta\right)\frac{\partial N}{\partial \eta} + \left(\mathbf{b}\mathbf{\Omega} - \frac{\kappa}{\sigma}\eta\right)\frac{\partial N}{\partial \zeta} + \frac{e}{c}[\mathbf{\Omega}\mathbf{B}]\frac{\partial N}{\partial \mathbf{p}} = S + I_{\text{el}}, \qquad (2)$$

where κ is the torsion of the curve $\mathbf{Y}(s)$ and $\sigma = 1 - k\eta$.

In the small-angle approximation, $\mathbf{\Omega} \approx \mathbf{t} + \alpha\mathbf{n} + \beta\mathbf{b}$. This allows us to simplify the integral for elastic collisions (provided that the effect of the external magnetic field on the collision process is ignored):

$$I_{\text{el}} = L(T)N, \quad L(T) = \frac{1}{4}\chi^2(T)(L_1 + L_2),$$

$$L_1 = \frac{\partial^2}{\partial\alpha^2}, \quad L_2 = \frac{\partial^2}{\partial\beta^2},$$

where $\chi^2(T)$ is the mean square of the scattering angle per unit path length.

1028-3358/01/4602-0069$21.00

For a narrow beam, when the ratios of its transverse size to the beam curvature radius and the twisting radius are small, the values of $k\eta$, $\kappa\eta$, and $\lambda\zeta$ are low. In addition, we suppose the degree of nonmonoenergeticity of the beam to also be small; i.e., $\tau = \frac{T}{W} - 1$, where $W = c\sqrt{p_0^2 + m^2c^2} - mc^2$ is the particle kinetic energy in the beam axis. Therefore, due to the smallness of the scattering angle, we can assume that $\chi^2(T) \approx \chi^2(W)$. Expanding the external field near the beam axis, $\mathbf{B} = \mathbf{B}_0 + \mathbf{B}_1$, and ignoring terms of the second order of smallness, we find from Eq. (2)

$$\frac{\partial N}{\partial s} + (\alpha + \kappa\zeta)\frac{\partial N}{\partial \eta} + \left(\lambda\beta - k^2\eta - k\tau\Gamma - \frac{e}{cp_0}\mathbf{b}\mathbf{B}_1\right)\frac{\partial N}{\partial \alpha} + (\beta - \kappa\eta)\frac{\partial N}{\partial \zeta} + \left(\frac{e}{cp_0}\mathbf{n}\mathbf{B}_1 - \lambda\alpha\right)\frac{\partial N}{\partial \beta} = S + \Lambda N, \quad (3)$$

where we denote

$$\Gamma = \frac{W + mc^2}{W + 2mc^2}, \quad \lambda = \kappa + \frac{e\mathbf{t}\mathbf{B}_0}{cp_0}, \quad \Lambda = L(W).$$

Equation (3) describes the penetration of a narrow beam of fast charged particles through a medium placed into a nonuniform magnetic field with allowance for the effect of multiple elastic scattering. This equation is simplified for $\kappa = 0$, i.e., in the case when the beam axis is a plane curve. As a particular example, we consider the propagation of a ring beam in a weakly focusing magnetic field with decay index q:

$$\mathbf{B} = B_0[qk\zeta\mathbf{n} + (1 - qk\eta)\mathbf{b}].$$

In this case, Eq. (3) is written out as

$$MN = S, \quad M = \frac{\partial}{\partial s} + M_1 + M_2, \quad (4)$$

where the following notation is introduced:

$$k_1 = k\sqrt{1+q}, \quad k_2 = k\sqrt{q},$$

$$M_1 = \alpha\frac{\partial}{\partial \eta} - (k_1^2\eta + k\tau\Gamma)\frac{\partial}{\partial \alpha} - \Lambda_1,$$

$$M_2 = \beta\frac{\partial}{\partial \zeta} - k_2^2\zeta\frac{\partial}{\partial \beta} - \Lambda_2.$$

The solution to Eq. (4) can be obtained by the method of Green's functions:

$$N(T, X) = \int G(X, X')S(T, X')dX',$$

$$MG(X, X') = \delta(X - X').$$

Here, for the set of variables, the following notation is used:

$$X = \{s, x_1, x_2\}, \quad x_1 = \{\eta, \alpha\}, \quad x_2 = \{\zeta, \beta\}.$$

It is easy to see that the Green's function has the following structure:

$$G(X, X') = \vartheta(s - s')F_1(s, x_1; s', x_1')F_2(s, x_2; s', x_2'),$$

where $\vartheta(x)$ is the Heaviside step-function and the functions F_i satisfy the equation

$$\left(\frac{\partial}{\partial s} + M_i\right)F_i = 0$$

with the initial condition $F_i(s', x_i; s', x_i') = \delta(x_i - x_i')$.

To determine the functions F_i, we should pass from x_i to new variables ξ_i and γ_i:

$$\xi_1 = \left(k_1\eta + \frac{k}{k_1}\tau\Gamma\right)\cos\psi_1 - \alpha\sin\psi_1 - \frac{k}{k_1}\tau\Gamma - k_1\eta',$$

$$\xi_2 = k_2\zeta\cos\psi_2 - \beta\sin\psi_2 - k_2\zeta',$$

$$\gamma_1 = \alpha\cos\psi_1 + \left(k_1\eta + \frac{k}{k_1}\tau\Gamma\right)\sin\psi_1 - \alpha',$$

$$\gamma_2 = \beta\cos\psi_2 + k_2\zeta\sin\psi_1 - \beta',$$

where $\psi_i = k_i(s - s')$. This substitution of variables results in the elimination of terms with first-order derivatives (for brevity, the subscript i is omitted):

$$\frac{\partial F}{\partial s} - \frac{\chi^2}{4}\left(\sin^2\psi\frac{\partial^2 F}{\partial \xi^2} - \sin 2\psi\frac{\partial^2 F}{\partial \xi\partial \gamma} + \cos^2\psi\frac{\partial^2 F}{\partial \gamma^2}\right) = 0. \quad (5)$$

To solve Eq. (5), we can use the double Fourier transform for the variables ξ and γ, whereupon a standard differential equation is obtained for the Fourier transform. This equation is easily integrated, and, in the end, the following result is obtained:

$$F_i = \frac{k_i}{\pi D_i}\exp\left[-\frac{1}{D_i^2}(A_i\xi_i^2 - 2B_i\xi_i\gamma_i + C_i\gamma_i^2)\right],$$

$$A_i = \frac{\chi^2}{2k_i}\left(\psi_i + \frac{1}{2}\sin 2\psi_i\right), \quad B_i = -\frac{\chi^2}{2k_i}\sin^2\psi_i,$$

$$C_i = \frac{\chi^2}{2k_i}\left(\psi_i - \frac{1}{2}\sin 2\psi_i\right), \quad D_i^2 = C_iA_i - B_i^2.$$

For a delta-shaped source, the particle density is

$$n = \frac{k_1k_2n_0\vartheta(s)}{\pi\sqrt{c_1c_2}}\exp\left(-\frac{k_1^2\eta^2}{c_1} - \frac{k_2^2\zeta^2}{c_2}\right),$$

where c_1 and c_2 are the values of the coefficients C_1 and

C_2 for $s' = 0$. These quantities characterize beam broadening due to multiple elastic scattering.

Similarly, we can find the Green's function for the beam in a uniform magnetic field, when the beam axis represents a helical line. In this case, the curvature and torsion of the beam axis are independent of s: $k = |\nu|\sin\theta$, $\kappa = \nu\cos\theta$, where $\nu = -\dfrac{eB_0}{cp_0}$ and θ is the angle between the magnetic-field vector and the direction of the beam injection. For a spiral beam, Eq. (3) has the form

$$\frac{\partial N}{\partial s} + (\alpha + \kappa\zeta)\frac{\partial N}{\partial \eta} + (\beta - \kappa\eta)\frac{\partial N}{\partial \zeta} - k(k\eta + \tau\Gamma)\frac{\partial N}{\partial \alpha} = S + \Lambda N. \quad (6)$$

Here, for eliminating the terms with first derivatives, we should use the following substitution of variables:

$$\xi_1 = (\nu\eta - Q)\cos\psi - (\alpha + \kappa\zeta)\sin\psi + Q - \nu\eta',$$

$$\xi_2 = \mu\nu\zeta + \kappa\left(\eta - \frac{Q}{\nu}\right)\sin\psi + \alpha\frac{\kappa}{\nu}(\cos\psi - 1) - \nu(s - s')R - \nu\zeta',$$

$$\xi_3 = \mu\alpha + \frac{k^2}{\nu^2}[(\nu\eta - Q)\sin\psi + \kappa\zeta(\cos\psi - 1)] + \kappa(s - s')R - \alpha',$$

where the notation

$$\psi = \nu(s - s'), \quad \mu = \frac{k^2 + \kappa^2\cos\psi}{\nu^2},$$

$$Q = \frac{\kappa\beta - k\tau\Gamma}{\nu}, \quad R = \frac{k(k\beta + \kappa\tau\Gamma)}{\nu^2}$$

is introduced.

As a result, Eq. (6) is reduced to a form similar to (5):

$$\frac{\partial N}{\partial s} - \frac{1}{4}\sum_{i,j=1}^{3} a_{ij}\frac{\partial^2 N}{\partial \xi_i \partial \xi_j} = S.$$

For brevity, the expressions for the symmetric matrix of the coefficients a_{ij} are not given. However, they can be easily obtained by performing the above-indicated substitution of variables.

Applying the Fourier-transform method, we can obtain the Green's function:

$$G = \frac{\vartheta(s - s')\nu^2}{2\pi\sqrt{\pi}D}\exp\left(-\frac{1}{D^2}[(A_{22}A_{33} - A_{23}^2)\xi_1^2 + (A_{11}A_{33} - A_{13}^2)\xi_2^2 + (A_{11}A_{22} - A_{12}^2)\xi_3^2 + 2(A_{13}A_{23} - A_{33}A_{12})\xi_1\xi_2 + 2(A_{12}A_{23} - A_{22}A_{13})\xi_1\xi_3 + 2(A_{12}A_{13} - A_{11}A_{23})\xi_2\xi_3]\right).$$

The coefficients used here have the form ($r = s - s'$)

$$A_{ij} = \int_0^r a_{ij}(x)dx,$$

$$D^2 = A_{11}A_{22}A_{33} + 2A_{12}A_{13}A_{23} - A_{11}A_{23}^2 - A_{22}A_{13}^2 - A_{33}A_{12}^2.$$

The practical importance of the results obtained lies in the possibility of estimating the parameters of a beam of fast charged particles penetrating a medium placed in an external magnetic field. The estimates obtained can be applicable in a region where a noticeable thickening of a beam caused by dispersion of particle velocities and multiple elastic scattering still does not occur.

REFERENCES

1. L. R. Kimel' and O. N. Salimov, Zh. Tekh. Fiz. **42**, 1154 (1972) [Sov. Phys. Tech. Phys. **17**, 918 (1972)].
2. N. D. Naumov, Zh. Tekh. Fiz. **62** (2), 178 (1992) [Sov. Phys. Tech. Phys. **37**, 212 (1992)].
3. S. D. Kovalev, A. I. Kuzovlev, and D. B. Rogozkin, Zh. Tekh. Fiz. **63** (6), 37 (1993) [Tech. Phys. **38**, 447 (1993)].
4. A. S. Artamonov and V. A. Gorbunov, Zh. Tekh. Fiz. **50** (8), 1605 (1980) [Sov. Phys. Tech. Phys. **25**, 936 (1980)].
5. V. S. Remizovich and S. N. Taraskin, Zh. Tekh. Fiz. **51** (7), 1356 (1981) [Sov. Phys. Tech. Phys. **26**, 778 (1981)].
6. S. P. Andreev and A. V. Koshelkin, Dokl. Akad. Nauk **289**, 593 (1986) [Sov. Phys. Dokl. **31**, 570 (1986)].
7. S. P. Andreev and A. V. Koshelkin, Zh. Éksp. Teor. Fiz. **92**, 1161 (1987) [Sov. Phys. JETP **65**, 649 (1987)].

Translated by T. Galkina

Doklady Physics, Vol. 46, No. 2, 2001, pp. 72–74. Translated from Doklady Akademii Nauk, Vol. 376, No. 4, 2001, pp. 468–470.

PHYSICS

Spectrum of Magnetoelastic Waves in Axially Anisotropic Ferromagnets

B. I. Sadovnikov*, M. B. Sagdatkireeva, and M. Kh. Harrasov****

Presented by Academician V.P. Maslov April 23, 2000

Received June 22, 2000

Interpretation of spectra of magnetoelastic waves in magnetically ordered materials is still among the most important problems of solid-state physics. The most successful and widely used methods are secondary quantization and Bogolyubov transformation, which provide rich information on spectra of coupled magnetoelastic waves in magnetically ordered materials over wide ranges of temperature and other parameters [1, 2].

Axially anisotropic ferromagnets are of considerable interest because of their domain structure. Study of these ferromagnets have shown that one of the easy-magnetization axes is tilted to the surface normal, which makes it necessary to revise the contributions of magnetostriction and anisotropy in the specimen plane in the physics of magnetic domains. It was shown that these contributions cannot be regarded as mere corrections to anisotropy. The domain structure of axially anisotropic ferromagnets depends on the changes in the tilt angles of the easy-magnetization axes to the surface normal, the temperature, the geometric dimensions of the specimen, and the external stresses. The orientational phase transitions in these materials are also rather specific [3, 4].

Below, we use the method of secondary quantization for studying the coupled magnetoelastic waves in axially anisotropic cubic ferromagnets in the case where the easy-magnetization axes induce anisotropy along various directions in the specimen plane with due regard for the geometric sizes of the specimen.

Consider a Hamiltonian which takes into account the magnetic (H_m), elastic (H_e), and magnetoelastic (H_{me}) energies and determines the spectrum of magnetoelastic waves in an axially anisotropic ferromagnet:

$$H = H_m + H_e + H_{me}.$$

The dependence of the frequency $\omega(\mathbf{k})$ of a magnetoelastic wave on the wave vector $\mathbf{k}$ at various angles ψ of the tilt of the easy-magnetization axis to the surface normal of the specimen is characterized by the "dynamics" illustrated by Fig. 1. It is seen that the tilt angle of the easy-magnetization axis with a value up to $\psi = 10°$ gives rise to an additional resonance in the spectrum of coupled magnetoelastic waves (Fig. 1, $\psi = 10°$). At tilt angles up to $\psi = 15°$, a diffuse spin wave is generated at the nonzero values of the momentum; i.e., there is a region where no coupled magnetoelastic waves can exist (Fig. 1, $\psi = 15°$). This region strongly depends on the tilt angle of the easy-magnetization axis of the axially anisotropic ferroelectric (Fig. 1, $\psi = 15°$, $\psi = 25°$). The dependence of the region without any coupled magnetoelastic waves on the tilt angle can result in complete disappearance of all the magnetoelastic interactions (Fig. 1, $\psi = 45°$). With a further increase of the tilt angle of the easy-magnetization axis to the surface normal, the effect of soft creation (annihilation) of a coupled magnetoelastic wave is observed (Fig. 1, $\psi = 50°$), whereas in the region of large tilt angles, a diffusion spin wave arises (Fig. 1, $\psi = 65°$, $\psi = 80°$). It is also established that the energy of the magnetic subsystem is strongly dependent on the tilt angle of the easy-magnetization axis irrespective of the geometric dimensions of the specimen (Fig. 2). Moreover, the resonance frequency is also strongly dependent on the tilt angle (Fig. 3). In terms of the signal transformation, the above phenomena are very important. Choosing the appropriate magnetic parameters, specimen thickness, and tilt angle, it is possible to arrive at a situation where the coupled spin waves exist

* *Moscow State University, Vorob'evy gory, Moscow, 119899 Russia*

** *Bashkotorstan State University, ul. Frunze 32, Ufa, Bashkotorstan, 450074 Russia*

1028-3358/01/4602-0072$21.00

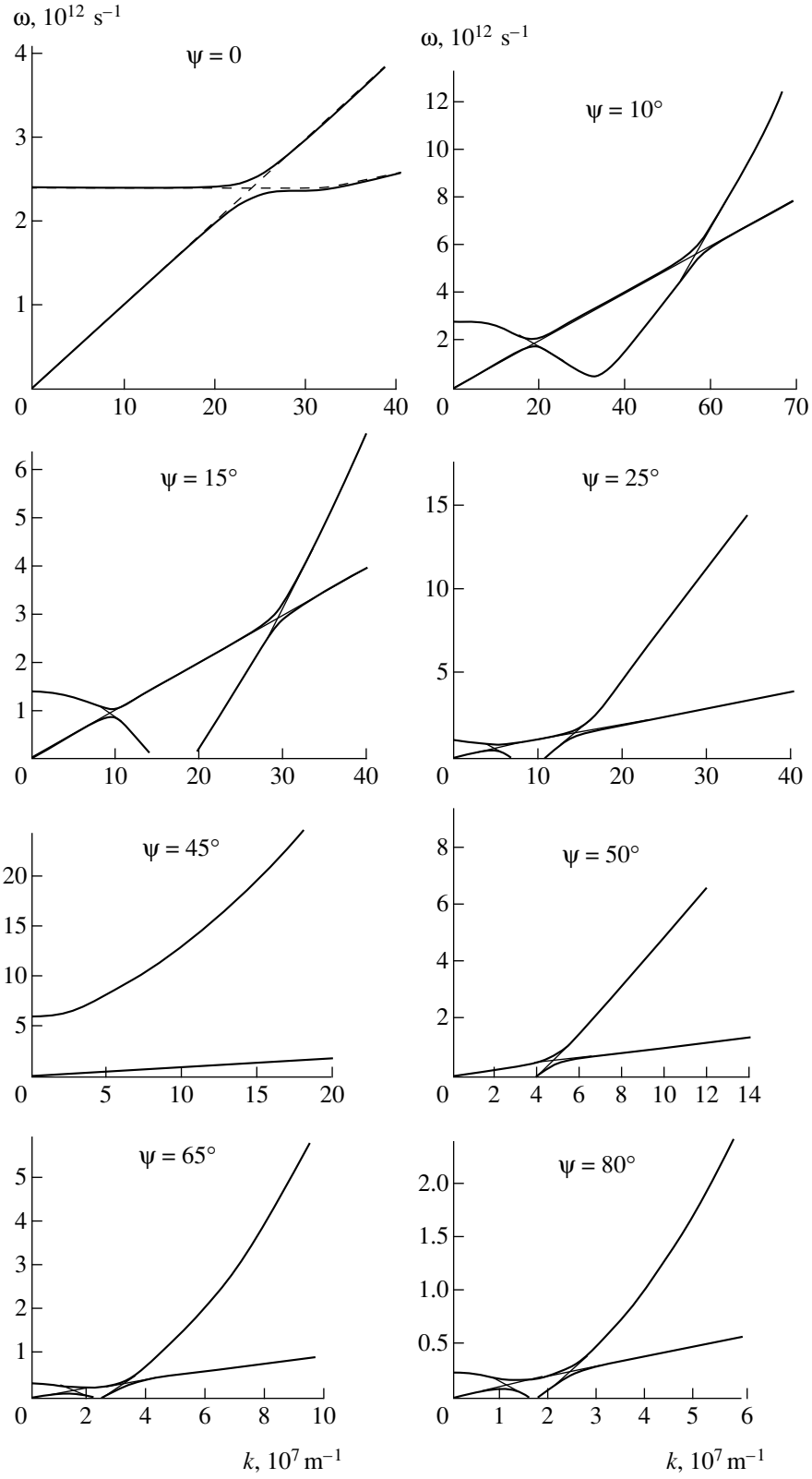

Fig. 1. Spectrum of magnetoelastic waves in an axially anisotropic ferromagnet with the magnetic parameters $K_\psi > 0$, $K_a > 0$, and $\frac{K_a}{K_\psi} = 0.2$ at various tilt angles ψ of the easy-magnetization axis to the surface normal; K_ψ and K_a are the second-order anisotropy constants corresponding to the axial anisotropy and the anisotropy induced in the specimen plane.

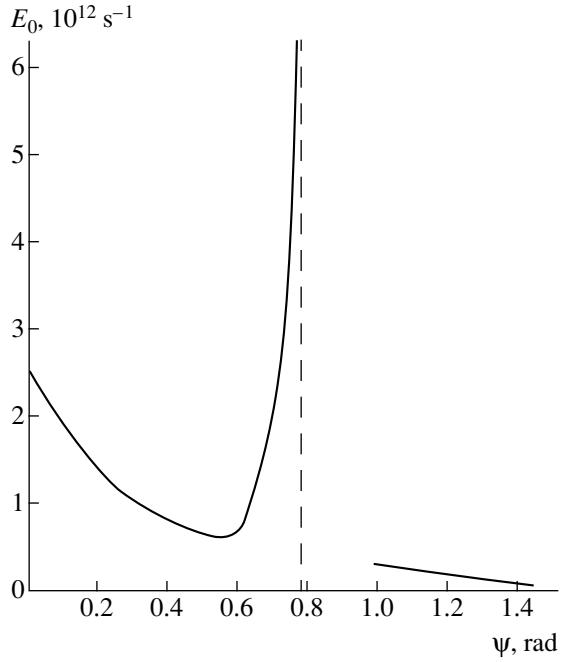

Fig. 2. Energy of the magnetic subsystem as a function of the tilt angle of the easy-magnetization axis to the surface normal.

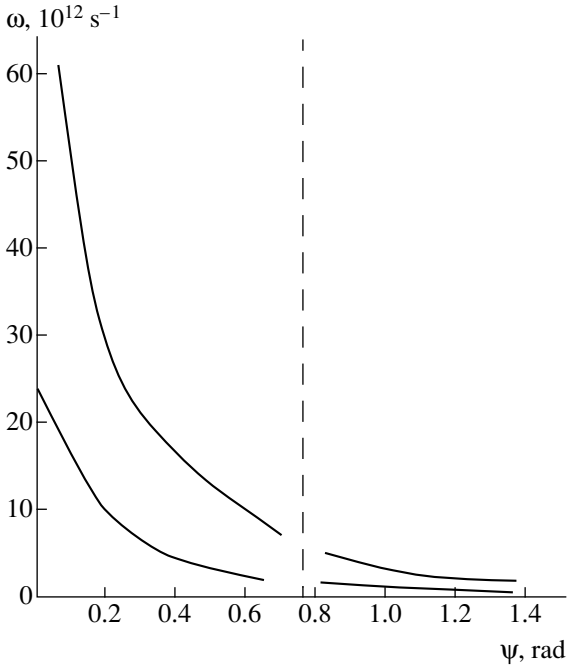

Fig. 3. Resonance frequency of the magnetoelastic interaction as a function of the tilt angle of the easy-magnetization axis to the surface normal.

only in the narrow range of **k** values in the vicinity of the resonance.

REFERENCES

1. N. N. Bogolyubov, Jr., B. I. Sadovnikov, and A. S. Shumovskiĭ, *Mathematical Methods in Statistical Mechanics of Model Systems* (Nauka, Moscow, 1989).
2. B. I. Sadovnikov and M. Kh. Kharrasov, Dokl. Akad. Nauk **339**, 472 (1994) [Phys. Dokl. **39**, 866 (1994)].
3. Kh. Ya. Mulykov, F. Korznikova, M. B. Sagdatkireeva, *et al.*, J. Magn. Magn. Mater. **110**, 73 (1992).
4. A. R. Muhutdinova, M. B. Sagdatkireeva, and M. Kh. Kharrasov, in *Proceedings of the Moscow International Symp. on Magnetism, Moscow, 1999*, Part 2, p. 30.

Translated by L. Man

Doklady Physics, Vol. 46, No. 2, 2001, pp. 75–78. Translated from Doklady Akademii Nauk, Vol. 376, No. 5, 2001, pp. 611–614.

PHYSICS

α–γ-Transition of Aluminum Oxide in Corundum Ceramics under the Action of Neutron Radiation

E. S. Astapova, E. B. Pivchenko, and E. A. Vanina

Presented by Academician V.G. Moiseenko April 11, 2000

Received May 10, 2000

Studies of structural modifications induced by the action of fast neutrons in ceramic insulators are of substantial scientific and practical importance. This is explained by the necessity of conserving the physical properties and strength characteristics of ceramic materials under extreme conditions of nuclear-reactor irradiation [1–3]. Aluminum-oxide ceramics widely used as insulating materials in nuclear-power engineering abruptly lose their mechanical and electric strength (up to 70%) when irradiated by high-fluence fast neutrons. The least modifications (below 14%) are observed in the mullite–corundum ceramics [3, 7, 8]. This paper is devoted to clarifying the mechanisms of these processes at the structural level.

We studied samples of highly alumina ceramics with an Al_2O_3 mass fraction from 76 to 99%, namely, UF-46, 22KhS, and GB-7 ultraporcelains and MK microlite, before and after irradiation by fast neutrons with a fluence of 3.7×10^{21} cm^{-2}. The samples were irradiated in the VÉK-8 channel of a BOR-60 nuclear reactor for 3.5 years (Nuclear Reactor Research Institute, Dimitrovgrad). The neutron-energy range amounted to 0–20 MeV, in which 100- to 300-keV neutrons predominated. The irradiation proceeded at a temperature of 300°C. The sample holding time between completing irradiation and the beginning of investigation was 13 years. For studying structure modifications in the ceramics, methods of X-ray structural diffraction and infrared (IR) spectroscopy were used.

The samples were photographed in a continuous mode and in a point-by-point scanning mode by the Debye–Scherrer method using DRON-3 and DRON-UM1 X-ray diffractometers. The Debye powder patterns were photographed for the copper *K*-series X-rays transmitted through a Ni filter according to the Bragg–Brentano scheme. As a result of photographing the samples, we obtained X-ray diffraction patterns for all the ceramic brands under investigation. From the set of interplane spacings and reflection intensities, the crystalline phases of the ceramics were identified according to the international JCPDS X-ray dosimetry card catalog [9, 10].

The ceramic samples were investigated by methods of IR absorption spectroscopy. The IR spectra were recorded with an IKS-29 spectrophotometer in the range of 400 to 1400 cm^{-1} with an error of 3 cm^{-1}. The samples for the investigations were prepared by pressing of pellets with KBr [5].

The highly alumina ceramics under study belong to the class of materials formed in the $MgO–Al_2O_3–SiO_2$ system. In addition to the basic crystalline α-Al_2O_3 phase, supplementary crystalline phases with a content lower than 5% are present in the ceramics, namely, magnesian spinel in MK; quartz, celsian, and anorthite in UF-46.

After fast-neutron irradiation, the phase composition of the materials was investigated by the method of X-ray dosimetry. After irradiation, the corundum content decreased negligibly in UF-46 and by 10% in GB-7. In microlite, no peaks corresponding to the α-Al_2O_3 phase were found (Fig. 1). After rejection by the harmonic-analysis method of the background and the diffusion components corresponding to the (111) and (220) lines, the crystalline phase arisen after the irradiation was identified as γ-Al_2O_3 according to the JCPDS X-ray dosimetry card catalog (no. 10-425) [10]. The mechanism of the α–γ-transition in the aluminum oxide within the composite material can be inconsistent with the model proposed for pure oxide, which is confirmed by the difference in phase modifications under the action of irradiation in the ceramics with various mass fractions of Al_2O_3.

We investigated IR spectra for UF-46, 22KhS, GB-7, and MK. In Figs. 2 and 3, the IR spectra for GB-7 and microlite in the range of 800 to 5000 cm^{-1} are shown; as is seen, Al_2O_3 is transparent to infrared radiation. A unit cell of γ-Al_2O_3 has a cubic close packing of oxygen atoms and represents a combination of two types of anions, i.e., $(AlO_6)^{9-}$ and $(AlO_4)^{5-}$ (in the crystallographic sense, this is a combination of tetrahedrons and octahedrons with a ratio of 1 : 2). The spatial group

Amur Institute of Integrated Research, Amur Scientific Center, Far East Division, Russian Academy of Sciences, Relochnyĭ per. 1, Blagoveshchensk, 675000 Russia

1028-3358/01/4602-0075$21.00

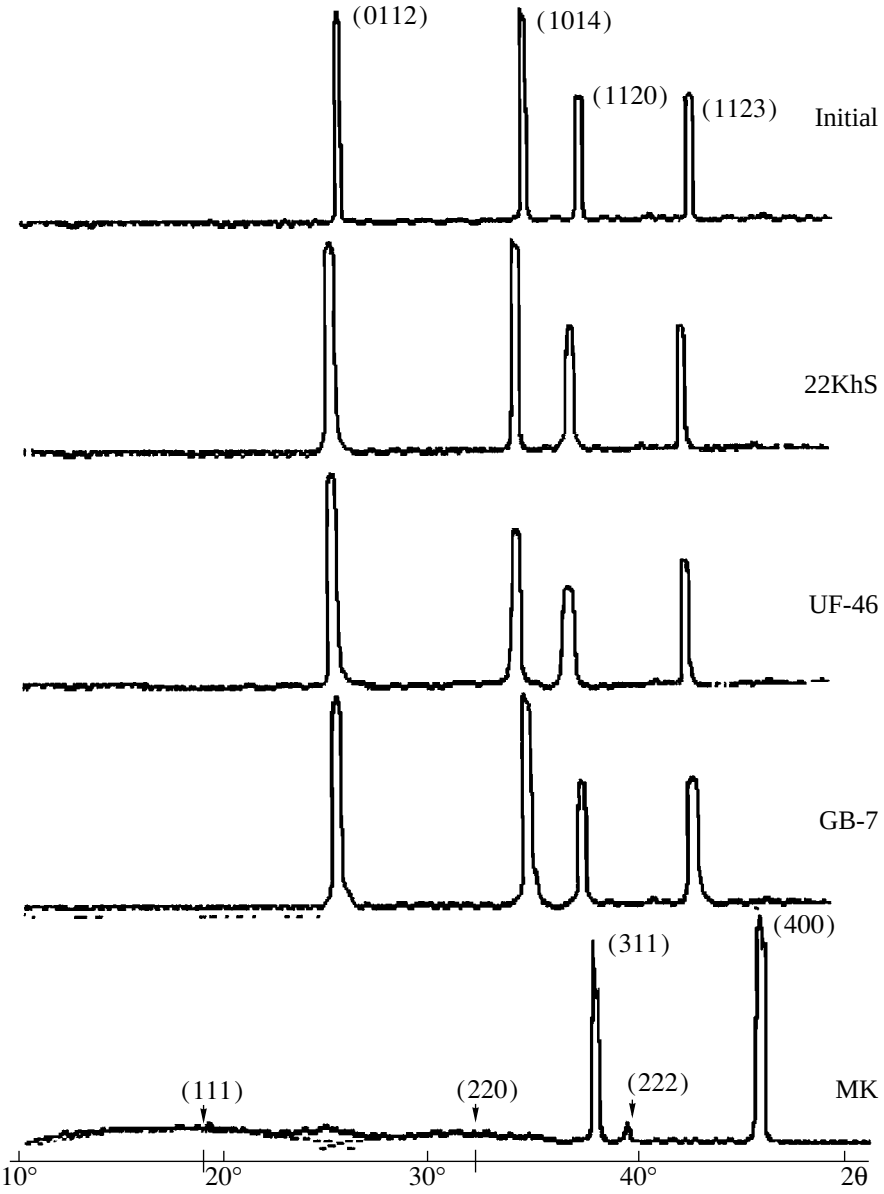

Fig. 1. X-ray diffraction spectra of ceramic materials before (i.e., in the initial state) and after irradiation by fast neutrons.

of this modification corresponds to O_h^7 [4]. Based on the complete vibrational representation of the O_h group and according to the selection rules, two vibrations corresponding to the F_{14} vibrational representation for AlO_6 octahedron and two vibrations corresponding to the F_2 for AlO_4 turn out to be active in the IR spectral range. Thus, the absorption bands corresponding to the triply degenerate F_{14} and F_2 vibrations must occur in the IR spectrum of γ-Al_2O_3. The F_{14} deformation vibration of the δ-AlO_6 octahedron yields a band at 450 cm^{-1}, while the F_{14} valence vibration of the ν-AlO_6 octahedron yields absorption bands at 600 and 635 cm^{-1} [6]. These bands are characteristic of both Al_2O_3 modifications and are present in the spectra of all aluminum-oxide ceramics. The band at 560 cm^{-1} is related to the F_2 deformation vibration of the δ-AlO_4 tetrahedron, while the 720- to 730-cm^{-1} absorption band corresponds to the F_2 valence vibration of the ν-AlO_4 tetrahedron. These bands, which are characteristic of the γ modification, are present only in the spectra of the irradiated MK and GB-7 ceramics; they are much lower in intensity for GB-7 (see Figs. 2 and 3). In the X-ray diffraction spectra of GB-7, no γ-Al_2O_3 peaks are detected, because the content of this phase is lower than 5%.

Thus, the IR-spectroscopy analysis not only confirmed the existence of the α–γ-transition of the aluminum oxide in MK under the action of irradiation, but

also revealed the nucleation of the γ phase in GB-7. In the UF-46 and 22KhS materials, no similar modifications under the action of irradiation were found.

Since the predominant type of radiation defects in these materials are the large-radius dislocation loops [11], it turns out to be possible to introduce transition local temperatures T_t with a characteristic random spread $\delta T_t(R)$, depending on the loop radius. In this case, the nucleation of the γ-phase turns out to be localized in the irradiation thermal spikes and the amount of nuclei does not attain a value detectable by routine methods. However, microlite contains magnesian spinel introduced for hampering the growth of α-Al_2O_3 nuclei. While sintering, it wraps around the corundum grains in thin (down to 1 μm) interlayers. It is necessary to take into account that the γ-Al_2O_3 latent nonstoichiometric synthetic phase has a spinel structure characterized by an imperfection in the cation positions. When forming an Al_2O_3 solid solution in $MgAl_2O_4$ spinel, the cation substitution proceeds according to the scheme

$$3Mg^{2+} \longrightarrow 2Al^{3+} + \square_{Mg},$$

where $\square_{Mg}$ is the vacant site belonging to the magnesium cation [6].

Thus, the γ-phase nuclei arisen in microlite under the action of neutron irradiation are surrounded by spinel, which leads to formation of a substitutional solid solution and the total transition of aluminum oxide into the γ modification in this material. In GB-7, the presence of the glass phase is lower than 9% and the amount of the γ phase formed corresponds to the calculated amorphization of corundum. In UF-46 and 22KhS, the reaction of the glass phase reduces the radiation swelling and amorphization of corundum. In these materials, no formation of the α-phase occurs at all or it is formed in a negligible amount undetectable by these methods. Thus, the abrupt deterioration in the strength characteristics of MK and GB-7 ceramic materials irradiated with fluences above 2.8×10^{21} neutrons cm^{-2} can be explained by the polymorphic transformation of the basic crystalline phase localized in the sites of the dislocation-loop aggregation in GB-7 and by the total transformation in microlite owing to the presence of magnesian spinel in this material. Based on X-ray dosimetry, the full-profile analysis of ceramic insulators in combination with IR spectral analysis makes it possible to predict the α–γ-phase transition of Al_2O_3 under the action of neutron irradiation. From the X-ray-dosimetry data on partial amorphization of corundum with simultaneous appearance of the Al_2O_3 γ-phase nuclei in GB-7 and the comparative analysis of substructure modifications in microlite, it follows that

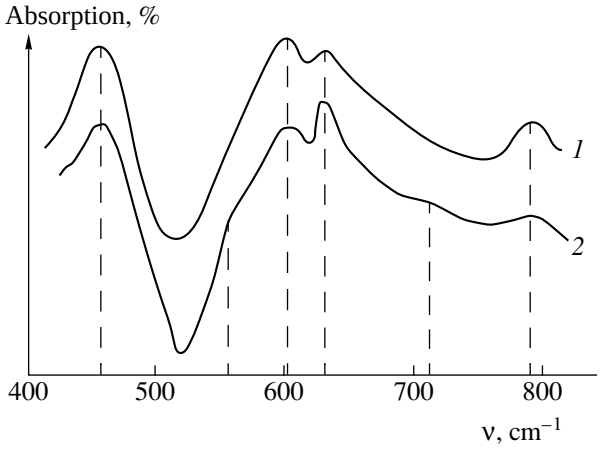

Fig. 2. IR absorption spectra of the GB-7 ceramic material: (*1*) before and (*2*) after irradiation by fast neutrons.

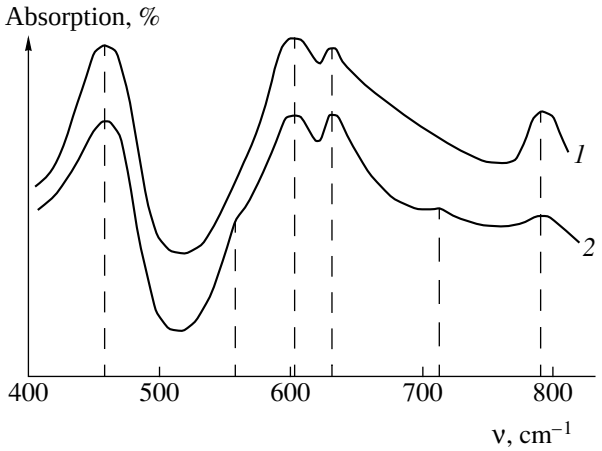

Fig. 3. IR absorption spectra of MK microlite: (*1*) before and (*2*) after irradiation by fast neutrons.

increasing the fluence (above 3.7×10^{21} cm^{-2}) leads to a loss of strength characteristics for GB-7 ceramics.

The results obtained extend the scope of radiation-damage mechanisms in ceramic insulators under the action of fast-neutron irradiation. These data can be used for developing a method of predicting the radiation resistance of ceramic insulators on the basis of structure modifications revealed by X-ray diffractometry and IR spectroscopy.

REFERENCES

1. E. S. Astapova, Fiz. Khim. Obrab. Mater., No. 3, 10 (1997).
2. E. S. Astapova and N. S. Kostyukov, At. Énerg. **78**, 336 (1995).
3. E. S. Astapova, N. S. Kostyukov, and E. B. Pivchenko, Perspekt. Mater., No. 6, 28 (1998).

4. N. V. Belov, A. A. Godovikov, and V. V. Bakanin, *Outlines on Theoretical Mineralogy* (Nauka, Moscow, 1982).
5. E. A. Vanina, E. S. Astapova, and L. N. Ignat'eva, At. Énerg. **81**, 303 (1996).
6. V. S. Gorshkov, V. G. Savel'ev, and N. F. Fedorov, *Physical Chemistry of Silicates and Other High-Melting Compounds* (Vysshaya Shkola, Moscow, 1988).
7. N. S. Kostyukov, N. P. Antonova, *et al.*, *Radiation Materials Science* (Atomizdat, Moscow, 1979).
8. N. S. Kostyukov and E. S. Astapova, J. Adv. Mater. **3**, 292 (1996).
9. D. R. Lundy and E. D. Eans, J. Appl. Crystallogr. **5**, 380 (1972).
10. *Selected Powder Diffraction Data for Minerals* (Joint Committee on Powder Diffraction Standards, New York, 1974).
11. R. S. Wilks, *Radiation Effects in* BeO, Al_2O_3 *and* MgO (Ceramics Division, Atomic Energy Research Establishment, Harwell, Berkshire, 1967).

Translated by V. Bukhanov

Doklady Physics, Vol. 46, No. 2, 2001, pp. 79–84. Translated from Doklady Akademii Nauk, Vol. 376, No. 5, 2001, pp. 615–620.

PHYSICS

A YAG:Nd Laser with a Sagnac Interferometer and a Passive Laser Q-Switch on a LiF:F_2^- Crystal

T. T. Basiev, A. V. Gavrilov*, V. A. Konyushkin**, S. N. Smetanin*, and A. V. Fedin***

Presented by Academician V.V. Osiko May 11, 2000

Received May 31, 2000

INTRODUCTION

The development of high-power solid-state lasers with a high quality of radiation for various technological applications is an important problem in laser physics. One of the most simple but, at the same time, efficient methods of solving this problem is passive Q-switching of a cavity. Indeed, in the early 1980s, it was found [1–3] that applying LiF:F_2^- crystal as a passive laser Q-switch provides generation on the principal mode without using additional selectors. In this case, the spectral width of the mode is inversely proportional to the pulse duration of the modulated radiation. However, the spatial and spectral radiation parameters remain stable only when the pumping level negligibly exceeds the threshold level and the pulse radiation power is no higher than several kilowatts.

Previously, in [4, 5], we showed the possibility of realization of a single-mode modulated radiation with a pulse peak power up to 100 kW and a spatial brightness exceeding 1×10^9 W/(cm^2 sr) with a divergence of 2 mrad and a coherence length of 10 cm. For this purpose, in a master oscillator of a YAG:Nd laser, we used an unstable cavity with a passive laser Q-switch based on a LiF:F_2^- crystal. Multistage amplification of the radiation in the master oscillator allowed us to increase the pulse power and its spatial brightness only by a factor of 2 to 2.5, while the divergence and the coherence length were unchanged [6]. Noticeable improvement of the energy and spatial characteristics was attained in [7, 8] when a coupled cavity of a special geometry was used. The passive laser Q-switch and two active YAG:Nd elements were placed in different arms of this cavity. An initial pulse was formed in the first arm containing the passive laser Q-switch. Then the pulse was amplified with the help of active elements placed in the second arm. This made it possible to increase the peak power of the single-mode radiation up to 500 kW and the spatial brightness up to 3×10^{10} W/(cm^2 sr), with simultaneous reduction of the divergence to 1.6 mrad and extension of the coherence length to 17 cm.

An important advantage of the latter scheme is the substantial reduction of optical and thermal loads on the passive laser Q-switch, whose values are determined by the transmission of a coupling mirror installed between the cavities. However, when employing optically dense passive laser Q-switches (initial transmission $T_0 \le 70\%$), the increase in the pumping energy was accompanied by a reduction in the modulation depth of laser radiation. This is explained by the insufficient radiation intensity needed to obtain the stable antireflection coating of the passive laser Q-switch, by the reflection of a part of the radiation from the end mirror, and by the radiation escape immediately from the second cavity arm. The improvement of the coupling-mirror transmission in order to increase the modulation depth was accompanied by a decrease in the stability of generation pulses, thereby breaking the thermal regime and the increase in thermal loads on the passive laser Q-switch. In addition, increasing the number of active elements in the optical circuit up to three and more reduced the radiation efficiency due to an insufficient compensation of aberrations.

In this study, we have investigated the possibilities of using a Sagnac interferometer as an end reflector for further improving the energy and spatial radiation characteristics of high-power pulse-periodic lasers with passive modulation of the Q-factor.

1. OPTIMIZATION OF THE OPTICAL SCHEME OF A YAG:Nd LASER

To determine the optimum geometry, we investigated two different laser cavities (Fig. 1, schemes 1 and 2) with active elements on the basis of a YAG:Nd crystal with a diameter of 6.3 and a length of 100 mm. In the first scheme (Fig. 1), the two active elements *1* and *2* were placed in a cavity consisting of two Sagnac

* *Kovrov State Academy of Technology, ul. Mayakovskogo 19, Kovrov, Vladimirskaya oblast, 601910 Russia*

** *Scientific Center of Laser Materials and Technologies, Institute of General Physics, Russian Academy of Sciences, ul. Vavilova 38, Moscow, 117942 Russia*

1028-3358/01/4602-0079$21.00

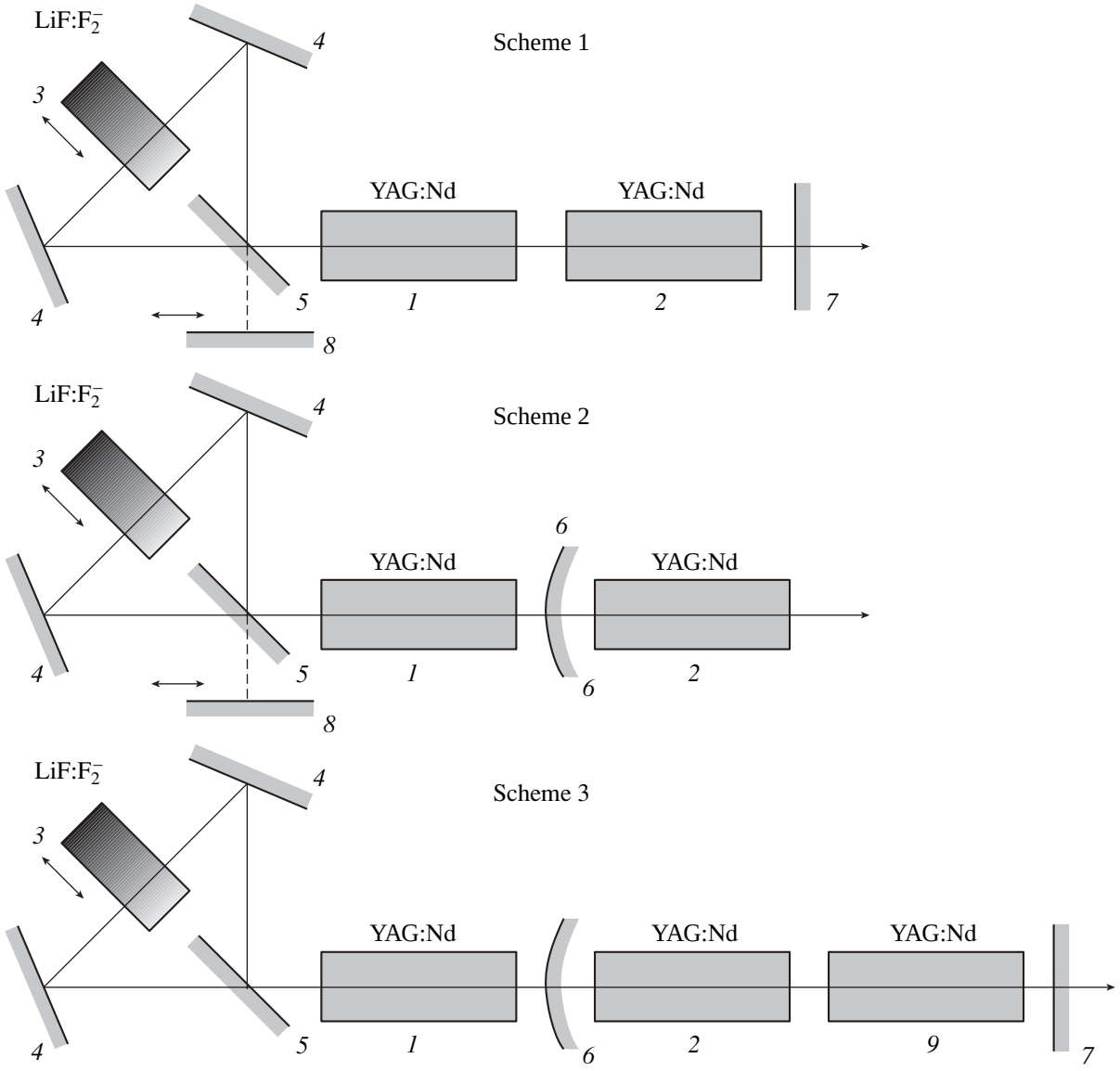

Fig. 1. Optical schemes of lasers based on a LiF: F_2^- crystal with a passive Q-switch: (*1*), (*2*), and (*9*) active elements; (*3*) laser passive Q-switch; (*4*) deflecting mirrors; (*5*) split mirror; (*6*) exit spherical mirror; (*7*) exit plane mirror; (*8*) plane nontransmitting mirror.

interferometers *4* and *5* and an exit plane mirror *7* (mirrors *6* and *8* were absent). In the second scheme (Fig. 1), a single active element *1*, a Sagnac interferometer, and a convex mirror *6* with a curvature radius of 750 mm form a master oscillator (mirrors *7* and *8* are absent). The second active element was used as a single-pass amplifier. The totally reflecting mirror was applied in both laser schemes to evaluate the effect of open output of the Sagnac interferometer on radiation parameters. The optical pumping was performed by KDNP-6/90A krypton lamps connected to a GND-13 power supply unit (the pulse pumping energy attained 85 J for each lamp, the pulse-repetition frequency was between 1 and 30 Hz with a pulse duration of 200 μs).

Passive Q-switching was performed with the help of a LiF: F_2^- crystal (*3*) with dimensions of $8 \times 17 \times 66$ mm. The crystal had a variable transmission changing linearly from 20 to 80% perpendicular to the laser optical axis. The optimum position of the passive laser Q-switch was evaluated through the generation efficiency and the thermal state of the crystal in its position both inside the cavity and in the Sagnac interferometer. It was established that the position of the passive laser Q-switch in the diagonal of the Sagnac interferometer is the most reasonable. In this case, the energy parameters of the radiation are higher by a factor of 1.3, while the thermal and optical loads on the passive laser Q-switch are significantly lower compared to those cor-

responding to its location inside the cavity. Indeed, when the passive laser Q-switch is positioned near the active element, the radiation propagating in the direct and opposite directions from the active element to the end reflector passes through the LiF crystal twice. This results in an increase in the energy loss in the medium of the passive laser Q-switch, thus elevating the thermal and radiant loads and decreasing the generation efficiency. Extension of the LiF:F_2^- crystal length to 40 mm did not provide stabilization of the thermal regime without forced cooling. It is worth noting that in the linear scheme [7], the radiation also executes no less than two passes through the passive laser Q-switch before escaping the cavity passive arm.

In the case of positioning the passive laser Q-switch in the interferometer, the radiation comes back again to the active element, passing by the LiF crystal only once. This fact decreases the energy loss on the nonreflecting faces of the passive laser Q-switch and the residual energy loss in the LiF: F_2^- crystal. Since the latter are mainly determined by the radiation absorption and scattering on inactive centers and depend on the quality of crystal manufacturing, the coefficient of the residual loss can be evaluated by the formula $\alpha = k_p l = k_a l/\beta$, where k_p and k_a are the coefficients of the inactive (passive) and active loss, respectively; l is the crystal length; and $\beta = k_a/k_p$ is the contrast characterizing the quality of the crystal. The values of k_p and k_a were determined according to the transmission spectrum of the LiF: F_2^- crystal. In this case, the value of β was independent of T_0 and equaled $\beta = 27$. For $T_0 = 52$ % ($k_a = 0.39$ cm^{-1}), the coefficient of residual loss was $\alpha = 0.025$, whereas for $T_0 = 32\%$ ($k_a = 0.67$ cm^{-1}), this coefficient increased up to $\alpha = 0.042$. Hence, with allowance for reflections from the faces of the LiF: F_2^- crystal (up to 5%), 7 to 10% of the energy can be lost only for a single pass through the passive laser Q-switch. Since the amount of the loss per single pass affects not only the rate of generation development but also the number of radiation passes through the cavity, the decrease in the effect of the residual loss in the case of using the Sagnac interferometer as an end reflector makes it possible to noticeably increase the efficiency of laser generation.

For both schemes 1 and 2 (Fig. 1), the optimum exit-mirror transmission was determined in terms of the mean and peak powers of the modulated radiation. The pumping-pulse energy was 84.4 J for each lamp, and the initial transmission of the passive laser Q-switch was ~58%. The results obtained showed that the optimum value of the exit-mirror transmission was 85–90% both with the additional mirror *8* and without it. In schemes 1 and 2 with open output (without the additional mirror *8*), the average radiation power turned out to be the same and attained 69 W. However, when using scheme 2 (the master oscillator with a single-pass amplifier), we obtained maximum values of 1.15 MW for the peak power and an energy of 57.5 mJ for the radiation pulses. This is, apparently, associated with the shorter length of the cavity and, as a consequence, the lesser time of passing by it [9]. This fact is confirmed by reducing the duration of generation pulses from 65 ns (scheme 1) to 45 ns (scheme 2). In addition, scheme 2 is more profitable from the standpoint of lower radiant loads on the passive laser Q-switch. This is explained by the fact that the radiation of the only single active element is practically absorbed.

Introducing a totally reflecting mirror at the open output of the Sagnac interferometer made it impossible to noticeably increase the average radiation power. For example, in scheme 2 with additional mirror *8*, the average radiation power increased only up to 72 W, i.e., by 5%. Moreover, the parameters of certain pulses of the modulated radiation appreciably deteriorated. The instabilities of the amplitude, duration, and pulse-repetition period increased from 5 to 10–15%. The number of pulses in a train increased from 40 to 49, and their energy and peak power even decreased to 49 mJ and 1 MW, respectively. In the profile of the radiation-intensity distribution, we observed chaotically arising local inhomogeneities. This testifies to a multimode character of generation. Therefore, application of an additional mirror in the linear laser scheme with the Sagnac interferometer can hardly be reasonable.

It should be noted that for a scheme with a linear triple-mirror cavity [7], the radiant loss was optimum when the exit-mirror transmission was 47%. The initial transmission of the passive laser Q-switch was 58%. From our results obtained for schemes 1 and 2 (Fig. 1), we can conclude that application of the Sagnac interferometer makes it possible to increase the cavity *Q*-factor and, as a consequence, the energy parameters of laser radiation for close values of the initial transmission of the passive laser Q-switch. To the greatest extent, this advantage becomes apparent in scheme 2 (Fig. 1), where the passive laser Q-switch is placed in the diagonal of the Sagnac interferometer. This assumption agrees well with the results of a test experiment in which the LiF: F_2^- with an initial transmission $T_0 = 53\%$ was placed inside the cavity in front of the Sagnac interferometer. In this case, the average radiation power decreased by a factor of 1.3 and attained 52 W.

The results of investigation of the dependences of laser energy and time parameters for scheme 2 (additional mirror *8* was absent) on the initial transmission of the passive laser Q-switch and the energy of pumping pulses are presented in Figs. 2 and 3.

Figure 2 shows the dependences of the energy (Fig. 2a) and time (Fig. 2b) radiation parameters on the initial transmission of the passive laser Q-switch for a pumping-pulse energy of 84.4 J and pulse-repetition interval of 30 Hz. As is seen from the results obtained, the maximum average power P = 74 W (Fig. 2a,

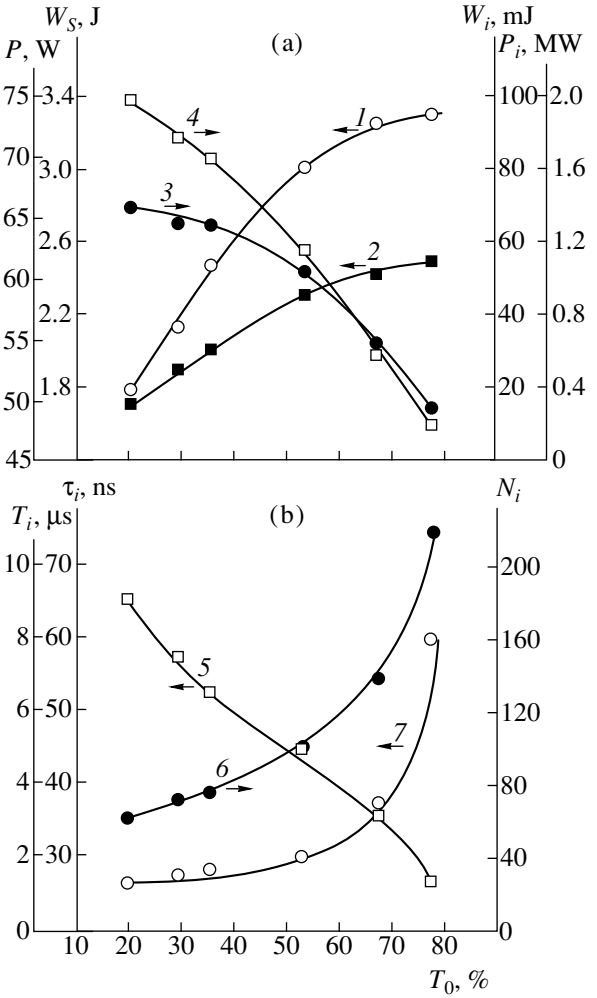

Fig. 2. Dependences of (a) energy parameters and (b) time parameters of laser radiation for scheme 2 on the initial transmission of the laser passive Q-switch on the LiF: F_2^- crystal: (*1*) the average power; (*2*) the energy of the pulse train; (*3*) individual-pulse energy in a train; (*4*) peak power; (*5*) repetition period; (*6*) pulse duration; (*7*) number of pulses in a train.

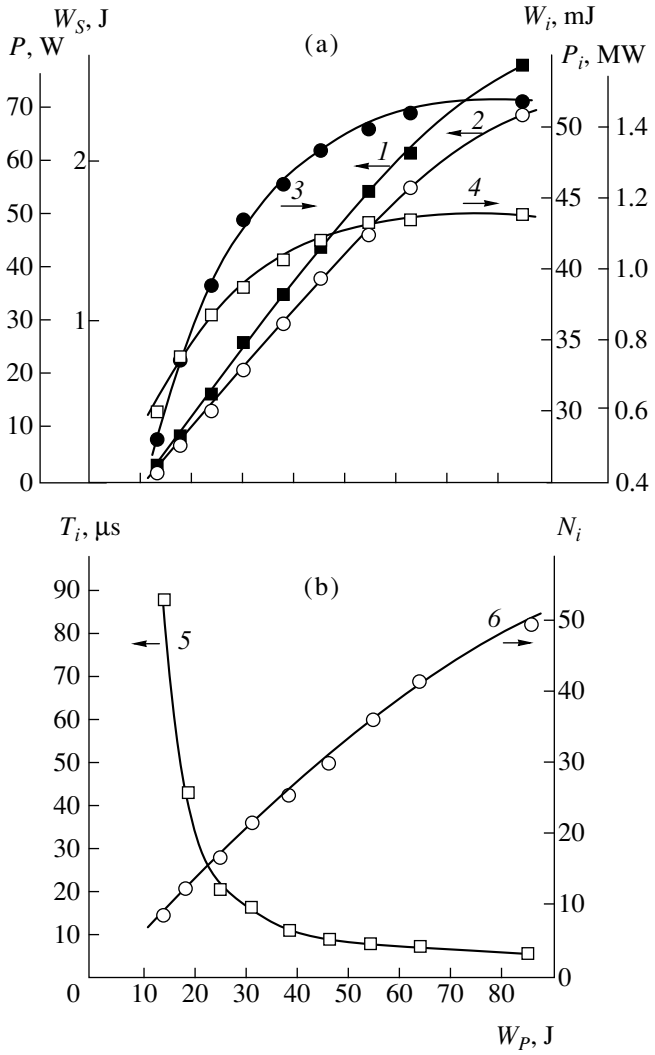

Fig. 3. Dependences of (a) energy parameters and (b) time parameters of laser radiation for scheme 2 on the energy of pumping pulses at an initial LiF: F_2^--crystal transmission of 53%: (*1*)–(*5*) the same as in Fig. 2; (*6*) number of pulses in a train.

curve *1*) and the maximum pulse-train energy W_S = 2.45 J (Fig. 2a, curve *2*) for modulated radiation are attained in the case of the initial transmission of the LiF: F_2^- crystal, T_0 = 78%. The energy of an individual pulse is W_i = 15 mJ (Fig. 2a, curve *3*) and its peak power is P_i = 200 kW. The decrease in the initial transmission of the passive laser Q-switch from 78 to 20% due to an increase in the threshold value of the inverse population and time needed to attain this value at a constant pumping rate leads to increasing the pulse-repetition period T_i in the train from 1.4 to 9.1 μs (Fig. 2b, curve *5*), decreasing the number N_i of pulses from 160 to 22 (Fig. 2b, curve *7*) and the duration τ_i from 80 to 35 ns (Fig. 2b, curve *6*). As a result, the decrease in the initial transmission of the passive laser Q-switch is responsible for the sharp increase in the energy of an individual pulse in the train and its power. For T_0 = 20%, these values are equal to 70 mJ and 2 MW, respectively. However, in this case, the average radiation power and the energy of the pulse train are lowered approximately by a factor of 1.4, i.e., to 50 W and 1.7 J, respectively.

Figure 3 demonstrates the dependences of the energy parameters (Fig. 3a) and time parameters (Fig. 3b) for laser radiation on the energy of pumping pulses for a 30-Hz repetition frequency and for an initial transmission of 53% for the passive laser Q-switch. It is seen that the increase in the energy W_P of pumping pulses is accompanied by a lowering of the time of attainment of the threshold inverse population and, as a consequence, the period T_i of pulse repetition in the train (Fig. 3b, curve *5*). This results in an increase not

only in the number of pulses N_i (Fig. 3b, curve *6*) but also in the average power P (Fig 3a, curve *1*) and in the energy of the pulse train W_S (Fig. 3a, curve *2*). The energy of an individual pulse in the train W_i (Fig. 3a, curve *3*) and its power P_i (Fig. 3a, curve *4*) increase also, which may be caused by the rise in the volume of an active medium taking part in the generation. However, in the range of pumping energy between 50 and 84.4 J, their rise slows down. This indicates that the use of the energy stored in the active element under pumping is close to maximum. This is also confirmed by the existence of the optimum value W_P = 54 J for which the maximum generation efficiency η = 1.42% is attained. The significant increase in the energy parameters of the single-mode radiation may be expected in a YAG:Nd laser with a coupled cavity involving a Sagnac interferometer in one of the arms.

2. A YAG:Nd LASER WITH AN OPTICALLY COUPLED RESONATOR AND SAGNAC INTERFEROMETER

The optical scheme of this laser is given in Fig. 1 (scheme 3). In contrast to scheme 2, we used a two-stage amplifier (active elements *2* and *9*) and an additional transmitting mirror *7* placed after the output amplification stage. To improve the compensation of the thermal lens in the active element *1* of the master oscillator, we applied a convex mirror *6* with a curvature radius of 750 mm. Its position in the cavity was chosen from the condition of correspondence between the diameters of both the zeroth mode and the active element. The optimum transmission of mirrors *6* and *7* (85 and 93%, respectively) was determined from the maximum generation efficiency.

The investigation of the radiation energy parameters and time parameters for the YAG:Nd laser system with the Sagnac interferometer as functions of the initial transmission of the passive laser Q-switch demonstrated that the character of these dependences is similar to those for scheme 2 (Fig. 2). It is worth noting that pulse durations in a train coincide for both schemes within the experimental errors. Whence, it follows that the optically coupled cavity with an additional stage of amplification practically does not affect the development of generation in the master oscillator but performs only multipass amplification of the radiation generated by this oscillator, which was not obtained in linear multimirror resonators [8, 9]. As in scheme 2, the maximum generation efficiency for the laser system is attained for the pumping-pulse energy W_P = 54 J. However, application of two-stage amplification made it possible to increase not only the radiation energy parameters, namely, the averaged power, the train energy, the energy of an individual pulse, and the peak power, but also the laser efficiency that attained η = 1.62%.

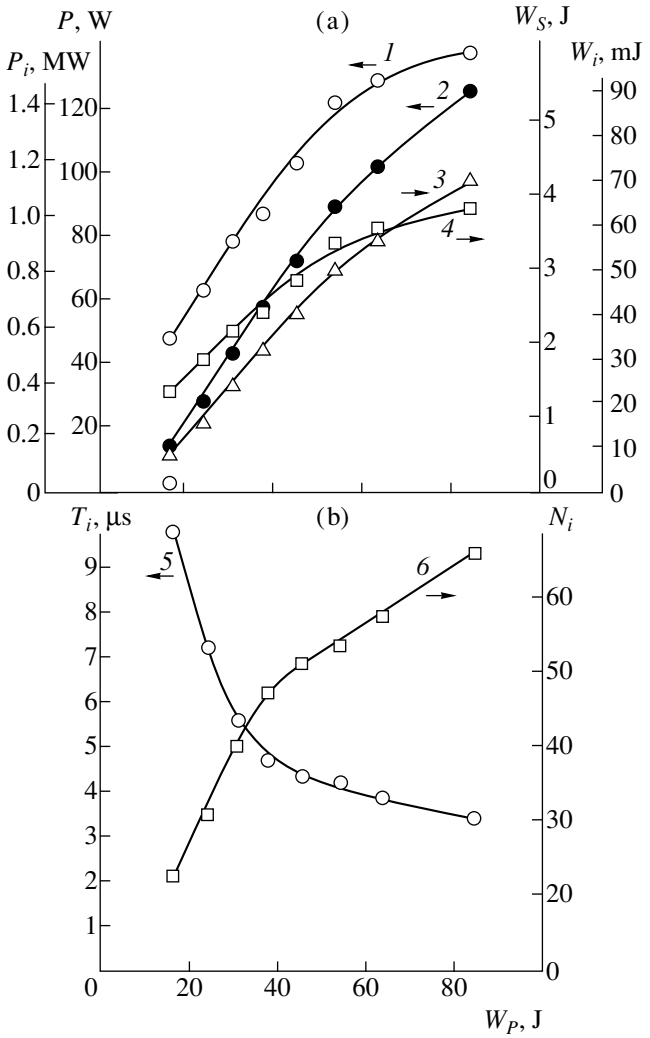

Fig. 4. Dependences of (a) energy parameters and (b) time parameters of laser radiation for scheme 3 on the energy of pumping pulses at an initial LiF:F_2^--crystal transmission of 53%: (*1*) peak power; (*2*) average power; (*3*) energy of a pulse train; (*4*) energy of an individual pulse in a train; (*5*) repetition period; (*6*) number of pulses in a train.

In Fig. 4, the dependences of the radiation energy characteristics (Fig. 4a) and time characteristics (Fig. 4b) of the YAG:Nd-laser on the energy of pumping pulses for a pulse-repetition frequency of 30 Hz are given. The position of the gradient dyeing passive laser Q-switch corresponded to the initial transmission T_0 = 53%. The dependences obtained show that compared with scheme 2 (see Fig. 3), the additional amplification provides the possibility of increasing the radiation energy parameters by a factor of 1.5–2, namely, the averaged power P from 70 to 123 W (Fig. 4a, curve *2*), the train energy W_S from 2.3 to 4.1 J (Fig. 4a, curve *3*), the energy W_i of an individual pulse from 54 to 69 mJ (Fig. 4a, curve *4*), and the radiation power P_i from 1.15 to 1.6 MW (Fig. 4a, curve *1*). The absence of the saturation for the rise of the energy parameters and the

weak effect of the amplification stages on the time characteristics (Fig. 4b, curves *5* and *6*) indicate the possibility of further elevating the generation efficiency in the case of a larger number of amplification stages.

The divergence of laser radiation determined by the relative distribution of intensity in the focal plane of the lens with a focal distance of 1 m was $\theta/2 = 1.1$ mrad at the level of e^{-2} with respect to the maximum intensity. This corresponds to the quality parameter $M^2 = 8.1$. For the maximum pumping energy and the initial transmission $T_0 = 20\%$ of the LiF:F_2^- crystal, the spatial radiation brightness was as high as 2.2×10^{12} W/(cm^2 sr). The coherence length measured with the help of a Michelson interferometer was 30 cm.

CONCLUSIONS

The data presented testify to the high generation efficiency of the laser system with a Sagnac interferometer and a passive Q-switch on the LiF:F_2^- crystal. Application of the Sagnac interferometer as an end reflector made it possible not only to decrease the energy loss in the cavity but also to increase the energy radiation parameters by a factor of 2 to 4 and the coherence length by a factor of 1.5 to 2, to elevate by more than one order of magnitude the radiation spatial brightness, as well as to raise the efficiency of laser generation.

In our opinion, this improvement of the radiation energy parameters and space parameters is caused by the spatial spectral and angular selectivity of the Sagnac interferometer, which arises while introducing the LiF:F_2^- crystal into its ring. In addition, the Sagnac interferometer modified by this manner is efficiently compensated through the self-collimating of the thermal lens induced under the action of pumping in the active element of the master oscillator. Furthermore, due to the interference, the Sagnac interferometer attenuates an irregularity in the phase incursion over the cross section of radiation reflected from it which retains the cavity *Q*-factor close to the initial value. Finally, the feasibility of controlling the radiation parameters by smooth changing of the optical density of LiF:F_2^- crystals with varying the transmission makes it possible to design flexible laser systems. These systems may be easily automated and involved in various technological processes.

REFERENCES

1. Yu. L. Gusev, A. V. Kirpichnikov, V. I. Lisitsyn, *et al.*, Kvant. Élektron. (Moscow) **8**, 1141 (1981).
2. T. T. Basiev, B. I. Denker, N. N. Il'ichev, *et al.*, Kvant. Élektron. (Moscow) **9**, 1536 (1982).
3. B. I. Denker, N. N. Il'ichev, A. A. Malyutin, *et al.*, Kvant. Élektron. (Moscow) **9**, 1842 (1982).
4. T. T. Basiev, A. N. Kravets, S. B. Mirov, and A. V. Fedin, USSR Patent No. 1799526, MKI N 01 S 3/11 (1992).
5. T. T. Basiev, A. N. Kravets, S. B. Mirov, and A. V. Fedin, Pis'ma Zh. Tekh. Fiz. **17** (9), 16 (1991) [Sov. Tech. Phys. Lett. **17**, 320 (1991)].
6. T. T. Basiev, A. N. Kravets, S. B. Mirov, and A. V. Fedin, Kvant. Élektron. (Moscow) **18**, 822 (1991).
7. T. T. Basiev, A. N. Kravets, and A. V. Fedin, RF Patent No. 2038666, MKI N 01 S 3/11 (1995).
8. T. T. Basiev, A. N. Kravets, and A. V. Fedin, Kvant. Élektron. (Moscow) **20**, 594 (1993).
9. T. T. Basiev, A. N. Kravets, and A. V. Fedin, Preprint No. 1, Inst. Obshcheĭ Fiziki RAN (General Physics Institute, Russian Academy of Sciences, Moscow, 1993).

Translated by Yu. Vishnyakov

Doklady Physics, Vol. 46, No. 2, 2001, pp. 85–87. Translated from Doklady Akademii Nauk, Vol. 376, No. 5, 2001, pp. 621–623.

PHYSICS

Structural Features of the Avalanche Multiplication in Field-Effect Heterotransistors

V. A. Gergel', Corresponding Member of the RAS V. G. Mokerov, Yu. V. Fedorov, and M. V. Timofeev

Received July 13, 2000

As is well known [1], the key advantage of field-effect transistors is the presence of a current-saturation region in their current–voltage characteristics. According to the classical model [2], the onset of the saturation region corresponds to the drain voltage $V_D' = V_G - V_t$ (where V_G is the gate voltage and V_t is the so-called threshold voltage) and extends to $V_D'' = V_B$, i.e., to the voltage corresponding to the onset of impact ionization. It is also well known that the saturation region is associated with a specific propagation of the drain voltage along the device structure. Indeed, the voltage drop along the channel length attains $V_G - V_t$ and corresponds to the almost complete depletion of the channel near-drain part. In this case, the relevant excess equal to $V_D - V_G + V_t$ is associated with a relatively narrow region of the space charge near the channel-drain boundary. This is the region of localization of the impact-ionization avalanche process occurring at a sufficient magnitude of this excess.

As a rule, in the practice of field-effect transistor design, the tendency exists to increase the breakdown voltage (in order to enhance the output power). Below, we show that in the field-effect heterostructure transistors, an additional feasibility appears for elevating the breakdown voltages compared to the field-effect devices of conventional (Schottky-transistor and MIS) realizations. It is evident that this feasibility is caused by the presence of two dissimilar semiconductor layers, namely, wide-gap and narrow-gap ones, in the transistor active region. The essence of the structural features of the ionization process in the heterostructure under study is easy to elucidate with the help of the electric-field pattern in the device near-drain region shown in Fig. 1. The equipotential lines shown in the figure demonstrate, first, the existence of the bulk channel in the transistor subgate wide-gap layer. Second, this is the most essential point, the field lines perpendicular to the equipotential lines and forming, with allowance for the energy jump, trajectories of the electron drift at the heteroboundary are decomposed into two classes. One of their parts (outgoing from the bulk channel directly into the GaAs–n^+ drain-electrode) is placed completely in the wide-gap layer and, consequently, is characterized by a considerably high threshold of impact ionization. At the same time, the other part (outgoing from the surface channel at the heteroboundary) is almost completely localized in the narrow-gap layer with a low ionization threshold.

We now try to complete the qualitative pattern of the phenomenon under consideration, complementing this pattern with the necessary quantitative estimates. At the source boundary, the cold electrons are injected into the surface 2DE-channel, since the bulk channel is separated from the source by an energy barrier. Then, drifting in a strong electric field, the electrons in the surface channel are heated and partially or almost completely pass into a bulk wide-gap channel, overcoming the corresponding energy barrier $\Delta = 0.1$–0.3 eV at the heteroboundary. Moving already in the bulk channel, these electrons are cooled while penetrating the heterobarrier. Then, they traverse the region of possible avalanche multiplication in the near-drain space-charge region without escaping from the wide-gap layer, in which the impact-ionization threshold is rather high. In turn, the electrons that failed to appropriately overcome the energy barrier of the heteroboundary are involved in narrow-gap trajectories of the near-drain space-charge region. There, the process of avalanche multiplication

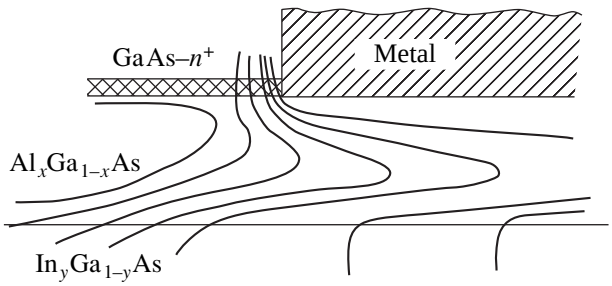

Fig. 1. Qualitative field pattern in the channel of a heterotransistor with modulation doping.

Institute of Radio Engineering and Electronics, Russian Academy of Sciences, ul. Mokhovaya 11, Moscow, 103907 Russia

1028-3358/01/4602-0085$21.00

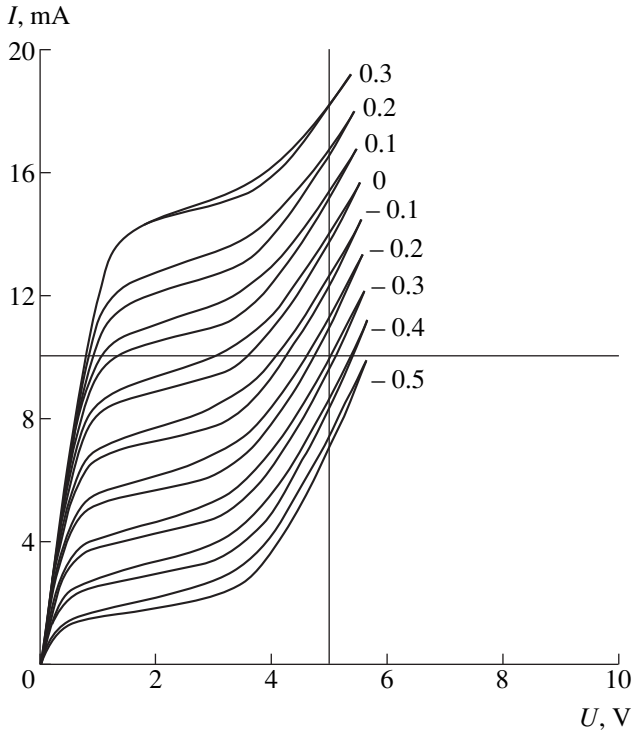

Fig. 2. Current–voltage characteristic for a transistor with a high heterobarrier $\Delta = 0.27$ eV.

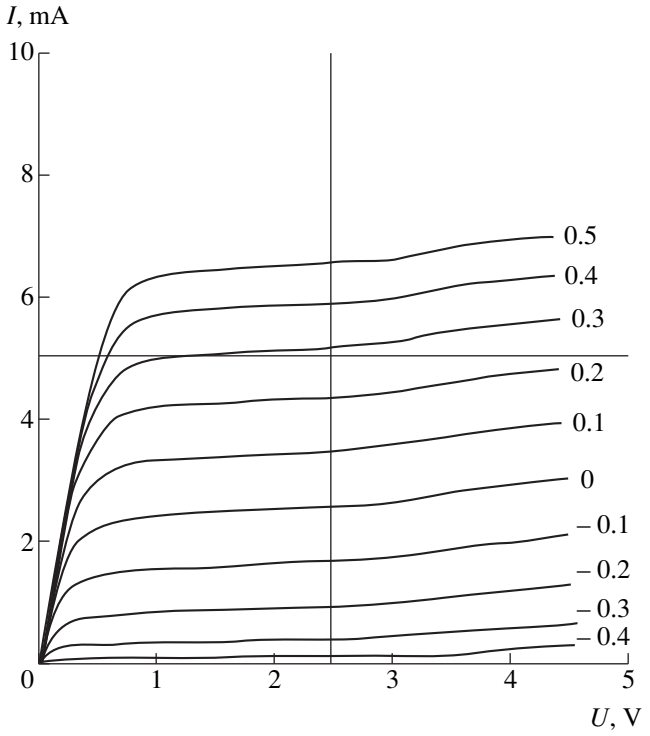

Fig. 3. Current–voltage characteristic for a transistor with a low heterobarrier $\Delta = 0.17$ eV.

develops at voltages considerably lower than those needed for avalanche breakdown along the wide-gap trajectories to be developed.

Consequently, in order to enhance the electric strength of a transistor, we should provide specific conditions for high-field heating charge carriers in the channel and properly choose the energy barrier for the heteroboundary when almost the entire electron flow has time to hop within the channel length from the surface channel to the bulk one. For the corresponding quantitative estimate, we use the simplest formula of a so-called thermoionic emission [3], roughly assuming it to be homogeneous along the channel length. This yields for the branching flow,

$$\Delta I = \frac{v_T}{4} L Q \frac{E_\perp}{T} \exp\left[-\frac{\Delta}{T}\right],$$

where v_T is the mean thermal velocity; T is the mean electron temperature; and Q is the surface electron density, depending on the boundary value of the bulk electron concentration n_S according to the well-known quasi-classical relation $n_S = Q\frac{E_\perp}{T}$; L is the channel length and $E_\perp = \frac{Q}{\varepsilon\varepsilon_0}$. To estimate the electron temperature, we employ the result of the ultraquasi-hydrodynamic drift model [4] proposed by us previously. According to this model,

$$T = \frac{1}{2}T_{\max} = \frac{1}{5}(V_G - V_t).$$

In turn, the current of the transistor-surface channel can be represented as a product of the surface charge by the mean drift velocity $I = v_D Q$. Combining this expression with the formula given in [1], it is easy to understand that the situations of interest, i.e., $I - \Delta I \ll I$ and $\Delta I \ll I$, are provided by the fulfillment of either of two inequalities:

$$\frac{5\Delta}{V - V_t} \gtrless \lambda n\left(\frac{L}{d}\frac{v_T}{v_D}\right).$$

Here, d is the thickness of the wide-gap layer, which appears here since $E_\perp = \frac{V_G - V_t}{d}$. Taking into account that the typical values of the relevant quantities are $V_G - V_t = 0.5$ V, $\frac{L}{d} \simeq 10$, and $\frac{v_T}{v_D} \geq 3$, we see that in the variation range of $0.1 < \Delta < 0.4$ eV, the realization of each situation is possible. The estimate given (rough but fairly reliable) indicates a quite realistic practical

possibility of elevating the transistor breakdown voltage by a corresponding optimization of the composition of the transistor wide-gap layer.

To confirm the considerations given above concerning the features of avalanche breakdown in heterotransistors, the families of current–voltage characteristics for two tested $Al_xGa_{1-x}As$–$In_yGa_{1-y}As$ *P*–HEMTs with similar parameters, except the composition x of the wide-gap layer, are shown in Figs. 2 and 3. In the first of them, the aluminum fraction was 0.27, which corresponds to the value $\Delta = 0.27$. In the second case, $x = 0.2$ and $\Delta = 0.17$. It is also evident that the overly large (from our point of view) molar fraction of aluminum and, correspondingly, barrier height Δ resulted in significant degradation of the characteristics of the first transistor.

REFERENCES

1. W. Shockley, Proc. IRE **40**, 1365 (1952).
2. S. Sze, in *Physics of Semiconductor Devices* (Wiley, New York, 1981; Mir, Moscow, 1986), Vol. 1.
3. G. E. Pikus, *Theoretical Principles of Semiconductor Devices* (Nauka, Moscow, 1965).
4. V. A. Gergel', V. G. Mokerov, M. V. Timofeev, and Yu. V. Fedorov, Fiz. Tekh. Poluprovodn. (St. Petersburg) **34**, 239 (2000) [Semiconductors **34**, 233 (2000)].

Translated by T. Galkina

Doklady Physics, Vol. 46, No. 2, 2001, pp. 88–91. Translated from Doklady Akademii Nauk, Vol. 376, No. 6, 2001, pp. 749–752.

PHYSICS

Effect of Misorientation Angle on the Photoluminescence Spectra of Si (δ)-Doped GaAs (111)A Layers Grown by Molecular Beam Epitaxy

G. B. Galiev, Corresponding Member of the RAS **V. G. Mokerov, and Yu. V. Khabarov**

Received August 9, 2000

In recent years, there has been considerable interest in epitaxial films grown on unusual vicinal faces of GaAs such as (11$\bar{1}$), (211), (311) etc. with a certain misorientation because of specific physical properties and novel possibilities for their application in various devices. Thus, it was shown [1] that a 1°–4°-misorientation of GaAs (111)A substrates in the [211] direction results in formation of a vicinal surface consisting of terraces formed by (111)A planes and steps formed by (111)B planes. In the [$2\bar{1}\bar{1}$]-direction, such misorientation gives rise to terraces formed by (111)A planes and steps formed by (100) planes [2]. Considerable interest is also expressed in the unusual behavior of the silicon dopant in (111) GaAs layers [in comparison with the (100) orientation]. Unlike (100) GaAs, where silicon located in the sites of Ga sublattice behaves mainly as a donor, in the (111)A layers grown by molecular beam epitaxy (MBE), one can obtain both strongly compensated semi-insulating layers or layers with *n*- or *p*-type conductivity, depending on the growth temperature T_g and ratio $\gamma = P_{As}/P_{Ga}$ of arsenic (P_{As}) and gallium (P_{Ga}) fluxes [2–5].

Of special interest is the so-called growth of planar or δ-doped layers, which provide the formation of extremely narrow quantum-size doping regions. However, as far as we know, no studies of the effect of GaAs (111)A misorientation on the process of δ-doping upon simultaneous variation of the γ ratio of fluxes on the type of conductivity and the carrier concentration in the layers or their optical properties have been made as yet.

Below, we present, for the first time, the results of our study of the Hall effect and the photoluminescence spectra of grown by the MBE and δ-doped (with Si) GaAs layers obtained at various values of the γ ratio on the (111)A substrates and the substrates misoriented from this plane along the [$2\bar{1}\bar{1}$] direction.

Institute of Radio Engineering and Electronics, Russian Academy of Sciences, ul. Mokhovaya 11, Moscow, 103907 Russia

The specimens were grown on semi-insulated GaAs substrates with (111)A ± 0.5° orientation and also on substrates purposefully misoriented from this plane by an angle α (1°, 1.5°, and 3°) along the [$2\bar{1}\bar{1}$] direction by molecular beam epitaxy on the TsNA-24 setup. All the substrates were glued to the common molybdenum holder with the aid of indium in order to grow all the specimens simultaneously. Silicon-doped structures grown by this method also had a ~0.48 μm-thick undoped buffer GaAs layer, a Si δ-doped layer, and an ~0.033 μm-thick upper undoped or "cap" GaAs layer. Epitaxial growth was performed at T_g = 600°C. The temperature of the silicon source was chosen to provide an electron concentration of $n = 1 \times 10^{18}$ cm^{-3} in the (100) GaAs layers. The deposition time of the silicon in δ-doping was 135 s. During formation of δ-layers, the growth was ceased (the screen of the molecular gallium source was shut). The conditions of structure formation are listed in the table. Carrier concentrations and conductivity type were determined by Hall-effect measurements. The photoluminescence (PL) spectra were measured in the photon energy range $\hbar\omega$ from 1.3 to 1.55 eV at T = 77 K. The PL excitation was performed by an Ar^+-laser with a wavelength of λ = 488 nm and a maximum excitation power of 100 W/cm^2 on the specimen surface.

The photoluminescence spectra for specimens *1–5* are presented in Fig. 1. The growth conditions, the mobilities μ, and the layer concentration n_s are given in the table. All these specimens were grown at a P_{As}/P_{Ga} ratio of ≈18. Specimen *1* has *n*-type conductivity, whereas all the other specimens have *p*-type conductivity. The PL spectra of specimens *2–5* show two bands. One (at $\hbar\omega \approx 1.508$ eV, hereafter referred to as *B*-band) corresponds to the radiative interband recombination (*e–h*). The second broad band is observed at $\hbar\omega \approx$ 1.36–1.38 eV and is hereafter referred to as Si-band. Figure 2 presents the PL spectra of specimens *6–10* grown under the same conditions as specimens *1–5* but having no Si δ-layer. In this case, no Si band is observed. This gives grounds to ascribe it to a Si

1028-3358/01/4602-0088$21.00

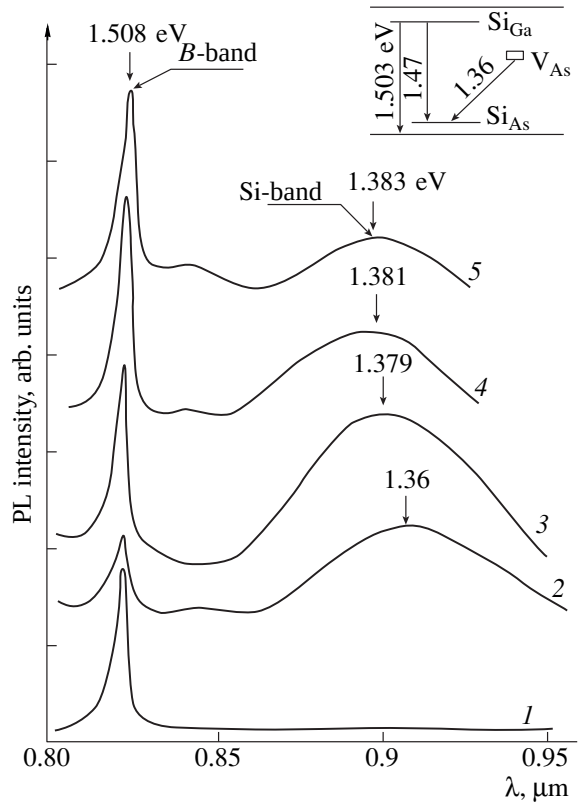

Fig. 1. PL spectra for specimens *1–5* grown at γ = 18 and having layers δ-doped with Si at $T = 77$ K. The curves are displaced with respect to each other along the vertical. The corresponding data are presented in the table. In the inset, a possible energy diagram for optical transitions is presented.

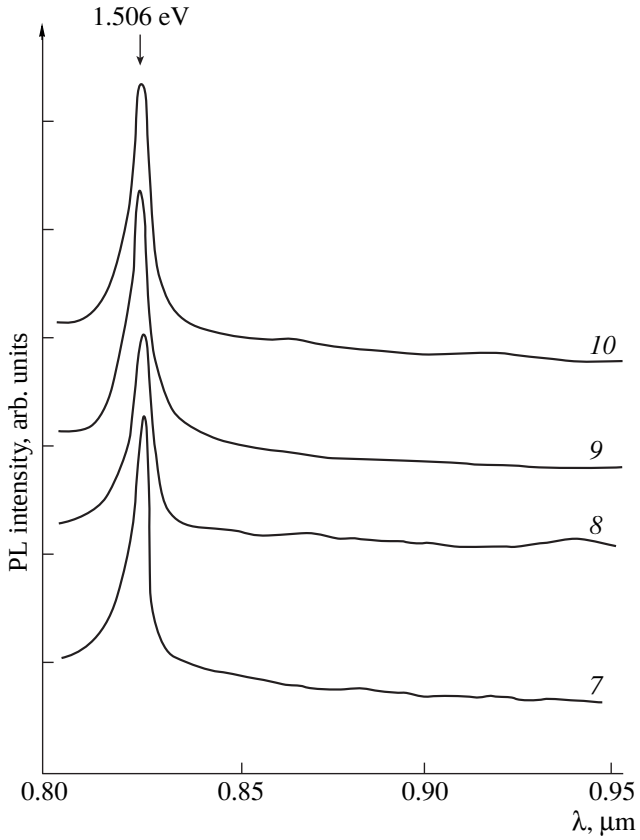

Fig. 2. PL spectra for specimens *7–10* grown at γ = 18 and having no layer δ-doped with Si at $T = 77$ K. The spectra are displaced with respect to each other along the vertical.

δ-doped layer. According to [6, 7], the PL spectra of single layers δ-doped with Be and grown on (100)GaAs have no such band. The PL bands due to the layer δ-doped with Be are located at $\hbar\omega = 1.42$–1.49 eV [6, 7].

According to [3, 8], the PL band at $\hbar\omega = 1.36$ eV in the homogeneously Si-doped GaAs (111)A layers is attributed to optical transitions between donor states associated with As-vacancies, V_{As}, and acceptor states

Table

Specimens	Substrate orientation	α, degree	γ	Conductivity type	n_s, p_s, cm^{-2}	μ, cm^2/(V s)
1	(100)	–	18	*n*	2×10^{12}	601
2	(111)A	±0.5	18	*p*	6.3×10^{12}	54
3	(111)A	1	18	*p*	1.0×10^{13}	43
4	(111)A	1.5	18	*p*	6.2×10^{12}	49
5	(111)A	3	18	*p*	4.9×10^{12}	60
11	(100)	–	63	*n*	1.3×10^{13}	305
12	(111)A	±0.5	63	*n*	3.6×10^{12}	129
13	(111)A	1	63	*n*	1.1×10^{12}	271
14	(111)A	1.5	63	*n*	2.0×10^{12}	175
15	(111)A	3	63	*n*	1.1×10^{12}	166

Note: α is the misorientation angle in the $[2\bar{1}\bar{1}]$ direction. Layer concentration n_s and mobility μ are measured at $T = 300$ K.

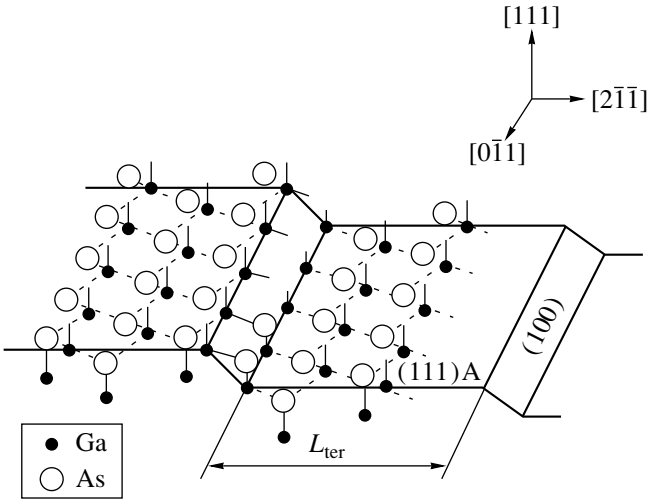

Fig. 3. Schematic arrangement of Ga and As atoms on the vicinal GaAs (111)A surface misoriented in the [2$\bar{1}\bar{1}$] direction.

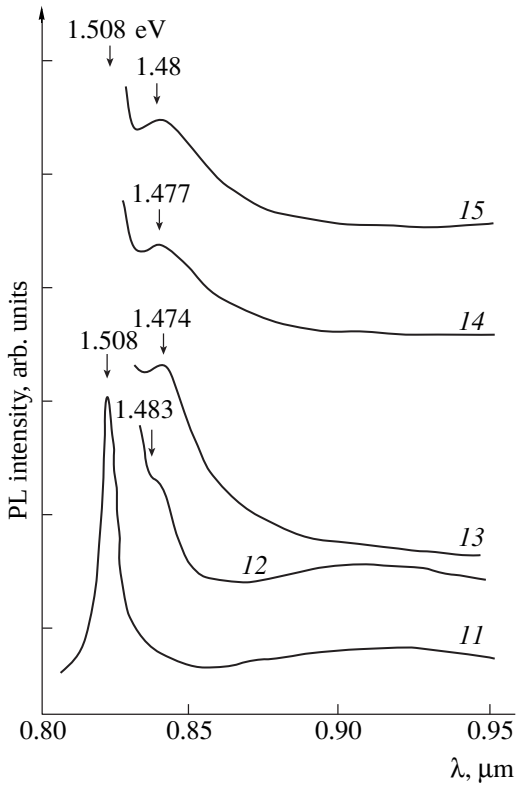

Fig. 4. PL spectra for specimens *11–15* grown at γ = 63 having layers δ-doped with Si at T = 77 K. The spectra are displaced with respect to each other along the vertical. For specimens *12–16*, the principal band ($\hbar\omega$ = 1.508 eV) is not shown.

associated with silicon atoms at the arsenic sites Si_{As}, i.e., to the transitions $V_{As} \longrightarrow Si_{As}$. This band is also observed in the Si-doped epitaxial layers grown on GaAs (100) after annealing at $T_{an} > 600$°C [9, 10] and in layers grown on (111)A, (211)A and (311)A substrates at low As pressures [8, 11]. The inset in Fig. 1 shows a diagram for the optical transitions constructed according to experimental data [3, 8, 9].

We consider the behavior of the Si-band as a function of misorientation angle α (Fig. 1). With an increase of misorientation, the peak of Si-band shifts to shorter wavelengths (from $\hbar\omega$ = 1.36 eV at α = 0° to 1.383 eV at α = 3°), which can be readily explained in terms of the bond density on the terraces and the steps. Figure 3 shows, schematically, the arrangement of Ga and As atoms on the vicinal surface at the misorientation of the (111)A plane of the GaAs substrate along the [2$\bar{1}\bar{1}$] direction. The vicinal surface is characterized by different densities of dangling Ga-bonds at terraces and steps; in other words, the conditions for formation of V_{As} vacancies and location of Si in the As sites are also different for the terraces and steps. We assume that donor–acceptor (D–A) pairs can be formed only if the distance r between them exceeds the Bohr radius. Then, according to [13], the emission energy of such a pair is determined by the expression

$$\hbar\omega = E_g - (E_A + E_D) + \frac{e^2}{4\pi\varepsilon\varepsilon_0 r},$$

where E_g is the gap energy; E_A and E_D are the acceptor and donor levels, respectively; ε and ε_0 are the relative dielectric constants of GaAs and vacuum, respectively; e is the electron charge; and r is the donor–acceptor distance. Thus, the transition energy $E_g - (E_A + E_D) \approx$ 1.36 eV should be corrected for the quantity $e^2/(4\pi\varepsilon\varepsilon_0 r)$ due to the interaction inside a D–A-pair. In our case, r is determined by a certain average donor–acceptor distance in pairs for a terrace of each length L_{ter}, which are 37.2, 18,6, 12.4, and 6.2 nm at α = 0.5°, 1°, 1.5°, and 3°, respectively. The values of $e^2/(4\pi\varepsilon\varepsilon_0 r)$ for r = 40 and r = 10 nm are 0.0027 and 0.012, respectively; i.e., it increases with the misorientation angle α and is comparable to the Si-band shift toward high energies observed in the PL spectra in Fig. 1. Thus, the Si-band shift with α can be explained by the variations in D–A distances in the D–A pairs at steps and the terraces of vicinal faces.

Now, we consider the epitaxial layers grown at a high γ value (≈63) providing the *n*-type conductivity. The PL spectra for specimens *11–15* grown at a high γ-ratio are shown in Fig. 4. As is seen from the table, all specimens exhibit the *n*-type conductivity. For the (100) orientation, the electron concentration at γ = 63 is higher than that at γ = 18, although the temperature of the silicon cell and the time of δ-layer formation were the same at both γ values. This may be explained by an increase of the number of Si atoms at Ga sites (Si_{Ga}), i.e., an increase of the donor concentration, since under high arsenic pressure P_{As}, the probability of occupying As sites by Si atoms decreases. As is seen from Fig. 4, in addition to the main band at $\hbar\omega$ = 1.508 eV, the mis-

oriented specimens also show a band at $\hbar\omega$ = 1.47–1.48. For specimen *12*, it has the shape of a "shoulder" in the range close to $\hbar\omega$ = 1.483 eV. With an increase of α, it becomes a simple peak (specimens *13*, *14*, and *15*). We believe that this band is caused by transitions between donor and acceptor silicon states, i.e., Si_{Ga}–Si_{As}.

Thus, our studies have shown that both *p*- and *n*-type δ-doped layers can be grown on (111)A substrates doped with silicon alone. The PL spectra for the (111)A substrate and substrates misoriented from this plane in the $[2\bar{1}\bar{1}]$ direction show bands that are attributed to single silicon δ-doped layers. The analysis of the PL spectra has shown that at low γ values (characteristic for formation of a *p*-type δ-layer), an increase in the misorientation angle results in a shift of the band at $\hbar\omega$ = 1.36 eV toward high energies. This shift is interpreted in terms of the variation of the average donor–acceptor distance in D–A-pairs because of an increase in terrace lengths at higher misorientation angles α.

REFERENCES

1. J.-S. Lee, H. Isshiki, T. Sugano, and Y. Aoyagi, J. Cryst. Growth **173**, 27 (1997).
2. Y. Okano, M. Shigeta, H. Seto, *et al.*, Jpn. J. Appl. Phys. **29**, L1357 (1990).
3. F. Plazza, L. Pavesi, M. Henin, and D. Johnston, Semicond. Sci. Technol. **7**, 1504 (1992).
4. V. G. Mokerov, G. B. Galiev, and Yu. V. Slepnev, Fiz. Tekh. Poluprovodn. (St. Petersburg) **32**, 1320 (1998) [Semiconductors **32**, 1175 (1998)].
5. G. B. Galiev, M. V. Karachevtseva, V. G. Mokerov, *et al.*, Dokl. Akad. Nauk **367**, 613 (1999) [Dokl. Phys. **44**, 510 (1999)].
6. D. Richards, J. Wagner, H. Schneider, *et al.*, Phys. Rev. B **47**, 9629 (1993).
7. G. M. Sipahi, R. Enderlein, L. M. R. Scolfaro, *et al.*, Phys. Rev. B **57**, 9168 (1998).
8. L. Pavesi, M. Henini, and D. Johnston, Appl. Phys. Lett. **66**, 2846 (1995).
9. H. Biray and J. Sites, J. Appl. Phys. **51**, 619 (1980).
10. L. Pavesi, N. H. Ky, J. D. Gariere, *et al.*, J. Appl. Phys. **71**, 2225 (1992).
11. J. Harrison, L. Pavesi, M. Henini, and D. Johnston, J. Appl. Phys. **75**, 3151 (1994).
12. L. Pavesi and M. Guzzi, J. Appl. Phys. **75**, 4779 (1994).

Translated by T. Galkina

Doklady Physics, Vol. 46, No. 2, 2001, pp. 92–96. Translated from Doklady Akademii Nauk, Vol. 376, No. 5, 2001, pp. 624–628.

TECHNICAL PHYSICS

On the Structure of a General Equation of State for Liquids and Gases

A. B. Kaplun and A. B. Meshalkin

Presented by Academician V.E. Nakoryakov June 14, 2000

Received June 27, 2000

There are hundreds of equations of state for liquids and gases that have been published. They describe thermal, caloric, acoustic, and other properties of a one-component substance (see, e.g., [1–6]). Rather arbitrarily, these equations can be divided into local and general ones. The former are intended to describe the separate regions of a thermodynamic surface, while the latter allow description by a single equation of thermodynamic properties for both liquids and gases to be made. However, despite long-term investigations in this field of thermodynamics, equations of different forms and structures are used for description of thermodynamic characteristics of a substance. Seemingly, the preferable form of the general equation of state has not been yet chosen in the literature. As is considered, the thermal equation of state having the form of a virial series in powers of density is the most validated from the theoretical point of view. However, as is well known, such a series diverges at high densities [4, 5]. Therefore, to accurately describe the thermodynamic properties of both liquid and gas in a wide range of state parameters, many authors express the compressibility factor as a power series in temperature and density instead of using the virial series.

In this paper, within the framework of phenomenological thermodynamics, we seek such a form (structure) of the thermal equation of state which could be considered preferable. Furthermore, based on it, we attempt to derive specific expressions for sufficiently accurate description of thermal properties of both liquid and gas.

The well-known exact equation of thermodynamics

$$\left(\frac{\partial U}{\partial v}\right)_T = T\left(\frac{\partial P}{\partial T}\right)_v - P \tag{1}$$

can be transformed into

$$\left(\frac{\partial U}{\partial v}\right)_T = \frac{RT^2}{v}\left(\frac{\partial Z}{\partial T}\right)_v, \tag{2}$$

where T and P are temperature and pressure, v is the volume, U is the internal energy, $z = \dfrac{Pv}{RT}$ is the compressibility factor, and R is the gas constant.

Taking the caloric equation $U = U(T, v)$ as initial (known), we can reduce Eq. (2) to the form

$$Z = \int \frac{v}{RT^2}\left(\frac{\partial U}{\partial v}\right)_T dT + \psi(v) = \varphi(T, v) + \psi(v). \tag{3}$$

Consequently, if the equation used for the internal energy is true, relation (3) determines the correct structure of the equation for Z. It is evident that, as $v \longrightarrow \infty$ (a state of a perfect gas), $\varphi(T, v) = 0$ and $\psi(v) = 1$. The physical meaning of the function $\psi(v)$ is to be clarified below.

From the mathematical point of view, an equation of the form

$$Z(T, v) = \varphi(T, v) + \psi(v) \tag{4}$$

is trivial. However, from the physical standpoint, Eqs. (3) and (4) imply the form of an equation of state that agrees with the correct equation for the internal energy and the exact thermodynamic relation (2).

The van der Waals equation

$$\left(P + \frac{a}{v^2}\right)(v - b) = RT \tag{5}$$

is the most known equation of state satisfying condition (3). It is written in terms of specific quantities, such as the specific volume v (the density $\rho = \dfrac{1}{v}$) and the gas constant R for a substance, which will also be used below. Then,

$$Z_{vW}(T, v) = -\frac{a}{vRT} + \frac{v}{v - b} = \varphi_{vW}(T, v) + \psi_{vW}(v), \tag{6}$$

Institute of Thermal Physics, Siberian Division, Russian Academy of Sciences, pr. Akademika Lavrent'eva 1, Novosibirsk, 630090 Russia

1028-3358/01/4602-0092$21.00

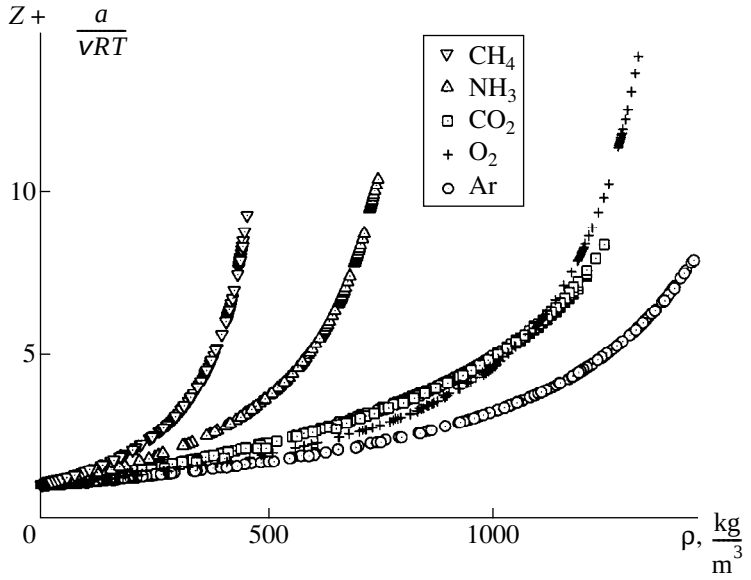

Fig. 1. Dependence of the function $y = Z + \frac{a}{vRT}$ on the density ρ.

where

$$\varphi_{vW}(T, v) = -\frac{a}{vRT}, \quad \psi_{vW}(v) = \frac{v}{v-b}.$$

According to (4),

$$\frac{Pv}{RT} - \varphi(T, v) = \psi(v); \tag{7}$$

i.e., the function $y(T, v) = Z - \varphi(T, v)$ must depend only on a single variable (volume) at arbitrary parameters T and v characterizing a thermodynamic system: $y(T, v) = \psi(v)$. The van der Waals equation should also satisfy this requirement in the case where the function $\varphi_{vW} = -\frac{a}{vRT}$ properly describes the behavior of the actual system. In other words, the condition

$$\frac{Pv}{RT} + \frac{a}{vRT} = \psi(v) \tag{8}$$

must be satisfied.

We can assume that, depending only on the single variable, the function $\psi(v)$ in (8), in the general case, can differ from $\psi_{vW}(v) = \frac{v}{v-b}$, which results from the van der Waals equation.

Equation (8) can be verified directly, because all quantities (except a) entering into its left-hand side can be measured experimentally or taken from reliable tabulated data for well-studied substances [7–13].

Figure 1 presents the results of calculations carried out for carbon dioxide, argon, oxygen, methane, and ammonia [7–11]. According to this figure, for each of the above-mentioned substances, fitting of the constant a in the first approximation (within a certain data spread) allows $y = Z + \frac{a}{vRT}$ to be considered as a single-valued function of the density: $y = f(\rho)$. The function $f(\rho)$ can be formally described, for example, by a polynomial on the basis of the least-square technique. At an equal number of polynomial coefficients, the best approximation was provided by a polynomial in odd powers of the density:

$$Z = 1 - \frac{a}{vRT} + \sum_{i=0}^{4} c_i \rho^{2i+1}. \tag{9}$$

The values Z_{calcd}, calculated by approximating Eq. (9) in a wide range of state parameters, differ from the tabular values of Z by no more than 0.13.

When following the spirit of the van der Waals ideas, according to Eq. (6), the calculated values of the function $y = \frac{Pv}{RT} + \frac{a}{vRT}$, at a certain a, must be equal to those of the function $\psi_{vW} = \frac{v}{v-b}$, which can be reduced to the form

$$\frac{v}{v-b} = 1 + \frac{b}{v-b}. \tag{10}$$

Therefore, according to the van der Waals equation, at a certain value of b, the plot of y as a function of $\frac{1}{v-b}$ must be represented by a straight line with a slope coefficient b. For argon, carbon dioxide, oxygen, methane, and ammonia, these plots are presented in Fig. 2. As is seen, within a certain interval of uncer-

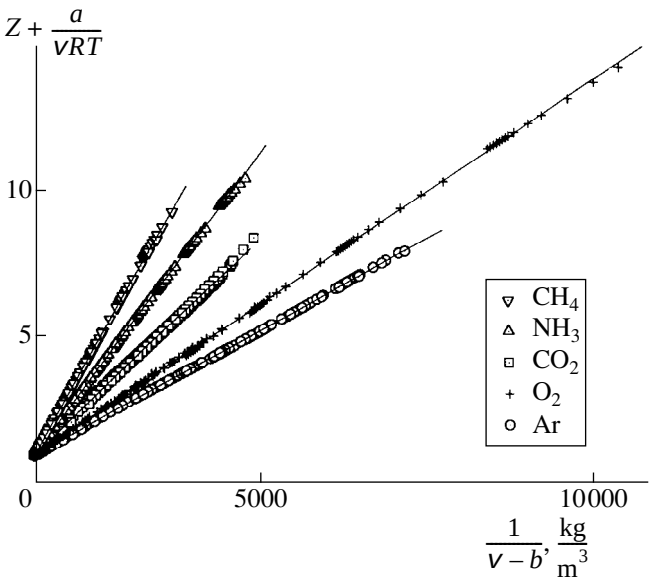

Fig. 2. Dependence of the function $y = Z + \frac{a}{vRT}$ on $\frac{1}{v-b}$. Symbols correspond to tabular experimental data; solid lines are plotted according to calculations by Eq. (12).

tainty, the relations y as functions of $\frac{1}{v-b}$ can actually be considered linear. However, their slope coefficients cannot even approximately be accepted equal to b.

In the general case, data plotted in Fig. 2 can be presented in the form

$$y = 1 + \frac{c}{v-b} \tag{11}$$

or

$$\frac{Pv}{RT} + \frac{a}{vRT} = 1 + \frac{c}{v-b}, \tag{12}$$

where c is the individual constant of the substance.

For certain well-studied substances, the coefficients in Eq. (12), which are calculated by optimizing the compressibility factor $Z = \frac{Pv}{RT}$ on the basis of the least-square technique, are presented in the table. According to it, the ratio $\frac{c}{b}$, even approximately, cannot be considered to be unity, as it follows from the van der Waals equation of state.

The compressibility factor Z that we have calculated by the equation

$$Z = 1 + \frac{c}{v-b} - \frac{a}{vRT} \tag{13}$$

using the least-square technique almost everywhere differs from tabular data by a value $\Delta Z \le \pm 0.1$. The discrepancy is higher only at high pressures and densities (near the triple point), near the critical point, and for rarefied gas. For such a simple three-parameter equation of state as (12) or (13), the result obtained is quite acceptable. Figure 3 represents the carbon dioxide pressure as a function of the gas density. The calculations are performed along isotherms by Eq. (13).

It was assumed above that, at a certain a, the function $y = Z + \frac{a}{vRT}$ is a single-valued function of density ρ. However, a detailed analysis of this function shows that, actually, at an arbitrary a, it systematically forms bundles corresponding to isolines (isotherms and isobars). Moreover, its splitting in bundles essentially exceeds the errors of experimental (tabular) data and, therefore, prevents further improvement of the description even at the expense of complication of the density function $f(\rho)$ and an increase in the number of fitting parameters.

Coefficients of the equation and an estimate of errors corresponding to calculations by formula (13) for various substances

Substance	R, $\frac{\text{J}}{\text{kg K}}$	Parameter ranges			a, $\frac{\text{J m}^3}{\text{kg}^2}$	b, $\frac{\text{m}^3}{\text{kg}}$	c, $\frac{\text{m}^3}{\text{kg}}$	$\frac{c}{b}$	$\sigma = \sqrt{\frac{(Z_{\text{tabl}} - Z_{\text{calcd}})^2}{N-1}}$
		T, K	P, MPa	ρ, $\frac{\text{kg}}{\text{m}^3}$					
Argon	208.17	90–500	0.1–50	10–1448	90	0.5406×10^{-3}	1.0434×10^{-3}	1.93	0.014
Neon	411.95	26–500	0.1–50	0.5–1296	49.9	0.6190×10^{-3}	0.9295×10^{-3}	1.50	0.034
Carbon dioxide	188.92	220–1000	0.1–100	5–1250	240	0.5451×10^{-3}	1.8053×10^{-3}	3.31	0.034
Methane	518.271	100–500	0.01–50	4–460	905.8	1.7857×10^{-3}	3.2836×10^{-3}	1.84	0.024
Propane	188.549	100–500	0.01–50	0.1–733	561.6	1.2304×10^{-3}	3.2593×10^{-3}	2.65	0.079
Ethylene	296.376	120–500	0.1–50	0.7–658	661.4	1.2914×10^{-3}	3.0653×10^{-3}	2.37	0.026
Oxygen	259.835	60–500	0.1–50	0.8–1330	138.04	0.6569×10^{-3}	1.2675×10^{-3}	1.93	0.031
Ammonia	481.617	200–600	0.1–50	0.3–750	1262	1.0732×10^{-3}	2.5324×10^{-3}	2.36	0.035

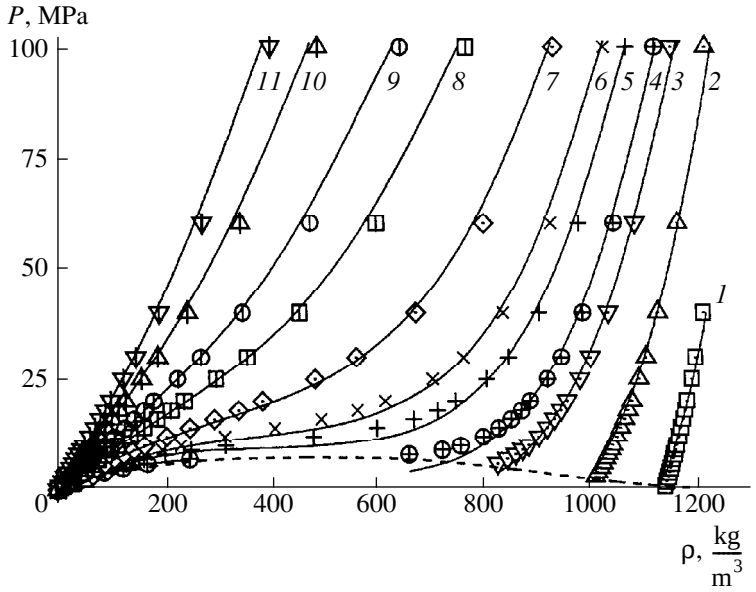

Fig. 3. Pressure of carbon dioxide as a function of density and temperature: (*1*) 230 K; (*2*) 260; (*3*) 290; (*4*) 305; (*5*) 330; (*6*) 350; (*7*) 400; (*8*) 500; (*9*) 600; (*10*) 800; (*11*) 1000. Symbols correspond to tabular experimental data; solid lines are calculated according to Eq. (13); the dashed line represents the liquid–vapor saturation curve.

In addition, similarly to the van der Waals equation, Eq. (13) does not provide a correct transformation to the case of rarefied gas whose equation of state can be described by the second virial coefficient $B(T)$. For many substances, the equation describing the temperature dependence $B(T)$ in the entire temperature range studied to date is presented to within experimental accuracy in [14].

Thus, Eqs. (12) and (13) qualitatively incorrectly describe the thermal properties of a substance in the critical region and in the region of rarefied gas. (Nevertheless, these equations describe experimental data throughout a wide range of parameters much better than other known few-parameter equations of state.) Therefore, it is natural to use these equations for describing the thermal properties of the liquid phase, i.e., in a narrower range of state parameters. It is evident that in this case, the constants of the equations can vary noticeably and the requirement that, at low densities, these equations turn into those of state for the perfect gas becomes unnecessary.

Then, Eq. (13) can be written as

$$Z = d + \frac{c}{v - b} - \frac{a}{vRT}. \qquad (14)$$

According to our calculations, Eq. (14) describes the thermal properties of the above-mentioned substances within the accuracy of experimental (tabular) data within the temperature range from T_{tr} to $0.9T_{cr}$ and for pressures varying up to 100 MPa. As an example, we present the equation of state for liquid carbon dioxide:

$$Z = \frac{pv}{RT} = 1.686 + \frac{1.469 \times 10^{-3}}{v - 0.594 \times 10^{-3}} - \frac{258}{vRT}. \qquad (14a)$$

where p, T, and v are expressed in megapascals, kelvins, and $m^3\ kg^{-1}$, respectively, and $R = 188.92\ J\ kg^{-1}\ K^{-1}$.

For the liquid CO_2 phase, the discrepancy between the tabular [7] and calculated [by Eq. (14a)] values of density does not exceed 0.2% at pressures up to 100 MPa (Fig. 4), which is comparable with the errors of experimental (tabular) data.

We now consider the physical meaning of the function $\psi(v)$. As is seen from Eq. (8), the temperature-

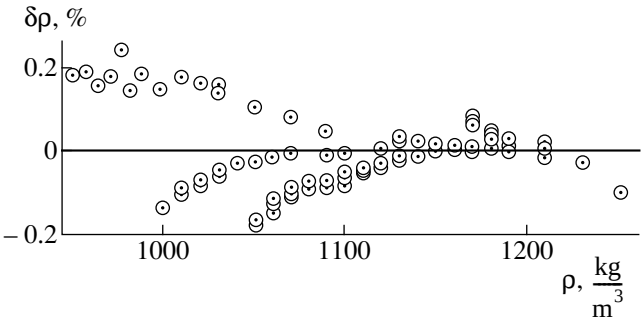

Fig. 4. Relative discrepancy between tabular and calculated [by Eq. (14a)] values of density for carbon dioxide $\delta\rho = \frac{\rho_{tabl} - \rho_{calcd}}{\rho_{tabl}} \times 100$ in the temperature ranges from 220 to 270 K and pressures up to 100 MPa.

dependent term $\varphi_{vW} = -\frac{a}{vRT}$ tends to zero as $T \longrightarrow \infty$ at arbitrary finite v if the coefficient a is a constant or a weakly varying function of temperature. Thus, the function

$$\psi(v) = \left(\frac{Pv}{RT}\right)_{T\to\infty}, \quad (15)$$

i.e., the function $\psi(v) = f(\rho)$, represents the compressibility factor Z at infinitely high temperatures. We can assume (although this question needs to be specially analyzed) that this conclusion does not depend on a specific form of the equation of state (presented here by the van der Waals equation) and results directly from Eq. (3). Then, Eqs. (8) and (15) determine the asymptotic behavior of an actual system at high temperatures provided the term $\frac{a}{v^2}$ entering into the van der Waals equation (5) sufficiently adequately describes the interparticle interaction in the actual system. In the literature, the high-temperature asymptotic equation of state is usually represented by the equation of state for hard spheres. According to our calculations, the compressibility factor for the system of hard spheres Z_{hs} coincides with $\psi(v)$ [or $f(\rho)$] only up to the critical density. With increasing the density, the discrepancies between Z_{hs} and $f(\rho)$ grow and can exceed two at the density occurring at the triple point.

Thus, the analysis and the calculations carried out in this paper show that a form (structure) of the general thermal equation of state (as well as of the local equations) is preferable provided that the equation for the compressibility factor $Z = \frac{pv}{RT}$ contains a term being a function only of one variable, namely, the density (or the specific volume). Certain known equations of state (see, e.g., [1, 2, 6]), as well as the van der Waals equation (6), contain a density function as a term. However, as far as we know, the fact that just such a structure of the equation of state is preferable has not been thoroughly discussed in the literature.

REFERENCES

1. J. O. Hirschfelder, C. F. Curtiss, and R. B. Bird, *Molecular Theory of Gases and Liquids* (Wiley, New York, 1954; Inostrannaya Literatura, Moscow, 1961).
2. M. P. Vukalovich and I. I. Novikov, *Equations of State for Actual Gases* (Nauka, Moscow, 1948).
3. *Equations of State for Gases and Liquids*, Ed. by I. I. Novikov (Nauka, Moscow, 1975).
4. E. Mason and T. Spurling, *The Virial Equation of State* (Pergamon, New York, 1969; Mir, Moscow, 1972).
5. *Physics of Simple Liquids*, Ed. by H. N. V. Temperley, J. S. Rowlinson, and G. S. Rushbrooke (North-Holland, Amsterdam, 1968; Mir, Moscow, 1971).
6. G. A. Spiridonov and I. S. Kvasov, Obzory po Teplofiz. Svoĭstvam Veshchestv, No. 1 (57), 45 (1986).
7. V. V. Altunin, *Thermal Properties of Carbon Dioxide* (Izd. Standartov, Moscow, 1975).
8. V. A. Rabinovich, A. A. Vasserman, V. I. Nedostup, and L. S. Veksler, *Thermal Properties of Neon, Argon, Krypton, and Xenon* (Izd. Standartov, Moscow, 1976).
9. *Thermodynamic Properties of Methane*, Ed. by V. V. Sychev, A. A. Vasserman, V. A. Zagoruchenko, *et al.* (Izd. Standartov, Moscow, 1979).
10. I. F. Golubev, V. P. Kiyashova, I. I. Perel'shteĭn, and E. B. Parushin, *Thermal Properties of Ammonia* (Izd. Standartov, Moscow, 1978).
11. *Thermodynamic Properties of Oxygen*, Ed. by V. V. Sychev, A. A. Vasserman, A. D. Kozlov, *et al.* (Izd. Standartov, Moscow, 1981).
12. V. V. Sychev, A. A. Vasserman, A. D. Kozlov, and V. A. Tsymarnyĭ, *Thermodynamic Properties of Propane* (Izd. Standartov, Moscow, 1989).
13. *Thermodynamic Properties of Ethylene*, Ed. by V. V. Sychev, A. A. Vasserman, E. A. Golovskiĭ, *et al.* (Izd. Standartov, Moscow, 1981).
14. A. B. Kaplun and A. B. Meshalkin, High Temp. High Press. **31**, 253 (1999).

Translated by Yu. Verevochkin

Doklady Physics, Vol. 46, No. 2, 2001, pp. 97–102. Translated from Doklady Akademii Nauk, Vol. 376, No. 5, 2001, pp. 629–634.

TECHNICAL PHYSICS

Robust Nonlinear Image Filtration with Retention of Small-Size Details in the Presence of Pulse and Multiplicative Interferences

V. F. Kravchenko*, V. I. Ponomarev,**
Corresponding Member of the RAS V. I. Pustovoĭt*, and L. Ninjo-de-Rivera****

Received October 16, 2000

1. Space and airborne systems for the Earth's surface remote sensing (RS) have gained wide-spread application in ecological and agricultural monitoring, survey of natural resources, etc., [1–5]. Unfortunately, in many practical instances, the quality of images obtained with such systems is unacceptable due to the noise effect. In practice, nonlinear filters are widely used for image filtration and processing in view of their ability to suppress noise of various nature [6]. However, well-known nonlinear filters are primarily aimed at retention of boundaries of large-scale objects in an image rather than of its small-size details [7–9].

In this paper, new robust filtration algorithms employed for image processing are presented. These algorithms provide retention of small-size details while suppressing pulse noise and multiplicative interference.

To this end, we employed a modification of the standard sigma filter [7], which is generally recognized by its ability to retain small-size details. The algorithm uses a robust filter of the *KNN*-type as a preliminary result in calculating the locally adaptive *M*-estimate [6]. The restraining function for the *M*-estimate is similar to that used in the sigma filter. Estimation of data local activity is introduced, which is similar to that employed for estimating local statistics in a Lie filter [8]. The image filter proposed has the property of efficiently suppressing both pulse and multiplicative interferences.

2. There exists a number of physical models for the noise effect [2, 6, 10, 11]. Employed here is the following physical model of image distortion in the presence of pulse interference [10, 11]:

$$u(x, y) = N_{\text{pulse}}(I(x, y)). \quad (1)$$

Here, $I(x, y)$ is the initial image, $u(x, y)$ is the result of the image distortion by the pulse noise, and $N_{\text{pulse}}(I(x, y))$ is the functional determining the noise effect on the image:

$$N_{\text{pulse}}(I(x, y)) = \begin{cases} \text{an event with a random amplitude} \\ \text{and a probability of occurrence } P_i \\ I(x, y), \text{ otherwise.} \end{cases}$$

We consider that in the digital-image case for data taken in byte representation, the pulse noise is uniformly distributed within the interval of values [0, …, 255].

In addition to the pulse noise, an image formed in RS systems [1, 2] is also distorted by multiplicative interference. In this connection, noise model (1) is transformed to the form

$$u(x, y) = N_{\text{pulse}}(\varepsilon_{\text{mult}}(x, y)I(x, y)). \quad (2)$$

Here, $\varepsilon_{\text{mult}}(x, y)$ corresponds to the multiplicative noise.

Thus, the problem is to develop a robust filtration algorithm capable of eliminating pulse noise, suppressing multiplicative interference, and providing reasonable retention of small-size image details. Such contradictory requirements to the filtration algorithm can be realized only by invoking nonlinear filtration procedures.

3. Robust image-filtration algorithms based on a simplified one-step scheme for calculating reduced robust *M*-estimates for the data sampling mean value **X** were proposed in [10, 11]:

$$\theta_{\text{med}\mathbf{M}} = \text{med}\{X_i\tilde{\psi}(X_i - \text{med}\{\mathbf{X}\}), i = 1, \ldots, n\}, \quad (3)$$

$$\theta_{\text{Wil}\mathbf{M}} = \operatorname{med}_{i \le j}\{0.5[X_i\tilde{\psi}(X_i - \text{med}\{\mathbf{X}\}) + X_j\tilde{\psi}(X_j - \text{med}\{\mathbf{X}\})], i = 1, \ldots, n\}. \quad (4)$$

* *Institute of Radio Engineering and Electronics, Russian Academy of Sciences, ul. Mokhovaya 18, Moscow, 103907 Russia*

** *National Polytechnic Institute of Mexico, Santa Anna pr. 1000, Mexico City, 04430 Mexico*

*** *Central Design Bureau of Unique Instrumentation, Russian Academy of Sciences, ul. Butlerova 15, Moscow, 117342 Russia*

1028-3358/01/4602-0097$21.00

Below, we use a simple approximation for the cutoff function $\psi(X)$, which is related to the Huber robust *M*-estimate [12] for a normal distribution having long tails:

$$\tilde{\psi}(X) = \begin{cases} X, & |X| \le r \\ 0, & |X| > r. \end{cases} \quad (5)$$

The function $\tilde{\psi}$ is the normalized ψ-function: $\psi(X) = X\tilde{\psi}(X)$.

The principal idea realized in these algorithms consists in substituting the arithmetic truncated mean (which is characteristic of robust *M*-estimates) by the mean value calculated in terms of ranks or *R*-estimates. As was shown recently [10, 11], *RM*-estimates (3), (4) constructed by this procedure possess robust properties which are superior to those of the basic *R*- and *M*-estimates.

Employing *K* elements of a sampling whose values are closest to the central element (pixel) of the filter window, we obtain the well-known *KNN*-filtration algorithm [13] for images with an initial estimate:

$$\hat{I}_{KNN}(i, j) = \frac{1}{\sum_{m=-L}^{L}\sum_{n=-L}^{L}\tilde{\psi}(u(i+m, j+n))} \times \sum_{m=-L}^{L}\sum_{n=-L}^{L}\tilde{\psi}(u(i+m, j+n))u(i+m, j+n). \quad (6)$$

Here,

$$\tilde{\psi}(u(i+m, j+n)) = \begin{cases} 1, & \text{if } u(i+m, j+n) \text{ is one of the } K \\ & \text{elements closest to } u(i, j) \\ 0, & \text{otherwise,} \end{cases}$$

and $m, n = -L, \ldots, L$.

For improving the robust properties of (6), we propose changing the arithmetic mean in (6) to the rank estimate used in *RM*-algorithms (4), (5):

$$\hat{I}_{MMKNN}(i, j) = \text{med}\{u_{KNN}(i+m, j+n)\}, \quad (7)$$

$$\hat{I}_{WMKNN}(i, j) = \text{med}\left\{\frac{[u_{KNN}(i+m, j+n) + u_{KNN}(i+m_1, j+n_1)]}{2}\right\}. \quad (8)$$

Here, $u_{KNN}(i+m, j+n)$, $u_{KNN}(i+m_1, j+n_1)$ is the totality of *K* pixels in the filtration window which are closest in value to the central element $u(i, j)$, $m \le m_1$, $n \le n_1$, $m, n, m_1, n_1 = -L, \ldots, L$.

Simulation of filtration algorithms (6)–(8) has shown that algorithm (6) has no property of revealing random pulse disturbances and much less of suppressing them. On the contrary, robust algorithms (7), (8) ensure the suppression of pulse interferences even for low probabilities of their appearance. In this case, the ability of suppressing disturbances considerably decreases near boundaries of extended objects.

Improvement of the properties of algorithm (6) is attained by additional allowance for elements possessing the closest values in the pixel sampling within the window near the object boundaries. The number of these elements is calculated from the parameter of the local activity of sampling data. In addition, the use of the iterative scheme in calculating estimates is proposed.

With this scheme taken into account, filtration algorithm (6) transforms into a linear algorithm of the modified *KNN* filter (*LMKNN*):

$$\hat{I}^{(q)}_{LMKNN}(i, j) = \frac{1}{K_{\text{close}}}\sum_{m=-L}^{L}\sum_{n=-L}^{L}\tilde{\psi}^{(q-1)}(u(i+m, j+n), \hat{I}^{(q-1)}) \times u(i+m, j+n), \quad (9)$$

where

$$\tilde{\psi}^{(q-1)}(u(i+m, j+n), \hat{I}^{(q-1)}) = \begin{cases} 1, & \text{if } u(i+m, j+n) \text{ is one of the } K_c \text{ elements} \\ & \text{closest in its value to } \hat{I}^{(q-1)}(i, j) \\ 0, & \text{otherwise.} \end{cases}$$

Here,

$$K_c = K + a\Sigma(u(i, j)) \le K_{\max},$$
$$\Sigma(u(i, j)) = \text{med}\{|\text{med}\{u(i, j)\} - u(i+m, j+n)|\},$$
$$\hat{I}^{(0)}_{LMKNN}(i, j) = u(i, j). \quad (10)$$

The parameter *a* determines the algorithm sensitivity to local data variations near the object boundaries. The maximum number $K_{\max}$ of elements neighboring the central one determines the boundary smoothing and retention of the image small-size details. Filtration algorithm (9) is the generalization of filter (6) and is equivalent to (6) in the case $q = 1$ and $a = 0$.

Variants of the *RM*-type algorithms for *KNN* filtration, which are applicable to processing of wide-class images, are realized on the basis of *R*-estimates (4), (5) in the form of two algorithms of *RMKNN* filtration.

The first one is the median algorithm of the *M*-type for *KNN*-filtration, i.e., the *MMKNN*-algorithm:

$$\hat{I}^{(q)}_{MMKNN}(i, j) = \text{med}\{h^{(q)}(i+m, j+n)\}. \quad (11)$$

Here, $h^{(q)}(i+m, j+n)$ determines K_c values for the sampling in the window, which are closest with respect to

the estimate at the previous step $\hat{I}^{(q-1)}_{MMKNN}(i, j)$, $\hat{I}^{0}_{MMKNN}(i, j) = u(i, j)$.

The second algorithm is the *KNN*-filtration *M*-type Wilcoxon algorithm, i.e., the *WMKNN* algorithm:

$$\hat{I}_{WMKNN}(i, j) = \operatorname{med}\left\{\frac{[h^{(q)}(i + m, j + n) + h^{(q)}(i + m_1, j + n_1)]}{2}\right\}. \quad (12)$$

Here, the values $h^{(q)}(i + m, j + n)$, $h^{(q)}(i + m_1, j + n_1)$ are determined by K_c closest sampling values in the window with respect to the estimate at the previous step $\hat{I}^{(q-1)}_{WMKNN}(i, j)$, $\hat{I}^{(0)}_{WMKNN}(i, j) = u(i, j)$; the value K_c is determined by relation (10), where $m \le m_1, n \le n_1, m, n, m_1, n_1 = -L, \ldots, L$. In (11) and (12), iterations cease when $\hat{I}^{(q)}(i, j) = \hat{I}^{(q-1)}(i, j)$.

4. In the course of numerical simulation, filters (9), (11), and (12) were noticed to be sensitive to the value of $\Sigma(u(i, j))$ from (10). We now propose the following modification of the detector $\Sigma(u(i, j))$, which provides a higher quality filter operation:

$$\Sigma(u(i, j)) = \frac{\operatorname{med}\{|u(i, j) - u(i + m, j + n)|\}}{\operatorname{MADM}\{u(i, j)\}} + 0.5\frac{\operatorname{MADM}\{u(i, j + l)\}}{\operatorname{med}\{u(i + k, j + l)\}}. \quad (13)$$

Here, $\operatorname{med}\{u(i + k, j + l)\}$ is the sampling median within the filtration window; $k, l = -L, \ldots, L$; and MADM is the median of absolute deviations from the median.

As a result of modeling, for a wide range of pulse-noise intensities, the window size 5×5 was found to be optimal. In this case, the minimum number of neighboring elements $K_{\min} = 5$ provides satisfactory retention of small-size details in the image and sufficient suppression of pulse noise.

To improve the quality of the pulse-noise suppression, when K_c is reasonably large, filtration employing a median filter can be performed. It was shown by numerical simulation that, for $K_c > 7$ and $K_c > 350$, the filter described in (10), (13), and (11) can be replaced by a median one with a window size of 3×3 and 5×5, respectively.

For suppressing multiplicative interference, we propose a new robust filtration algorithm for the first time. This algorithm preserves the pulse-noise elimination properties of the filter described previously and is capable of suppressing multiplicative interference. In this case, the yield of the filter described in (10), (13), and (11) is used as the initial estimate for computing another *M*-estimate suitable for image filtration [10, 11]. In addition, the robust *M*-estimate is employed on the basis of the cutoff function:

$$\Omega(u) = \begin{cases} u, & |u - \theta^{(0)}| \le b\operatorname{med}\{\mathbf{U}\} \\ 0, & \text{otherwise.} \end{cases} \quad (14)$$

Here, $\mathbf{U}$ is a vector composed of image elements inside the filtration window, $\theta^{(0)} = \hat{I}_{MMKNN}(i, j)$, and $\operatorname{med}\{\mathbf{U}\}$ is the median for a sampling of elements from the filtration window of size 5×5. Thus, with allowance for cutoff function (14), the *M*-type filter can be written in the form

$$\hat{I}_M(i, j) = \frac{\sum_{m=-M}^{M}\sum_{n=-M}^{M} u(i, j)\Omega'\{u(i + m, j + n) - \hat{I}^{(0)}(i, j)\}}{\sum_{k=-M}^{M}\sum_{l=-M}^{M}\Omega'\{u(i + m, j + n) - \hat{I}^{(0)}(i, j)\}}, \quad (15)$$

where

$$\Omega'\{u(i + m, j + n) - \hat{I}^{(0)}(i, j)\} = \begin{cases} 1, & |u(i + m, j + n) - \hat{I}^{(0)}(i, j)| \le b\operatorname{med}\{\mathbf{U}(i, j)\} \\ 0, & \text{otherwise;} \end{cases}$$

and $\operatorname{med}\{\mathbf{U}(i, j)\}$ is the median for a sampling of the image elements inside the filtration window [the coefficient b controls the suppression of multiplicative interference; $m, n = -L, \ldots, L$; $2(L + 1)$ are the vertical and horizontal sizes of the filtration window]. Here, $\hat{I}^{(0)}(i, j) = \hat{I}_{MMKNN}(i, j)$.

Simulation of the algorithm has shown that filter (15) possesses a property of suppressing multiplicative interference but efficiently retains small-size image details only in the case of a low noise level. With the goal to remedy this drawback, we propose an adaptive scheme similar to that used in the Lie filter [8, 14]. Then, the image-filtration algorithm is represented in the form

$$\hat{I}(i, j) = \hat{I}_{MMKNN}(i, j)Q(i, j) + (1 - Q(i, j))\hat{I}_M(i, j). \quad (16)$$

Here,

$$Q(i, j) = 1 - \left(c\frac{\hat{I}_M(i, j)}{\operatorname{med}\{|\hat{I}_M(i, j) - U(i + m, j + n)|\}}\right)^2 \quad (17)$$

is the robust estimate for the local data activity and the coefficient c controls the degree of retention of small-size image details; $m, n = -L, \ldots, L$.

Thus, the proposed image-filtration algorithm (8), (9) is a connected series of two filters retaining image small-size details, namely, a 5×5 *MMKNN*-filter (10), (13), (11) for pulse-noise suppression and an *M*-filter (15) for multiplicative-interference suppression. *M*-filter (15) is similar to the well-known sigma filter retaining small-size image details with allowance made for the weighted processing on the basis of local-activity data.

At the final stage, the yields of these two filters are mixed in algorithm (16), (17) by a method similar to that used in the Lie filter [8].

5. A number of numerical experiments are carried out with the aim of studying the properties of new algorithms (9), (11), (12), (15)–(17). These algorithms are compared with the algorithm of the *KNN*-filter (6), as well as with the median filter. As the efficiency criterion, we employed that of the mean square error (MSE): $\mathrm{MSE} = \langle [I(x, y) - \hat{I}(x, y)]^2 \rangle$.

Artificial test images were used for evaluating the deterministic characteristics of the filtration algorithms. The simulation has shown that, in the noniterative variant, the *KNN*-filter does not change the object boundaries and restores image small-size details. Algorithms (9), (11), and (12) with parameters $a = 0$, $q = 25$ provide retention of the image boundaries and small-size details if the value K_c is equal to the filtration-window size. If this size is 3×3 and $K_c > 3$, the small-size details of the test image are reduced to one pixel of resolution.

Analysis of the experimental results shows that the *WMKNN* algorithm provides better reconstructed small-size details than the standard median filter even when the latter employs a filtration window with a smaller aperture. The standard median filter does not retain thin lines and distorts the angles of triangular objects. Similar results were obtained when processing the widely used test image "Lena". We can conclude that the response functions of the filters proposed provide good reconstruction of the object boundaries.

For studying the statistical characteristics of noise suppression by the *RM*-type filtration algorithms, the initial test image was distorted by pulse noise according to physical model (1). The maximum number of iterations was $q_{\max} = 25$. Analysis of the statistical-simulation data for the *RMKNN* algorithms has shown that they provide distortions with significantly smaller MSE-values in the resulting image compared to the median filter. For a low-intensity noise, *MMKNN* algorithm (11) provides the best results in terms of MSE-value for the 5×5 filtration-window. However, in the case of high noise intensity, the best image quality is provided by *WMKNN*-filter algorithm (12).

It is worth noting that the MSE-minimum criterion does not reflect the image-filtration quality from the standpoint of the suppression of random-interference pulses. Additional visual analysis of the filtration should be carried out with respect to retention of the image boundaries and small-size details. With this fact taken into account, we list in Table 1 the characteristics obtained in the process of simulating the algorithms being analyzed for two widely used in the literature test images "Lena" and "Bridge" [10, 11].

As follows from Table 1, *WMKNN* algorithm (12) provides the best filtration quality for all cases under study. *MMKNN* algorithm (11) yields good results when the noise intensity is not very high. The *LMKNN* algorithm yields the worst results. For low noise intensity, the 3×3 window is preferable. However, for a high-intensity noise, the 5×5 window should be used.

For finding the characteristics of the proposed noise suppression by filters (14)–(16), the standard test images "Lena" and "Mandrill," as well as other ones distorted by a mixture of multiplicative Gaussian noise and pulse noise (2), were used. The following parameters of the noise mixture were varied: the probability of the appearance of a pulse with a random amplitude in each image reading and the relative variance of multiplicative interference. The filter parameters a and c were also varied. The minimum values of the MSE for the test image "Lena" determined from the simulation results are listed in Table 2. For a quantitative comparison of the characteristics for the filter developed, the results of the noise suppression for the test image by the 5×5 median filter are listed in the same table (in brackets).

It can be concluded from the analysis of the tables that the filter proposed provides better quantitative results (compared to the standard median filter) when the relative variance of multiplicative interference is lower than 0.25. However, when the noise relative variance is much higher than 0.25, the filter proposed does not adequately suppress the noise. This fact can be explained by the strongly nonlinear structure of the filter proposed ceasing its operations when the neighboring elements have their maximum or minimum values, which occurs reasonably often within the range from 0 to 255, i.e., when the relative variance is too large. The filter "recognizes" the destroyed regions as spurious objects by realizing the procedure of their reconstruction as small-size details of the image.

6. Thus, new robust nonlinear-filtration algorithms of the *RM*-type for RS-system image processing are obtained and analyzed for the first time [15]. Such filters are capable of simultaneously suppressing a complicated noise mixture, of leaving sharp boundaries of large-size objects, and of retaining small-size details in the images being processed. The optimum parameters employed in adaptive algorithms for various physical characteristics of a noise mixture were determined. The filters developed provide good visual quality of the images processed when the relative variance of multiplicative noise is not too large and the probability of appearance of pulse interferences corresponds to a moderate level.

Table 1. Results of statistical simulation of algorithms

Pulse-noise probability	Algorithm	MSE	Detail retention	Noise suppression	Window	K_c	a
0.01	*LMKNN*	36.68	Poor	Strong	3×3	4	0.1
	MMKNN	35.10	Good	Strong	3×3	4	0.05
	WMKNN	28.64	Excellent	Strong	3×3	4	0.05
	LMKNN	30.83	Fair	Strong	5×5	5	0.1
	MMKNN	22.58	Good	Strong	5×5	5	0.1
	WMKNN	14.71	Excellent	Strong	5×5	5	0.05
0.05	*LMKNN*	44.07	Poor	Strong	5×5	5	0.1
	MMKNN	47.07	Fair	Strong	5×5	5	0.1
	WMKNN	41.0	Good	Strong	5×5	5	0.1
	LMKNN	44.09	Fair	Strong	5×5	7	0.05
	MMKNN	47.21	Good	Strong	5×5	7	0.05
	WMKNN	41.49	Excellent	Strong	5×5	7	0.05
0.1	*LMKNN*	51.64	Very poor	Weak	3×3	4	0.5
	MMKNN	55.24	Very poor	Weak	3×3	4	0.5
	WMKNN	52.66	Very poor	Weak	3×3	4	0.5
	LMKNN	57.89	Poor	Excellent	5×5	5	0.1
	MMKNN	65.28	Poor	Strong	5×5	5	0.1
	WMKNN	56.59	Fair	Strong	5×5	5	0.1
	LMKNN	66.07	Poor	Excellent	5×5	7	0.1
	MMKNN	61.82	Fair	Strong	5×5	7	0.05
	WMKNN	55.81	Good	Strong	5×5	7	0.05

Table 2. Minimum values of the mean-square error (MSE), which are obtained as a result of simulating the algorithm developed for the test image "Lena"

Pulse-noise probability	Relative variance of multiplicative interference (the bracketed numbers are the MSE for the 5×5 median filter)			
	0	0.05	0.1	0.25
0.00	3.4 (37.5)	63.6 (86.9)	116.4 (129.1)	268.4 (170.1)
0.01	6.4 (37.8)	66.3 (87.7)	120.8 (130.8)	265.9 (251.6)
0.05	16.75 (39.5)	76.9 (90.1)	126.9 (135.5)	280.2 (258.0)
0.10	31.9 (41.8)	90.8 (96.0)	142.8 (142.3)	253.9 (266.5)
0.15	30.45 (45.4)	102.9 (103.8)	134.2 (153.0)	271.8 (280.1)
0.20	36.74 (50.1)	111.8 (112.9)	149.9 (165.1)	288.8 (298.8)

The results obtained demonstrate the advantages of the new robust algorithms introduced for the *RM*-filtration while processing images in problems of remote sensing.

REFERENCES

1. S. E. Fal'kovich, V. I. Ponomarev, and Yu. V. Shkvarko, *Optimum Receiving of Space-Time Signals in Radio Channels with Allowance for Scattering* (Radio i Svyaz', Moscow, 1989).
2. A. A. Goncharenko, V. F. Kravchenko, and V. I. Ponomarev, *Remote Sensing in Inhomogeneous Media* (Radio i Svyaz', Moscow, 1991).
3. S. G. Zubkovich, *Statistical Characteristics of Signals Reflected from the Earth's Surface* (Sov. Radio, Moscow, 1968).

4. V. F. Kravchenko, V. I. Ponomaryov, R. Haime-Rivas, and Yu. V. Shkvarko, J. Commun. Technol. Electron. **45**, 872 (2000).
5. J.-O. Éklund, G. J. Nussbaumer, *et al.*, *Fast Algorithms in Image Numerical Processing* (Radio i Svyaz', Moscow, 1984).
6. J. Astola and P. Kuosmanen, *Fundamentals of Nonlinear Digital Filtering* (CRC Press, New York, 1997).
7. J. S. Lee, Comput. Vision, Graph. Image Processing. **24**, 255 (1983).
8. Lee Jong-Sen, IEEE Trans. Pattern Anal. Mach. Intell. **PAM1-2** (2), 125 (1980).
9. V. Lukin, N. N. Ponomarenko, P. Kuosmanen, and J. Astola, in *Proceedings of EUSIPCO-96, Eighth European Signal Processing Conference, Trieste, 1996*, Vol. 3, p. 1909.
10. V. F. Kravchenko, V. I. Pustovoĭt, V. I. Ponomarev, and A. B. Pogrebnyak, Dokl. Akad. Nauk. **371**, 611 (2000) [Dokl. Phys. **45**, 149 (2000)].
11. V. I. Ponomaryov and O. B. Pogrebnyak, J. Electron. Imaging **8**, 467 (1999).
12. F. R. Hampel, E. M. Ronchetti, P. J. Roussew, and W. A. Stahel, *Robust Statistics: The Approach Based on Influence Function* (Wiley, New York, 1986).
13. I. Pitas and A. N. Venetsanopoulos, *Nonlinear Digital Filters: Principles and Applications* (Kluwer, New York, 1990).
14. W. Y. Han and J. Ch. Lin, Electron. Lett. **33**, 124 (1997).
15. V. K. Volosyuk, V. F. Kravchenko, and V. I. Ponomarev, Zarub. Radioélektronika: Usp. Sovr. Radioélektron., No. 12, 3–74 (2000).

Translated by V. Tsarev